ABSTRACT

Title of Dissertation: PERFORMANCE OF ELECTRIC MEDIUM-SIZED VARIABLE-RPM ROTOR AND SHROUDED ROTOR

Peter Christian Ryseck
Masters of Science, 2022

Thesis directed by: Professor Inderjit Chopra
Department of Aerospace Engineering

Electric variable RPM rotors are increasingly being used for propulsion and control of unmanned air vehicles. As these vehicles scale to carry heavier payloads of 50 to 400 lbs (20 to 180 kgs) in the group 2 and 3 UAS category, there are concerns about their aerodynamic performance and handling quality degradation. Therefore, there is a need to develop a systematic experimental testing procedure to measure loads on these systems to evaluate performance and augment Computational Fluid Dynamic (CFD) validation tools. In this work, a universal electric powered test rig is designed and fabricated for hover and wind tunnel tests of open and shrouded rotors. Steady hover results are validated using blade element momentum theory. These predictions incorporate an empirical correction approach in conjunction with an interpolation scheme to capture Reynolds number variation along the span of the blade and variation with RPM. Results show good agreement with the interpolation method for the low Reynolds number rotor tested ($Re_{tip} < 500,000$).

For the variable RPM rotor, transient step and chirp inputs are also presented. System identification showed linear frequency responses between thrust and torque with RPM and RPM-square in hover. Therefore, when modeling this rotor, steady inflow appears adequate in the frequency range of interest (0.4 to 60 rad/sec). In addition to an open rotor, the electric motor-rotor test stand was used to test a shrouded rotor in hover and forward flight to systematically compare performance results. Test data showed the shrouded rotor gained 15% thrust for the same power in hover with the best configuration. For low speed forward flight, lift-to-drag ratio was found to increase by 8 to 10% for the shrouded rotor system over the isolated rotor.

PERFORMANCE OF ELECTRIC MEDIUM-SIZED VARIABLE-RPM ROTOR AND SHROUDED ROTOR

by

Peter Christian Ryseck

Dissertation submitted to the Faculty of the Graduate School of the
University of Maryland, College Park in partial fulfillment
of the requirements for the degree of
Master of Science
2022

Advisory Committee:
Professor Inderjit Chopra, Chair
Professor Anubhav Datta
Professor James Baeder

Acknowledgments

There are countless friends and mentors who have guided me in my progress as a researcher and engineer. I am extremely grateful for their support and will do my best to express my gratitude in a few short words:

Dr. Chopra, as my advisor since I joined the research lab in 2016, your mentorship, guidance, and wisdom has shaped me into an independent and passionate researcher. The trust you instilled in me will not go forgotten, and I will cherish the lessons you have taught me forever.

Dr. Anubhav Datta, thank you for sharing your experience, knowledge, and teaching me to trust myself.

From the Army Research Laboratory, Dr. Rajneesh Singh, Dr. Mathew Floros, Dr. John Hyrnuk and Dr. George Jacobellis. Through summer internships and graduate school, your feedback and assistance in my work has been invaluable, thank you!

Dr. Derrick Yeo, from easily beating you in go kart races to being mutually amused by seemingly random things to presenting our work at conferences, your impact on my life as a scholar and friend is immeasurable. I, like one of your many students, will be forever grateful.

Dr. Vikram Hrishikeshavan, you showed me that research is more than a job, it is a passion fueled opportunity to learn and share new things. The trust you placed in me as a freshman set me on the course I am on today, thank you!

From the John's Hopkins Applied Physics Laboratory, thank you Dr. Elena Shrestha, Jibu, Bernadine, Kate, and Chuck for your help in the shrouded rotor study.

Thank you to everyone in the lab for your help and advice including: Shashank, Brandyn, Derek, Nick, Radu, and Remi. Thank you to those in the GLMWT – Dr. Barlow, Noah, Ben, and Joe – your patience as I navigated wind tunnel operations was appreciated. Thank you to Emily Glover and Dr. Mark Lopez from San Jose State University and the DEVCOM Aviation Missile Center for assistance with system identification analysis.

Lastly, thank you to my family, my parents and my sisters, for our strong relationship bound together by mutual laughter and love.

Table of Contents

Chapter 1: Introduction

1.1 Applications of Multicopter Aircraft

Unmanned air vehicles (UAV) with vertical flight capabilities offer solutions to a variety of diverse situations spanning from disaster relief efforts to monitoring of crop yields. Within the Department of Defense (DoD), multicopter air vehicles can serve a number of applications that include surveillance, reconnaissance and cargo delivery for future war fighters. Their ability to take off vertically, hover, transition to forward flight and land vertically in confined areas provides them operational advantages over fixed-wing aircraft.

Recent advances in electric propulsion, manufacturing capabilities, and autonomy have created a new market for advanced vertical take-off and landing (VTOL) aircraft. In particular, multi-rotors are a cost effective strategy to achieve flight stable vehicles that can serve on demand applications because of their easy scalability in quantity. For the future war fighter, multiple vehicles could be stationed throughout a battlefield to deliver critically needed medical supplies in the event of a casualty [1]. In Kruger Park, when a poacher's approximate location is discovered, UAVs could be sent to scan the area and provide information to rangers on the ground [2]. In the event of a natural disaster, UAVs could serve as the primary search vehicle in search and rescue efforts, allowing rescue crews to plan routes and save lives more efficiently [3]. With increasing uncontrolled wild fires, unmanned air systems (UAS) could serve as aerial water tankers that extinguish flames, working collectively to maximize the ratio of water dropped to operational costs compared to traditional methods [4].

Beyond scalability in quantity, multi-rotors have potential to be scaled in platform size. This could allow for carrying larger and heavier payloads which would typically be transported by slower ground transport or traditional full-scale rotorcraft. Above group 2 UAS with max gross take-off weight (MGTOW) greater than 50 lb, electric multi-rotors can be used to transport passengers and cargo, allowing for a number of advantages such as reduction in mechanical complexity, noise, and pollution when compared to traditional single main rotor helicopters. Thus, the coupling of scalability in platform size and quantity provides operational advantages unlike any other platform.

The TRV-80 (Tactical Resupply Vehicle) is being developed and evaluated by the DoD for unmanned assured logistics resupply to support traditional ground-based units. This aircraft is the focus of this thesis. The aircraft has four sets of 28 inch (0.7 m) diameter counter-rotating coaxial rotors in a quadrotor configuration and is capable of carrying a payload of 25 lbs (11 kg) for a total flight range of 17 miles (28 km) under li-ion battery power [5].

Figure 1.1: Tactical Resupply Vehicle (TRV-80) being prepared for flight by a Marine. [5]

1.2 Background, Motivation and Previous Work

As these vehicles scale up to carry larger payloads of 50 to 400+ lbs (20 to 180+ kgs) in the group 2 and 3 UAS categories, a detailed understanding of the aerodynamic performance is crucial to design more efficient and capable vehicles. The aerodynamics need to be investigated in order to maximize aircraft range and endurance, thereby improving overall mission effectiveness.

1.2.1 Variable-RPM and Variable-Pitch Rotor Comparison

Instead of using traditional collective and cyclic controls with a swash plate, multicopters make use of RPM for varying thrust and torque and is therefore a function of the rotor speed squared. Beside steady loading, transient RPM variation for control has limited bandwidth due to factors such as rotor inertia and overall electrical system phase lag. Phillips et al. investigated a combination of rotor RPM and collective input in hover and forward flight for an experimental 8 lb quadrotor-biplane vehicle [6]. Due to concerns with forward flight efficiency and control as these vehicles scale, it is important to develop a better understanding of the trade-offs between both approaches of control. McKay et al. simulated quadcopter dynamics and found that a quadcopter equipped with variable-pitch rotors required more power for varying thrust in hover but yielded a 70% greater climb rate than the variable-RPM case [7]. In addition to performance trades, there are considerations to made be with respect to controls and flying qualities. Most important, the inertial effects of a variable RPM rotor have implications on thrust and torque response as the rotor scales. Examining several multirotor rotors, rotor inertia was found to increase considerably for rotors greater than 1.5 ft as found by Walter et al. [8].

Building a better model of the response dynamics will improve understanding of handling quality degradation and system climb rates as these vehicles scale up. Thus, it is necessary to experimentally quantify isolated rotor output loads in response to doublet and chirp inputs. A frequency-response curve that characterizes this single-input/single-output (SISO) subsystem can be obtained from experimental data. Ultimately, this will inform modeling and simulation development using physics based and system identified models.

1.2.2 Low Speed Forward Flight Performance

Figure 1.2: TRV-150 in low speed cruise [9].

UAVs operate in low speed forward flight or in hover with a side wind for extensive periods of flight. Thus, it is important to better understand low speed aerodynamics for UAV drag and rotor roll and pitching moments produced in edgewise flight which have implications on controls and vehicle design. Bart et al [10] performed wind tunnel testing on a small 9 inch (0.23 m) diameter propeller at incidence angles ranging from -90° to 90° with inflow speeds (axial velocity) ranging from 0 to 9 m/s. Results showed strong moments acting on the propeller in forward flight and unstable conditions in descending flight. A roll and pitching moment was present that was comparable in magnitude to rotor torque and was found to increase with higher inflow speeds and incidence angles, suggesting an increased flow velocity difference through the disk due to the high advance ratios. Similar wind tunnel studies have been conducted on larger rotors such as one by Kolaei [11] with an 18 inch (0.45 m) diameter rotor up to 25 m/s inflow speed. NASA also performed a wind tunnel study investigating several multicopters and measuring component loads of the bare airframe, isolated rotor, and full airframe to validate analytical and numerical models at both the full vehicle and component levels [12]. The experimental measurement of these quantities will validate and improve physics-based models resulting in superior flight control systems and autonomy for UAVs.

Lastly, Reynolds number has a significant effect on medium-sized variable RPM rotors. Deters et al. found through experimental tests that as the Reynolds number increases, the thrust coefficient increases and the power coefficient decreases [13]. Careful consideration to Reynolds number effects needs to be accounted for as was needed for the high endurance micro quadrotor helicopter developed and described by Winslow et al. [14].

1.2.3 Ducted Rotor Configuration

It is well established that ducted rotor configurations have the potential to offer significant performance benefits over equivalently sized open rotor systems, including increased thrust and reduced power consumption [16]. Beyond performance advantages, ducts may offer rotor noise shielding and safety for personnel operating near the vehicle. However,

Figure 1.3: Bell Nexus ducted rotor eVTOL concept [15].

there is limited experimental data publicly available to validate analytical aerodynamic predictions. Helios is a Computational Fluid Dynamics (CFD) tool developed by the DoD through the Computational Research and Engineering Acquisition Tools and Environments - Air Vehicle Design (CREATE-AV) program and is intended specifically for rotorcraft [17]. Helios is a highly-regarded and well-validated tool for open rotor configurations and is used extensively by the rotorcraft community for DoD-related applications. Before relying on Helios for the design of a ducted rotor system, it is necessary to validate CFD predictions against experimental data. Due to the aerodynamic interaction of the rotor blades with the surrounding duct geometry, there is a significant impact on the loads and performance of the overall system. As such, validation efforts which do not quantify this interaction do not offer sufficient information for ducted rotor vehicle design analysis. To ensure that appropriate considerations are made with regards to surface and volume grid generation, the near body solver, turbulence and transition models, and various other parameters relevant to CFD analysis, a validation study of Helios is necessary to accurately predict static, edgewise, and axial flight conditions of a ducted rotor system.

Chew et al. experimentally tested 3D printed shrouds with a 5 inch diameter rotor in addition to validating results with CFD analysis [18]. Performance gains were found by using both experimental testing and CFD to vary the duct wall geometry with the goal of maximizing efficiency. In addition to hover performance, the shroud geometry needs to be carefully considered to minimize the pitching moment due to edgewise gusts as found by Hrishikeshavan et al. [19].

1.3 Outline of Thesis

This thesis is organized into five chapters. Each chapter is self contained but draws from concepts addressed in previous ones. The organization is as follows:

Chapter 1: A discussion of the background and motivation for this research is provided.

Chapter 2: A description of the experimental test rig and test articles is given. Design, analysis, and validation of experimental components is presented. Operating procedures and axis conventions are described.

Chapter 3: Blade element momentum theory (BEMT) with two Reynolds number correction approaches is explained and compared with experimental hover results. Transient step and chirp input results are presented with Comprehensive Identification from Frequency Response (CIFER) analysis.

Chapter 4: Experimental comparison of a shrouded and isolated rotor in hover and low speed wind tunnel conditions is provided and discussed. Helios CFD results are validated for static and climb conditions.

Chapter 5: Conclusions and potential future work are described.

Chapter 2: Experimental Setup and Operating Procedures

2.1 Test Hardware and Data Collection

2.1.1 General Overview

A test stand was designed and built to be used for hover and wind tunnel tests in the Glenn L. Martin Wind Tunnel (GLMWT) at the University of Maryland [20]. The wind tunnel is closed loop and has a test section that is 11 ft wide by 7.8 ft tall (3.4 m by 2.4 m) and is capable of speeds up to 230 mph (103 m/s). Its layout is shown in Figure 2.1.

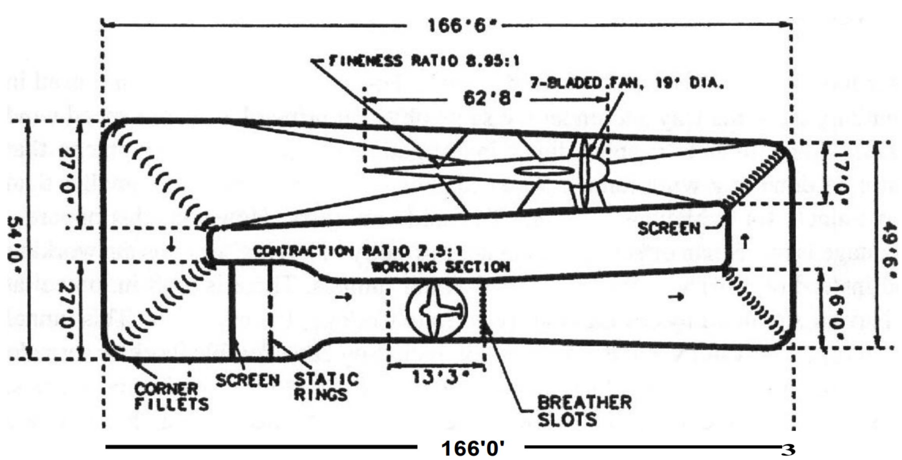

Figure 2.1: Layout of the Glenn L. Martin wind tunnel at the University of Maryland [21].

2.1.2 Universal Test Stand

Because the rotor and airframe are to be tested within the same range of α angles from -90° to 90°, a universal test stand (UTS) was designed and built to support a range of test articles. In this way, a variety of airframes and rotors can be tested without the need to replace the entire support structure and force/moment balance, thereby saving test time and maximizing consistency when exchanging test articles. The stand can also be installed on a hover tower for hover tests outside of the wind tunnel to limit wall effects and recirculation. Both configurations are shown in Figure 2.2 and overall dimensions are shown in Figure 2.3. It is constructed from 1/4 inch (6.35 mm) thick steel square beams that are welded together in an L-shape to minimize wake interference effects.

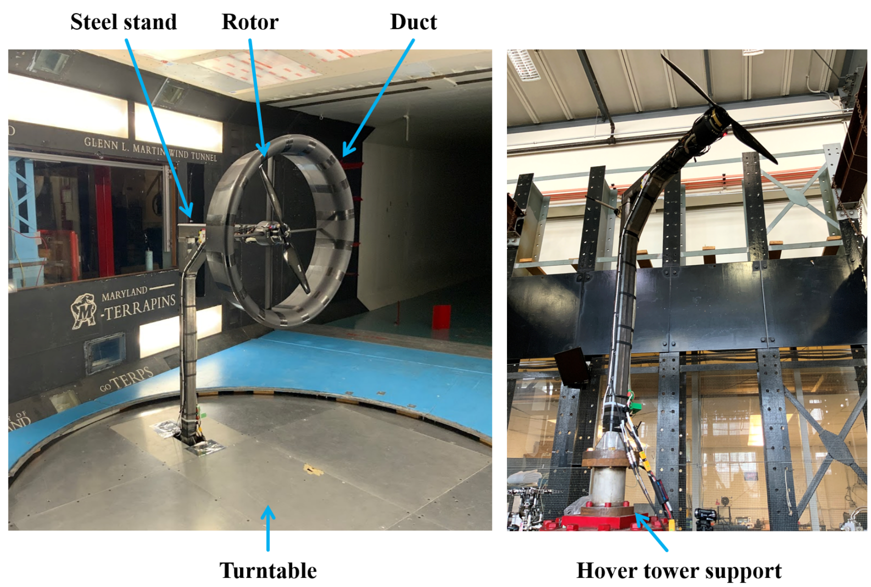

Figure 2.2: Universal Test Stand (UTS) in Glenn L. Martin Wind Tunnel test section and on hover tower with T-motor 28×9.2 rotor.

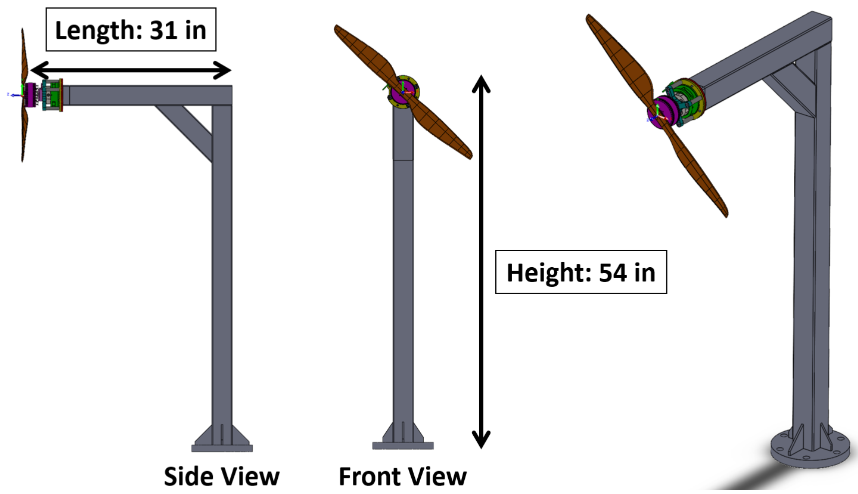

Figure 2.3: Universal Test Stand (UTS) dimensions.

2.1.3 Load Cells

Two six degree of freedom (DOF) ATI Mini-45 load cells were used in this study: First, to measure rotor loads, a load cell with the SI-290-10 calibration was chosen based on its maximum force and moment measurement limits and high resolution [22]. Second, to measure the shroud and airframe loads which have greater mass, a second load cell with both the SI-290-10 and SI-580-20 calibrations was chosen based on the expected maximum loads and desired resolutions. Calibration matrices were provided by the distributor ATI and verified prior to testing with known weights. These calibrations are shown in Figure 2.4. Momentum theory calculations were used to determine the approximate maximum thrust which was used to size the maximum load limits for the load cell. Hover tests later revealed the maximum force by thrust measured was approximately 110 N, 21% of the F_Z

limit, therefore ensuring the load cell would not be saturated.

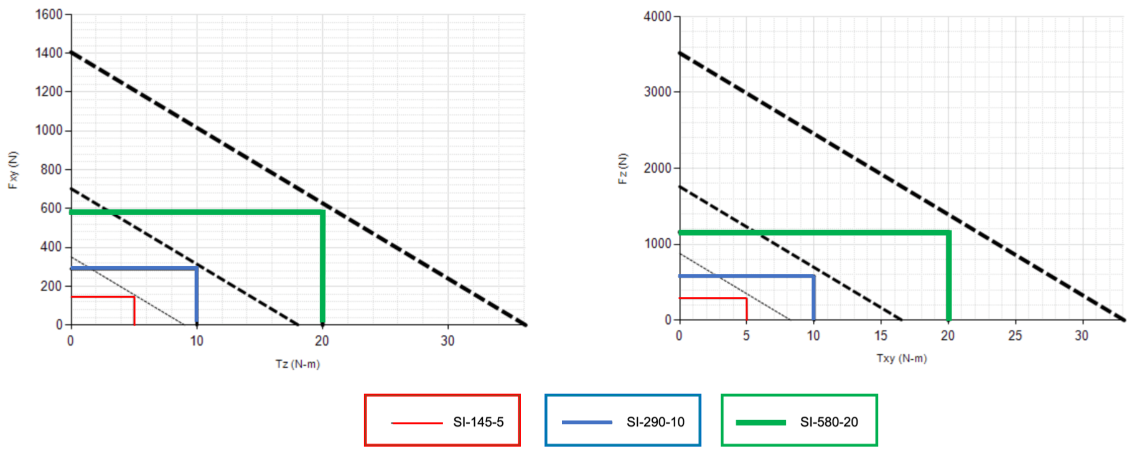

Figure 2.4: Metric sensing range and resolution for ATI Mini-45 load cell for SI-290-10 and SI-580-20 calibrations.

Additional tests were conducted to further verify that the calibration matrices provided by ATI were correct. This was done by loading the load cell with known weights and comparing to the measured load. The plot shown in Figure 2.5 shows a correlation of measured and actual force F_Z. The calibration results yielded a root mean square (RMS) value of approximately 0.999 for both load cells.

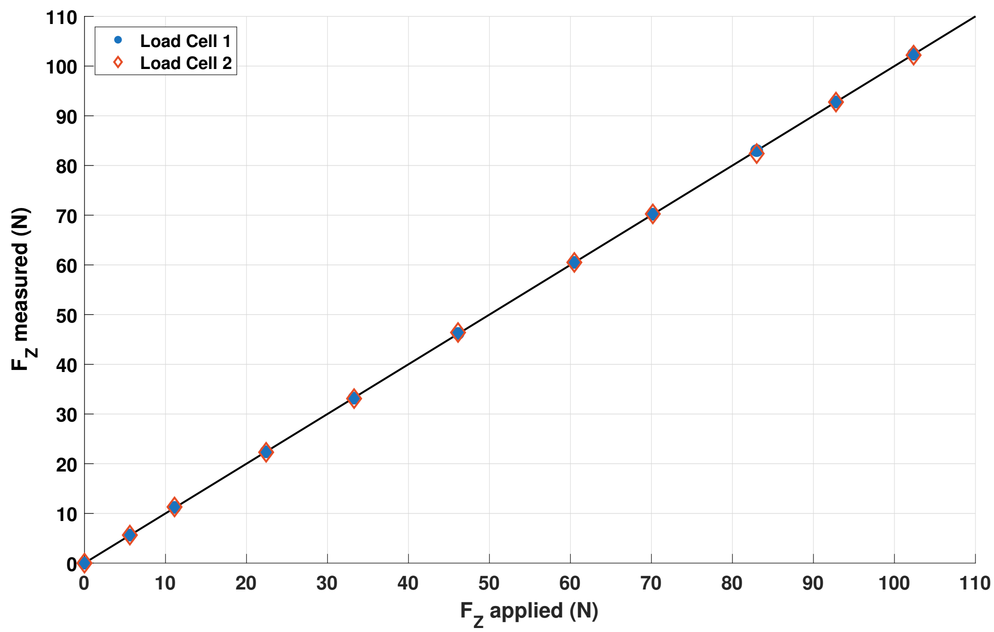

Figure 2.5: Load cell 1 and 2 F_Z calibration check.

2.1.4 Support Hardware

While in the wind tunnel, the test setup takes advantage of the rotating mounting floor which rotates the entire testing rig from α = -90° to 90°as shown in Figure 2.6. The floor also has the ability to translate the stand forward and aft in order to center the specific test article.

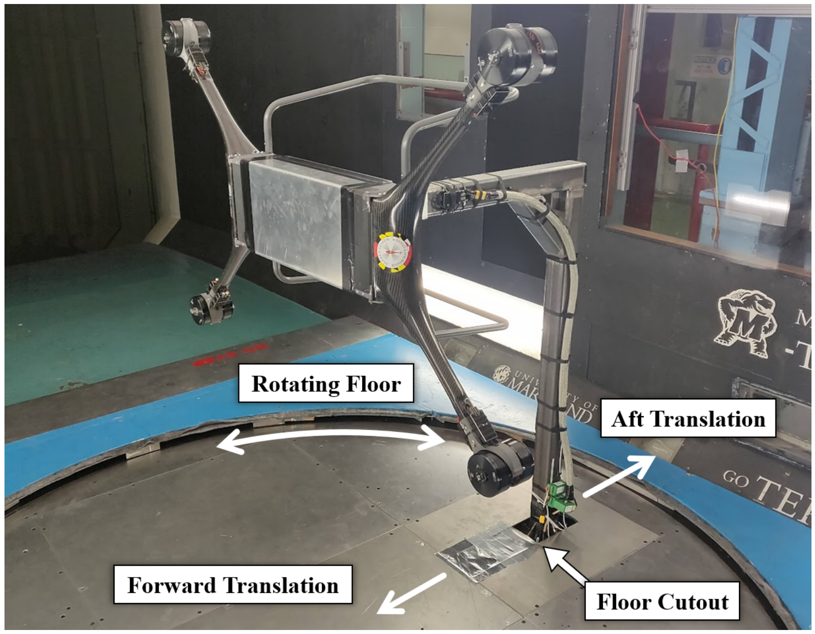

Figure 2.6: Universal Test Stand (UTS) ability to translate with cutout in aluminum plated floor.

The load cell is mounted to the front of the stand putting the rotor plane 0.69 m (96% of rotor diameter) forward of the vertical support beam in order to reduce interference effects with the support structure. For the airframe, additional structure is required pushing the center of the airframe 0.88 m forward of the vertical support beam to allow for a yaw angle change mechanism. These test articles with differing arm lengths can nonetheless both be centered in the test section by using the translating pads beneath the tunnel floor.

The TRV-80 airframe has a rotor center-to-center distance of 0.8 m $\times$ 1.3 m. It also includes landing legs, giving the airframe an overall height of 0.5 m. The airframe is mounted 90° on its side to allow for use of the rotating floor for angle of attack changes. Changing the yaw angle of the airframe required manual adjustment using a yaw tube and stub mechanism similar to the assembly used by Russel [12] which ensured reliable repeatability. The mechanism, shown in Figures 2.7, 2.8 and 2.9, is capable of testing a yaw angle range of 0 to 90° in 15° increments. Only some of these angles were tested, making the time spent manually adjusting the airframe yaw angle largely insignificant. The load cell is mounted forward of this mechanism and rotates with the model to increase system stiffness and keep the body axis aligned with the load cell.

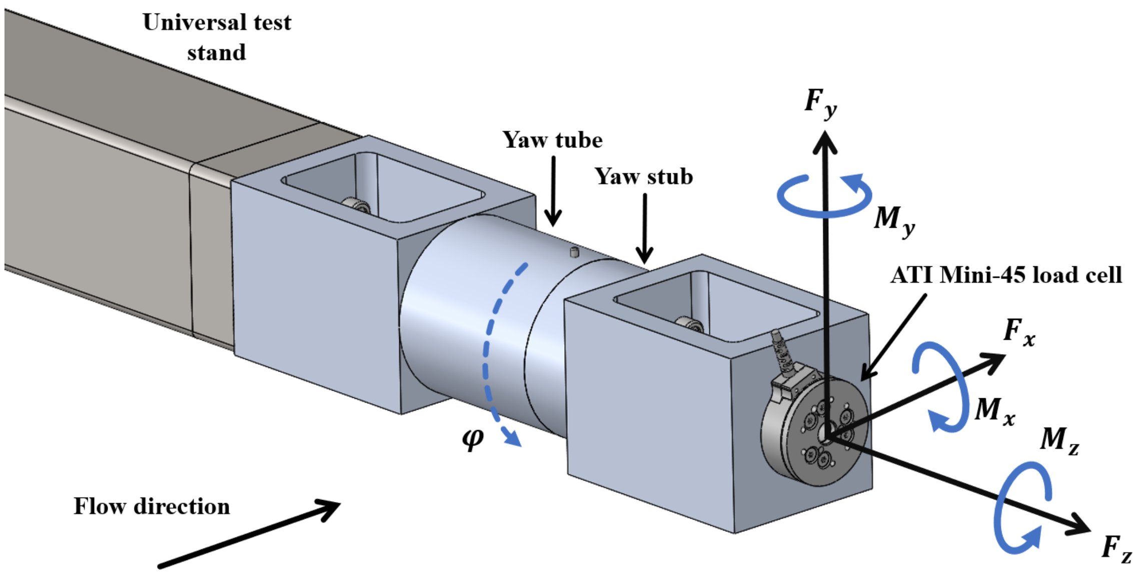

Figure 2.7: Airframe mounting hardware.

The yaw change mechanism shown in Figure 2.8 consists of five parts to mount the airframe to the test stand. A ‘yaw stub’ rotates inside a ‘yaw tube’. A locking pin can then be inserted to lock the orientation and a bolt fastened to further secure the mechanism from unwanted movement.

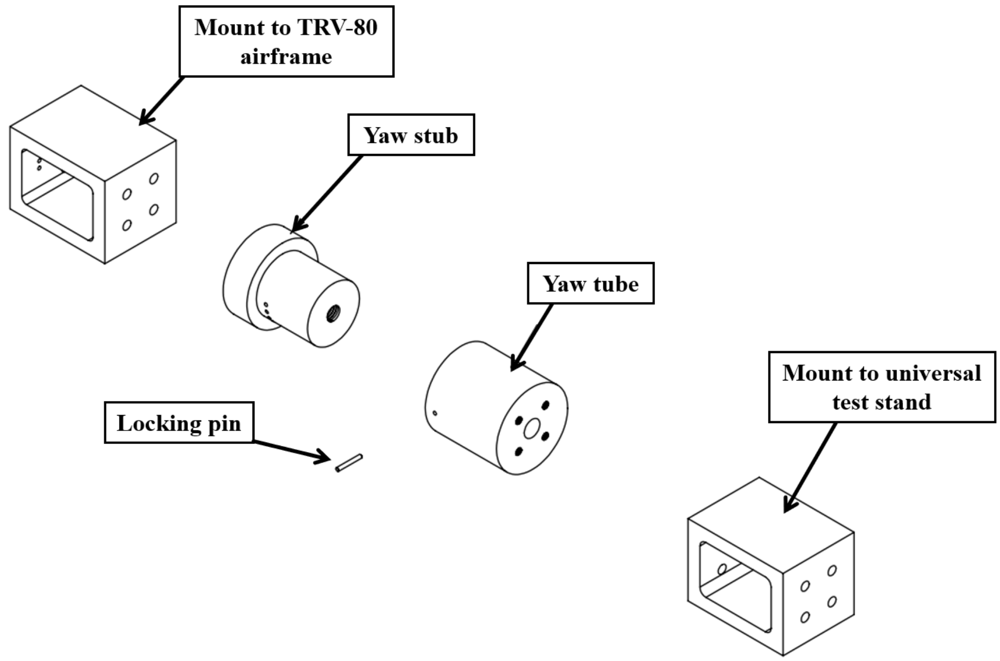

Figure 2.8: Parts for airframe yaw mechanism.

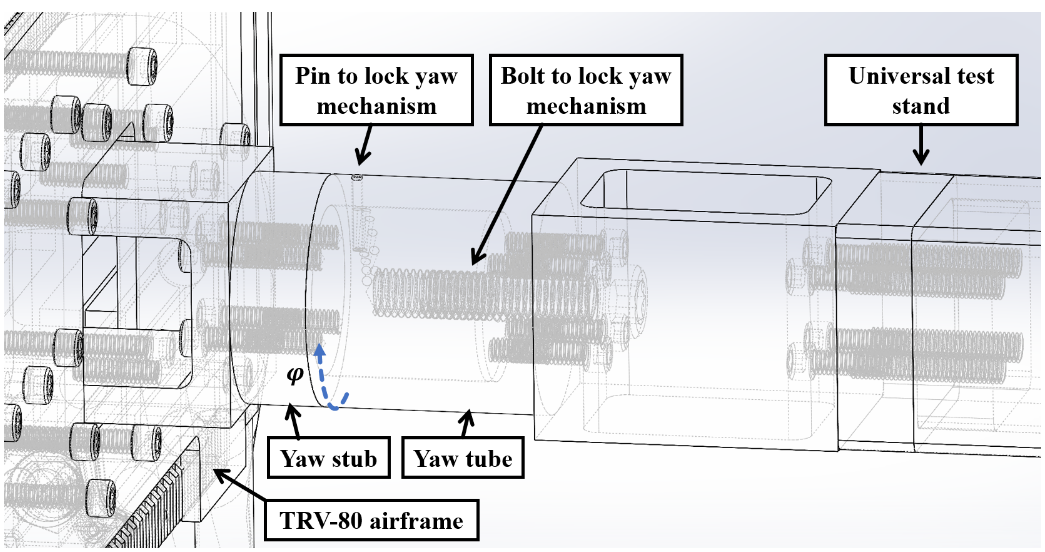

Figure 2.9: Internal structural view of airframe yaw mechanism.

To spin the rotor, the motor used was a T-motor brushless DC P80III 100 KV motor coupled with a Flame 80 A electronic speed controller (ESC) capable of a maximum rotational speed of 4500 RPM with a 28 inch diameter rotor. A different set of mounting hardware was used to mount the motor as is shown below in Figure 2.10.

F

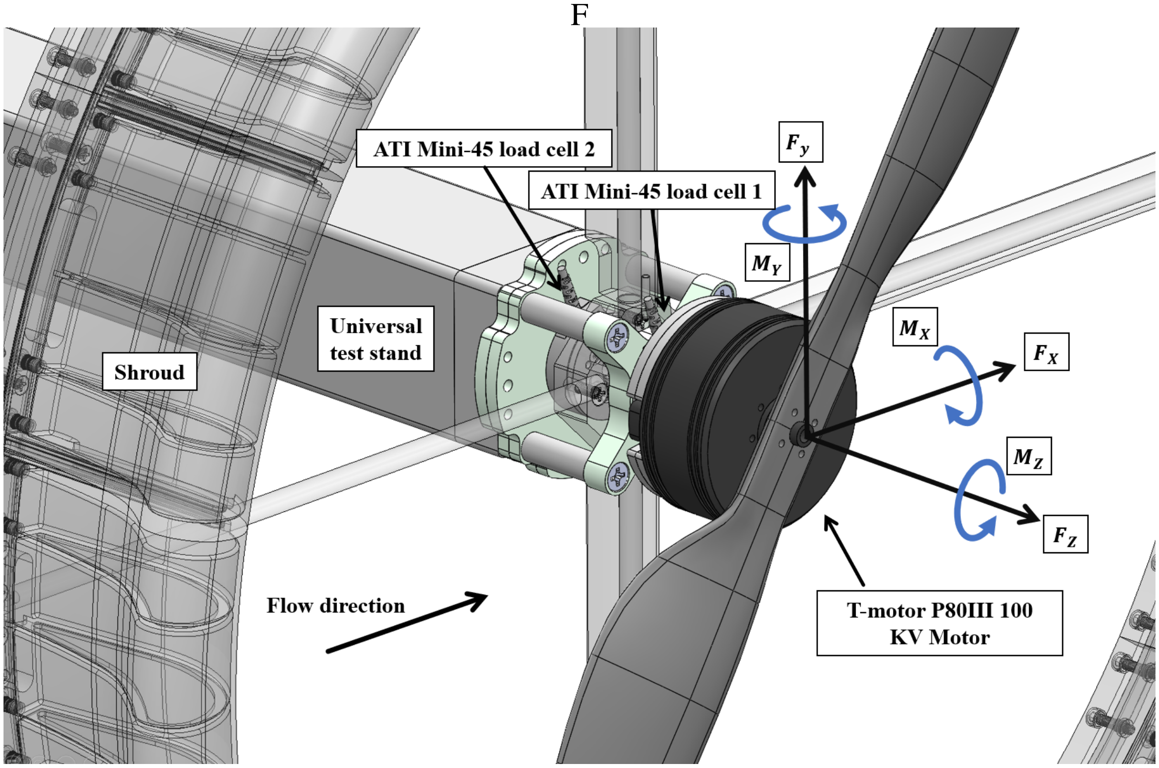

Figure 2.10: Rotor and shroud mounting hardware.

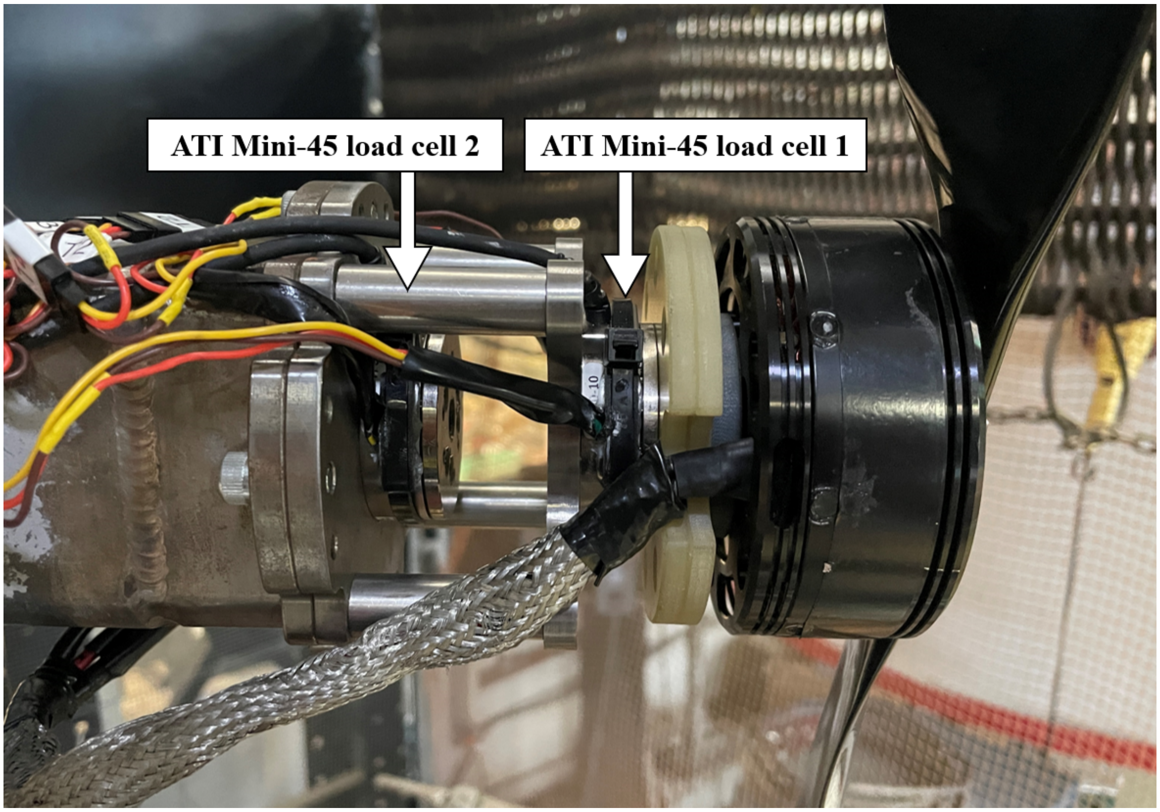

Figure 2.11: Load cell 1 and 2 for measuring 6 degree of freedom loads of shroud and rotor separately.

As shown in Figure 2.11, two load cells were used to measure uncoupled loads, one for the rotor and one for the shroud. The structure was designed with standoffs to ensure sufficient clearance between the shroud and the rotor load cells. Both load cells are mounted directly to the test stand and are therefore not mounted to one another. This simplifies post processing as the load readings from one load cell do not need to be subtracted from the other as would be necessary if the load cells were mounted in series.

Figure 2.12 shows how to secure the motor to the load cell and stand. The assembly was designed to limit structure in the wake of the rotor. Thus, countersunk screws were used to remove screw head interference in the interface. The procedure for assembly is as follows: 1) The motor is fastened to the first structural plate. 2) The load cell is mounted to a second structural plate. 3) The plates with the motor and load cell are fastened together to form one unit. 4) The assembly is mounted to the test stand adapter which is then secured to the test stand.

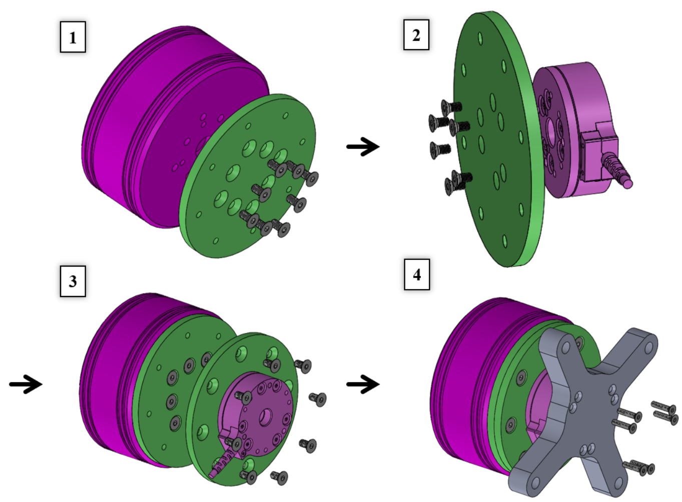

Figure 2.12: Assembly of load cell and motor.

The structure used to test the isolated rotor shown in Figure **??** was also used to test the shroud. To mount the shroud, no additional structure was required other than the shroud itself which included four struts for mounting to a second load cell. In this setup, a second ATI Mini-45 load cell was used to measure isolated uncoupled shroud loads. This was done to determine the contribution of loads from the rotor and the shroud separately which is useful in validating CFD results, distinguishing frequencies of either system, and ultimately informing final vehicle design decisions related to structures and aerodynamic performance.

A 3-D printed fairing surrounds the assembly to limit downwash interference as shown in Figure 2.13. To power the motor, a Jameco 48 V 210 amp AC-to-DC switching power supply was used to match a 12S battery which the motor and ESC would typically be powered by [23]. To control the DC output, a relay was installed which could be remotely turned on and off from inside the control room. To limit electrical noise, the DC power cable running up to the ESC was shielded and grounded.

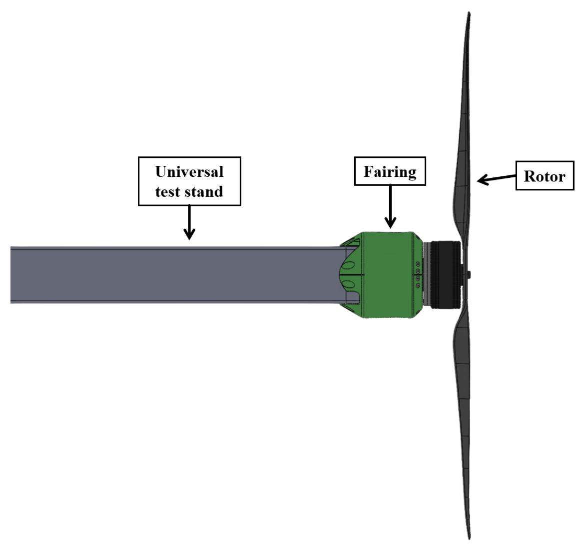

Figure 2.13: Fairing shown in green designed to limit downwash interference effects.

Table 2.1: Test component weights.

Component	Weight (kg)
Shroud 3D printed plastic	4.54
Shroud steel structure	3.17
T-motor motor	0.65
Fairing	0.2
G-10 insulation	0.15
T-motor rotor	0.05

2.1.5 Data and Control System

In addition to RPM and rotor loads, motor voltage and current were measured to quantify electrical efficiency. Both the current and voltage sensors are mounted near the ESC to limit voltage loss in the cable for an accurate reading. Because of heating caused by the motor, it is important to record load cell temperature drift to get a sense for drift in load cell output voltages. Thus, two 10K ohm thermistors were installed on the outer housing of the load cell. A single shielded cable was used to transmit all of the signals to a Texas Instruments NI Data Acquisition (DAQ) module. Because of the limited number of channels, a second DAQ was used to measure all load cell output voltages. Lastly, while in the wind tunnel, barometric pressure, ambient temperature, humidity, and dynamic pressure were recorded to a third DAQ located in the control room. These values would later be used to determine air density, temperature, and flow velocity.

A diagram of the complete data and control system is shown in Figure 2.14. To spin the rotor, the operator enters an RPM in LabVIEW and the motor slowly accelerates and stabilizes on the desired RPM automatically as described later in Section 2.1.7.

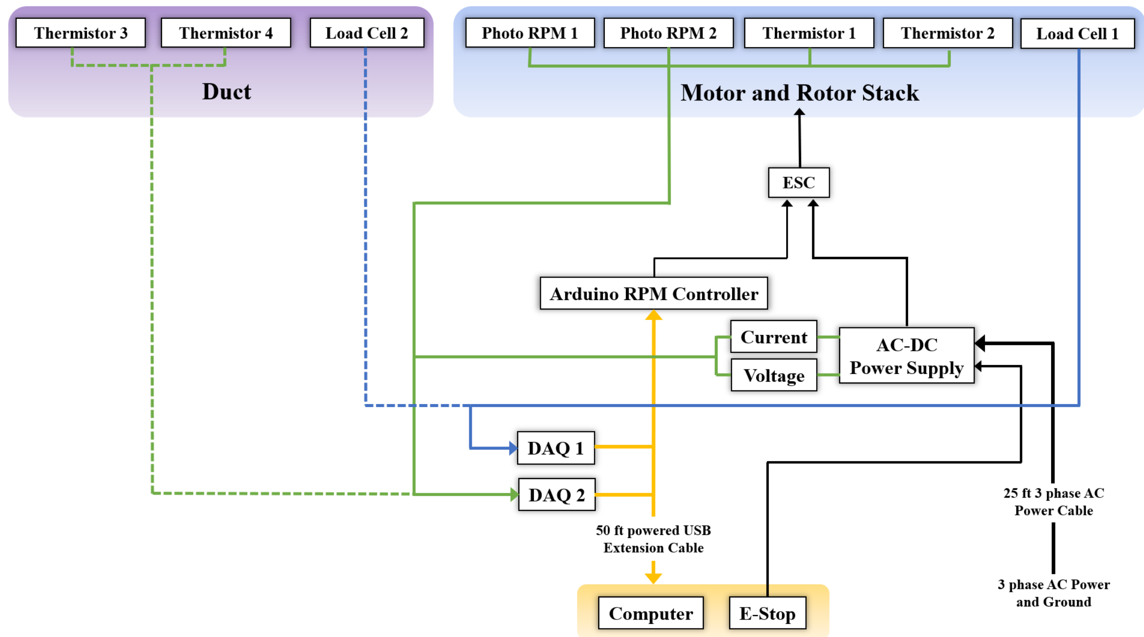

Figure 2.14: Data and control system of test stand.

2.1.6 Data Acquisition & Virtual Instrument Panel

Connected by 50 ft USB cables, the operator was able to control the setup from the control station as shown in Figure 2.15. Results were recorded at a 3 kHz sampling rate using a National Instruments USB-6251 (16 bit, 1.25MS/s) USB Multifunction I/O device as shown in Figure 2.16. Raw voltages were saved in addition to dimensional data that was processed within the Data Acquisition software LabVIEW. Redundant raw voltages were saved such that in the event of an incorrect calibration or other issues, the raw voltages could still be used to recalculate dimensional values in post processing.

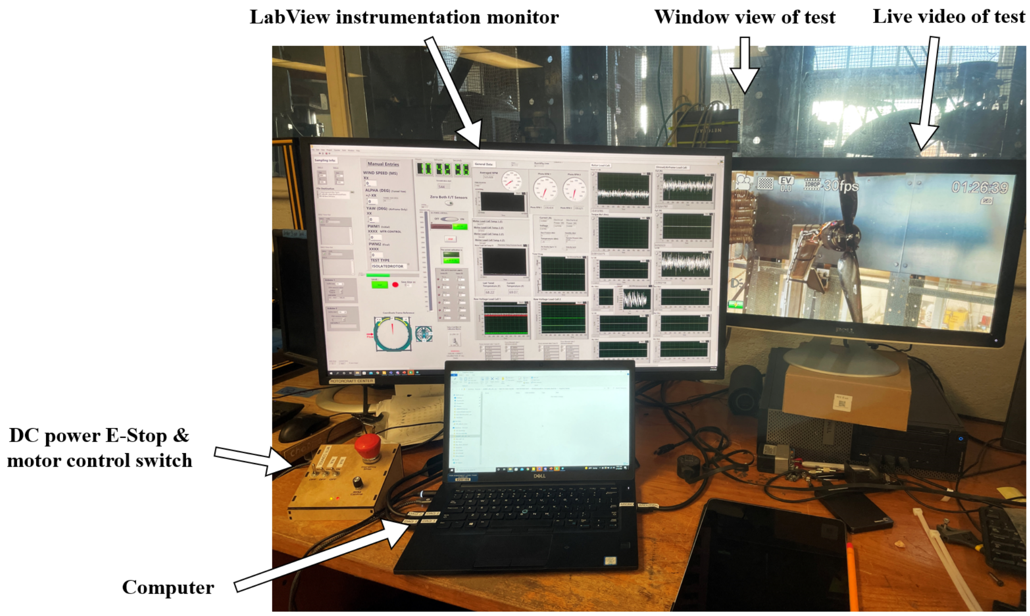

Figure 2.15: Operator test station.

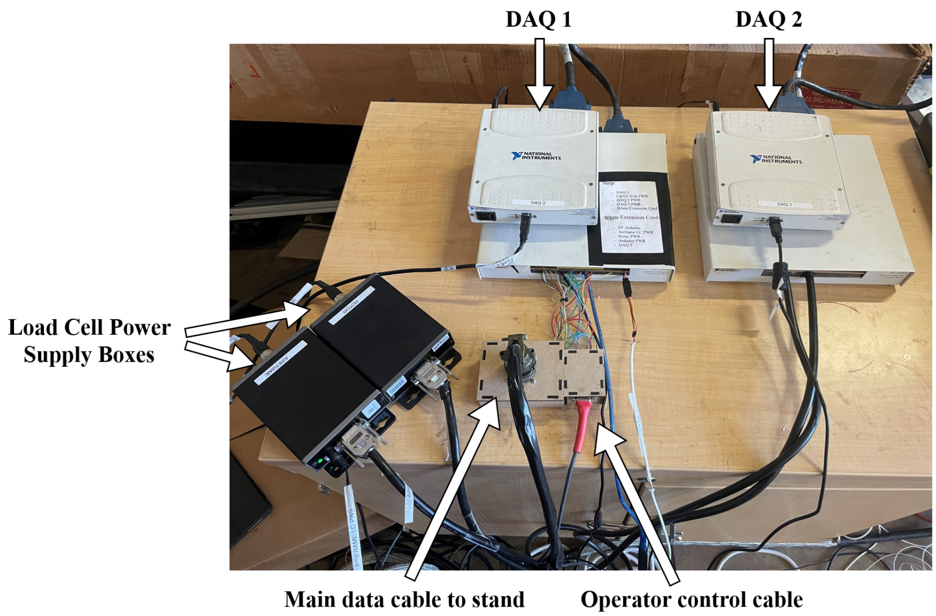

Figure 2.16: Data acquisition units and cabling.

The LabVIEW virtual instrument panel was used for prescribing inputs and monitoring live outputs. In general, many of these inputs and outputs had visual design features to alert the operator of any potential issues and avoid mismatching between the actual test parameters and the specified parameters used to classify the saved data. These design features are especially important to avoid confusion given the time constraints of a wind tunnel test.

Figure 2.17 shows a detailed close-up view of the operator inputs in the full LabVIEW instrumentation display. Sampling rate and save file location are the first two entries. For test conditions, the user may input: Wind speed, angle of attack, yaw angle, target RPM, and test type. These input parameters were then used to classify the saved output files for post processing. To avoid operator error, the target RPM entry was used to control the actual rotor RPM in addition to classifying the saved data, thereby ensuring the saved data would never be mismatched with the actual RPM of the test. As a further precaution, the input alpha angle was shown visually with a dial indicator to avoid coordinate frame reference confusion. The save button and save time entry is located beneath the manual test parameter entries. On the right side is a clock, a button to zero the load cell force and moment outputs, and a switch to turn the DC power to the motor on and off. The calibration for the second Mini-45 can be selected based on the load limits expected and the resolution required for the specific test. This will switch the calibration matrix according to the preferred calibration for the test. A visual indicator was also included to remind the operator of the calibration matrix selected. Lastly, load limit expectations for all six forces and moments can be entered for the software electric power cut-off safety feature.

Figures 2.18 and 2.19 shows the visual outputs. These outputs were displayed to monitor sensor health in real time and provide quantitative feedback for different test conditions. Starting with Figure 2.18 the visual outputs include: RPM, RPM controller error, and load cell temperature. To track the approximate force and moment reading drift, the temperature of the load cell when it was last tared and the current temperature is shown side by side. The raw voltages for both load cells are plotted to ensure they are operating properly and not saturated. Electrical current, voltage, and power are shown to monitor sensor health. From the wind tunnel, the ambient air temperature, density, humidity, and dynamic pressure are shown. Lastly, an approximate drag value is calculated and plotted based on the wind tunnel turn-table angle of attack and measured forces to assist with trimming the rotor thrust.

Figure 2.19 shows the six force and moment outputs for the two load cells. The purpose of the first load cell is to measure rotor loads while the second load cell can measure either the shroud or TRV-80 airframe depending on the test configuration.

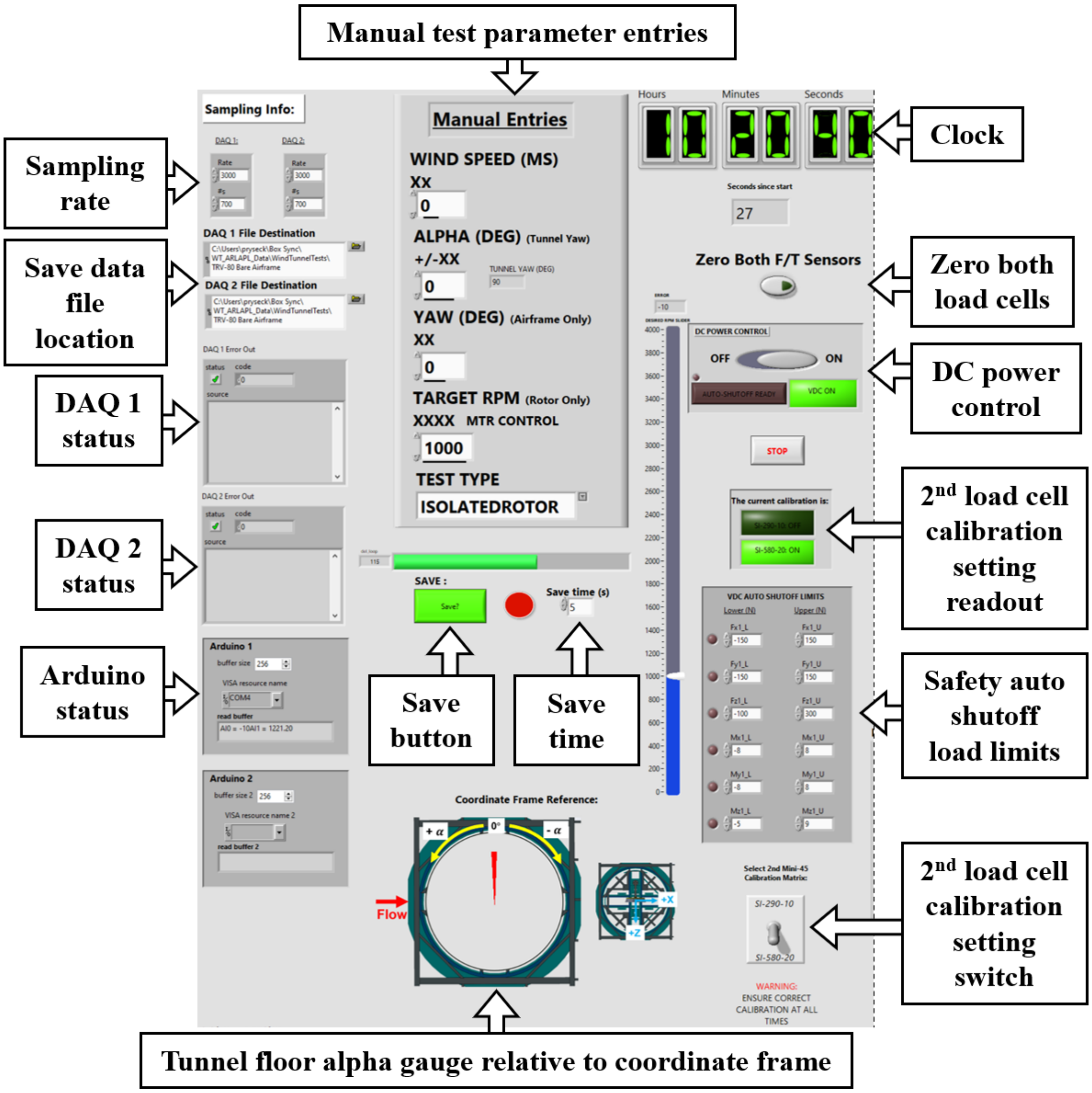

Figure 2.17: Operator inputs on LabVIEW virtual instrumentation display.

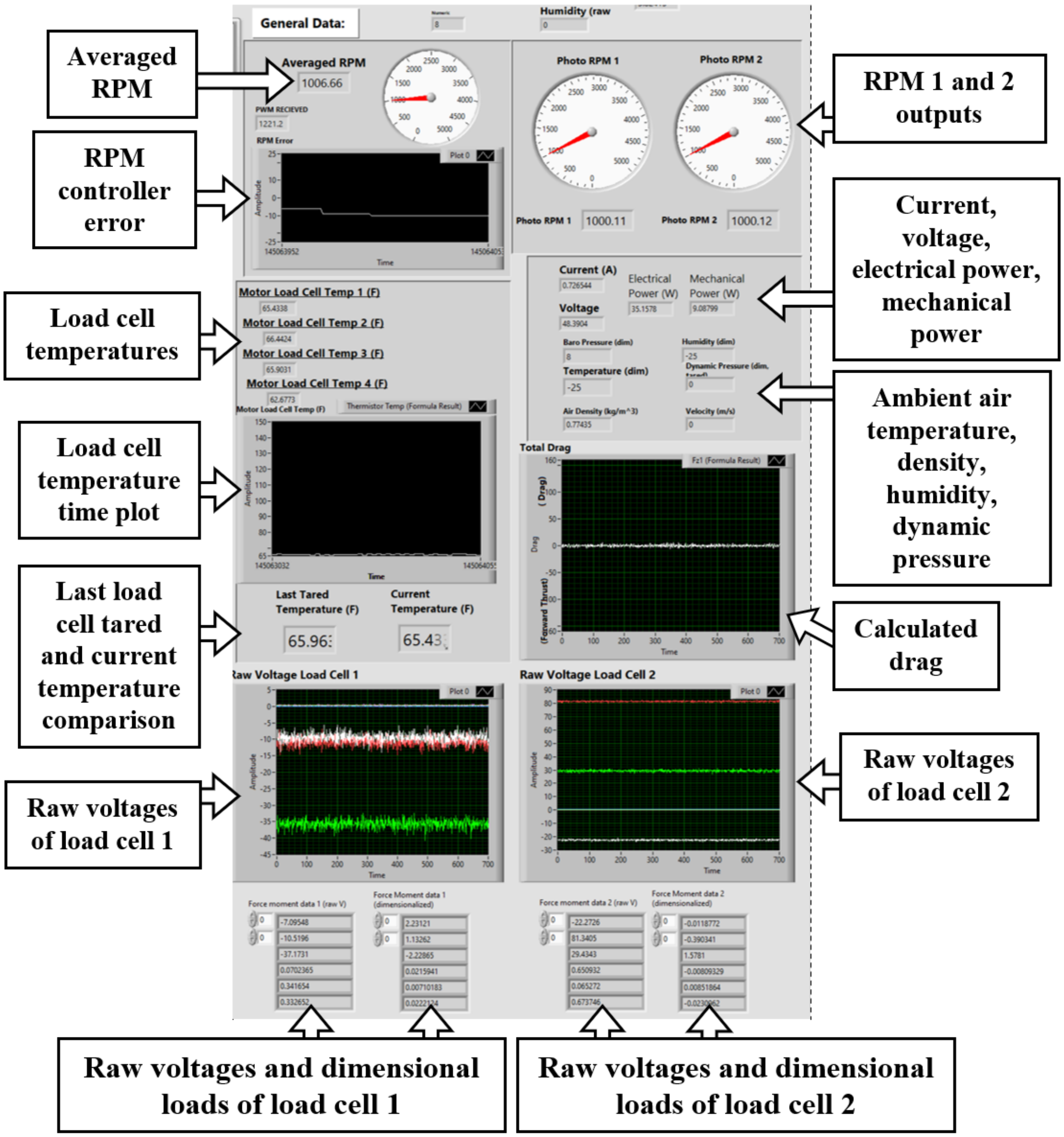

Figure 2.18: General data output on LabVIEW virtual instrumentation display.

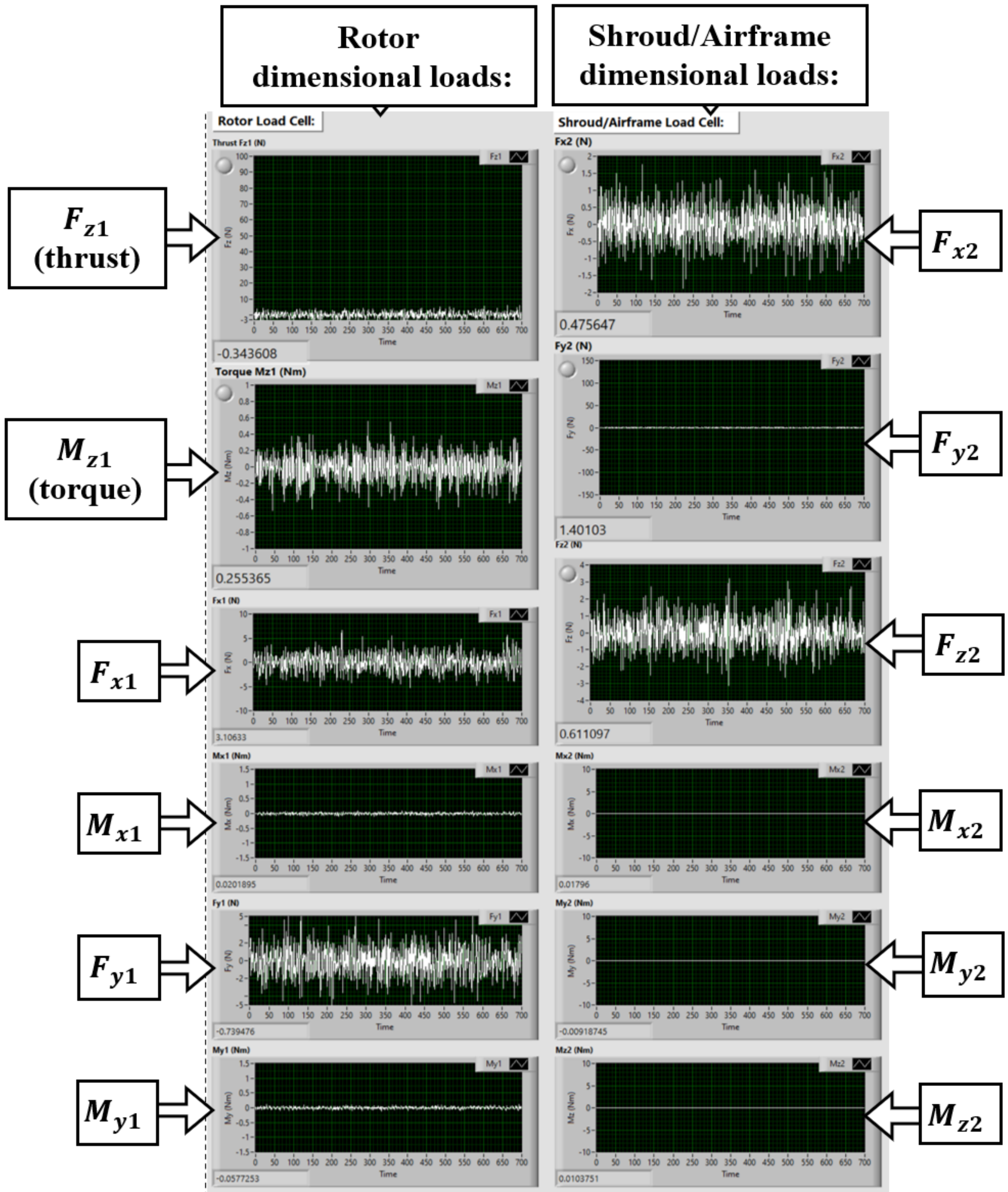

Figure 2.19: Force and moment output on LabVIEW virtual instrumentation display.

2.1.7 Rotor RPM Controller

Two infrared reflective (IR) sensors located next to the motor were used to measure the RPM of the motor and were averaged within LabVIEW. Two sensors were used for redundancy in case one fails while testing in the wind tunnel. In addition, the two sensors can be compared to ensure that the readings are in good agreement. To control the rotor RPM, a controller was implemented on a Teensy Arduino using RPM readings sent via serial communication from LabVIEW. The controller utilizes a proportional integral (PI) implementation where an outer loop frequency reading from the IR sensors generates RPM readings for an inner loop rate controller, thereby adjusting the pulse-width modulation (PWM) signal sent to the ESC. The control loop is shown in Figure 2.20.

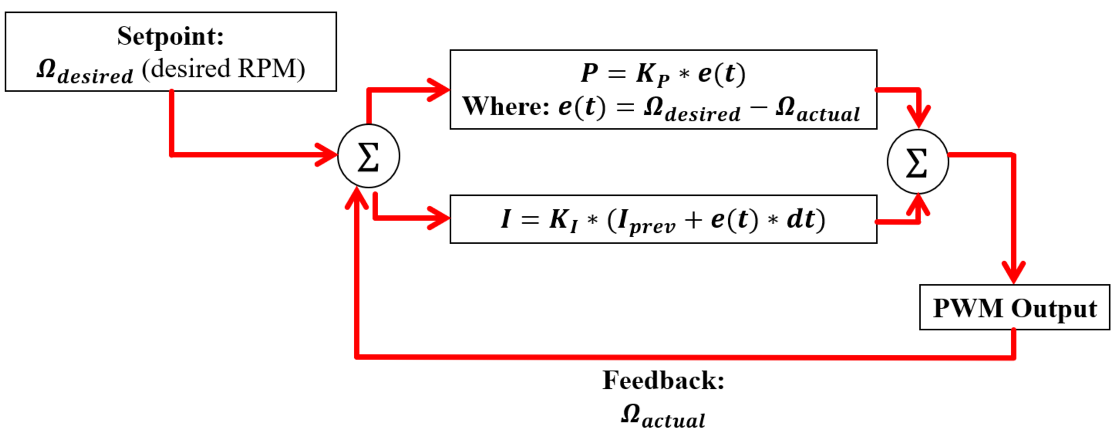

Figure 2.20: PI controller stabilizing on RPM setpoint.

2.1.8 Bare Test Stand Modal Analysis

Before constructing the steel test stand, a modal analysis was performed to determine the resonant frequencies and mode shapes. Because the stand is used for different test articles with different masses, the purpose of this modal analysis was to form a baseline understanding of the mode shapes and resonant frequencies to assist with the design of test hardware such as the shroud. The modal frequencies were found to be 23 Hz (1380 RPM), 23.3 (1400 RPM), 74 (4440 RPM), and 122 Hz (7330 RPM).

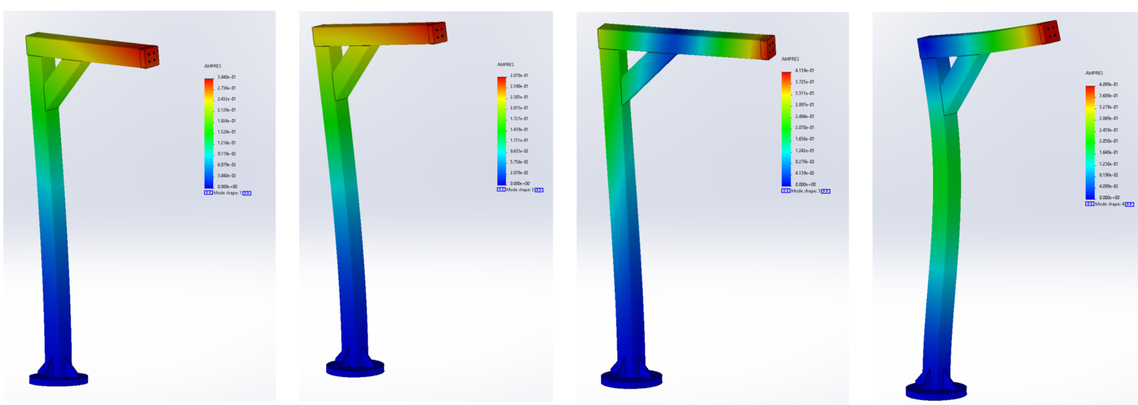

Mode 1: 22.98 Hz **Mode 2: 23.35 Hz** **Mode 3: 73.99 Hz** **Mode 4: 122.12 Hz**

Figure 2.21: Mode shapes of the universal test stand.

2.1.9 Test Stand Structural Testing and Resonant Frequency Identification

To ensure the stand would be capable of withstanding expected static loads in the wind tunnel, the stand was pulled in the two primary aerodynamic drag directions as shown in Figure 2.22. A laser sensor was used to determine the approximate deflection as a result of the static loading. Ratchet straps were used to pull on the stand with crane scales to measure the applied tension. The maximum drag loads were predicted based on the TRV-80 bare airframe area. Actual tested loads went beyond the predicted loads by about 20% and minimal deflection was found.

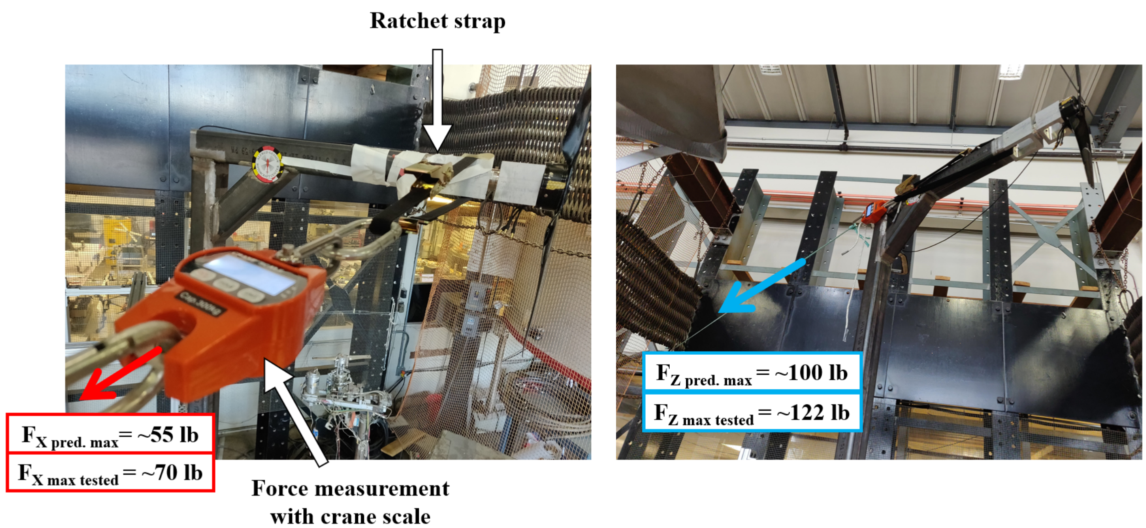

Figure 2.22: Test stand pulled in two notional drag directions to ensure sufficient structural stiffness prior to wind tunnel entry.

A rap test was performed to determine the natural frequency of the stand with the motor and rotor mass included. An ATI Mini-45 load cell was used to measure the frequencies with a log rate of 5 kHz. A Fast Fourier Transform (FFT) was applied to the measurements to determine vibratory output in the frequency domain. The rap test torque output in the time domain is shown in Figure 2.23 and the frequency output is shown in Figure 2.24. Multiple tests were conducted and results were found to be repeatable. The frequencies as a function of 1/rev RPM are listed in Table 2.2.

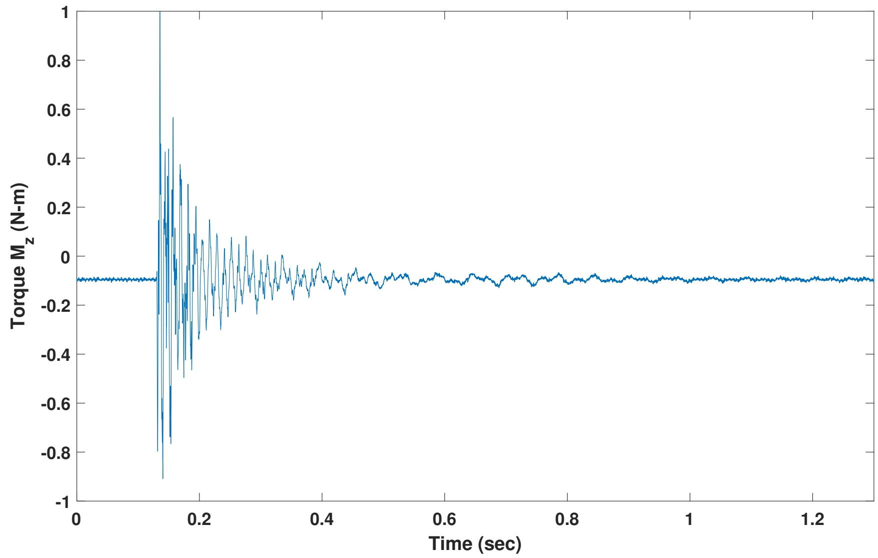

Figure 2.23: Impulse response of torque M_z.

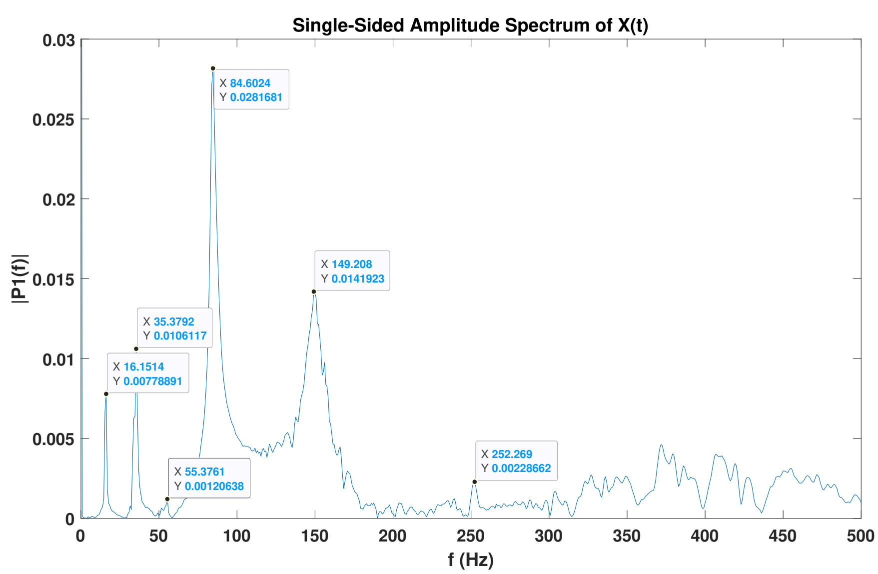

Figure 2.24: Fast Fourier Transform (FFT) of test stand with motor and rotor.

Table 2.2: Test stand natural frequencies found from rap test.

Test Stand Natural Frequencies (RPM)
960
2100
3300
5000
5700
8700

2.1.10 Thermal Drift Reduction for Electric Motor and Load Cell System

Background and Thermal Test Procedure

Because of intermittent motor heating over time, Garolite G-10 plates were used to thermally isolate the motor and load cell. For the intial test setup, the plate thickness was set such that with these plates installed, the load cell experiences 2 to 3°C fluctuation throughout each run. In the final setup, additional insulation was added so that less than 1°C fluctuation occurs throughout each respective run, while the motor can fluctuate 10 to 15°C.

To quantify the temperature drift, thermistors were mounted to both the rotor load cell and the shroud load cell. Four thermistors were used in total, with two mounted to the outer housing of either load cell for redundancy and to ensure good agreement in temperature reading between the two load cells (Figure 2.26). In all tests, readings between the two thermistors varied by less than 1°C and were averaged. Ideally, the thermistors would be placed near the strain gauges inside the load cell for a more accurate reading, but in practice the most accurate point of measurement was the outer housing.

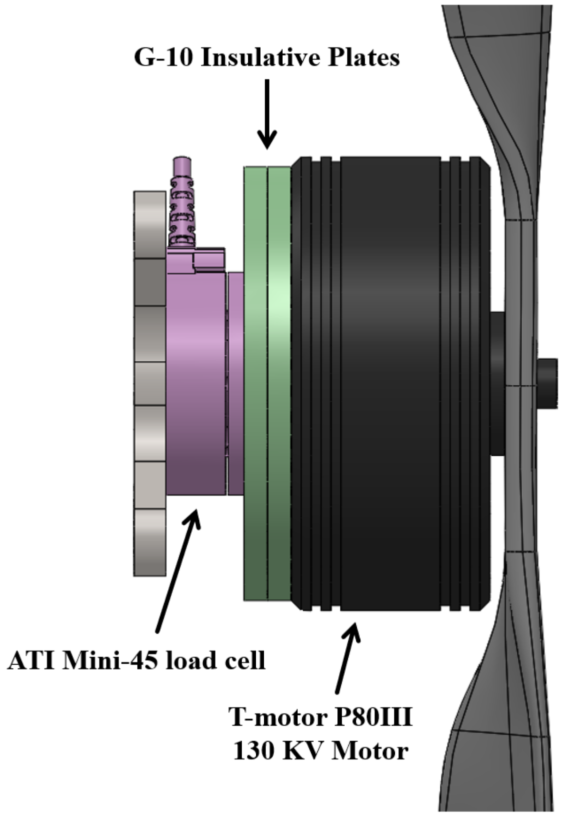

Figure 2.25: Garolite G-10 plates used to isolate the load cell from the motor.

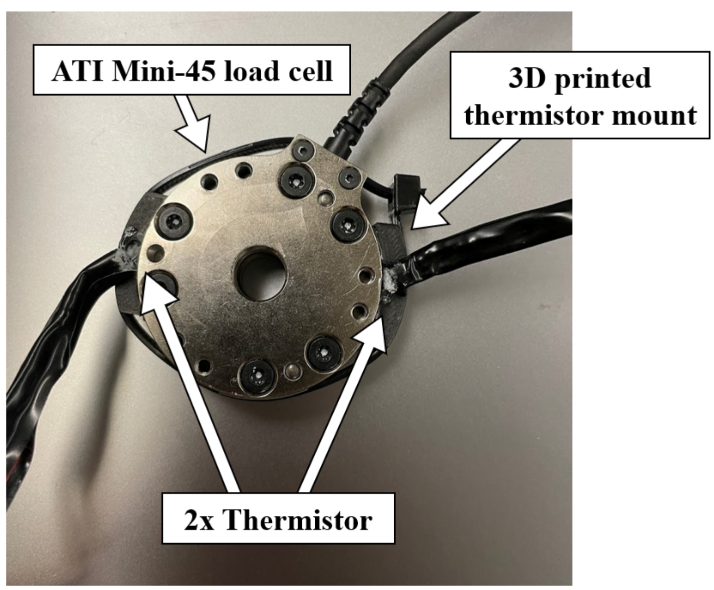

Figure 2.26: Two thermistors mounted to outer housing of load cell.

Tests were conducted in a hover configuration outside of the wind tunnel to investigate the load cell drift due to temperature fluctuation. Thus, these tests do not include wind tunnel free stream radiative cooling, although these effects can only be beneficial.

The test procedure is as follows: After an intial warmup run, a single test was conducted over a period of 10 minutes while collecting transient load cell and thermistor data. 10 minutes was chosen as it was the approximate length of time required to collect desired test data in the wind tunnel between load cell tares. The rotor was spun to 2300 RPM for 20 to 30 second intervals, with breaks between 2300 RPM runs wherein the RPM was either increased or decreased. This was done to capture motor temperature fluctuation due to internal heating and radiative cooling.

Initial Test Setup Insulation

For the initial test stand, 10 mm of insulative G-10 plate thickness was used to isolate the motor and load cell from heat transfer. Figure 2.27 shows a 10 minute hover run with varying RPMs. The intial 2300 RPM run logged between 30 and 60 seconds shows an approximate force $F_z = 34$ N. Repeating the same 2300 RPM 8 minutes later between 460 and 480 seconds, the force measured was 41 N, resulting in 7 N (20% increase) of drift. This was repeated multiple times with varying RPMs and the same approximate linear trend was found. Rotor torque M_z was found to have insignificant drift as shown in Figure 2.28. Temperature reading also fluctuated throughout the test, most likely due to rotor wash cooling and internal motor heating. As described earlier, it is likely the internal strain gauges of the load cell do not experience the same temperature fluctuation as the outer housing because the load cell force drift is linearly constant. However, it is clear that the temperature increases 2.5 °C over the 10 minute test based on the initial and final temperatures recorded.

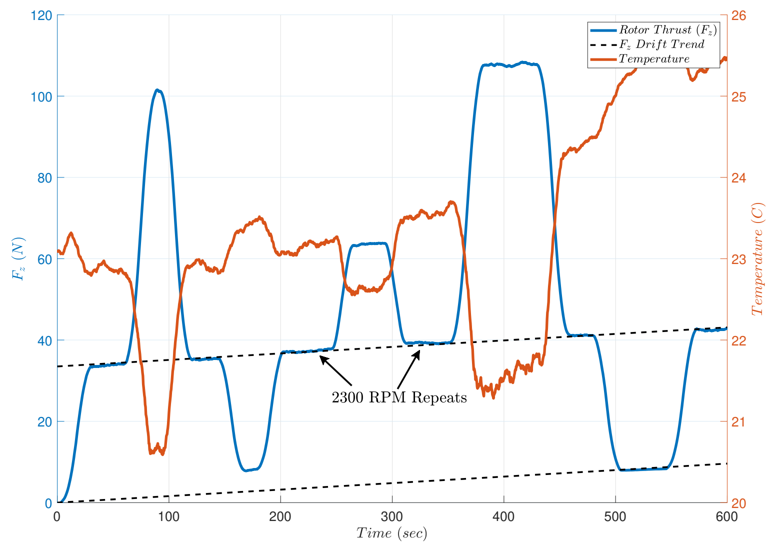

Figure 2.27: F_z (left y-axis) and temperature (right y-axis) versus time. F_z drift was found to be linear with a slope of $m = 0.016$ N/sec.

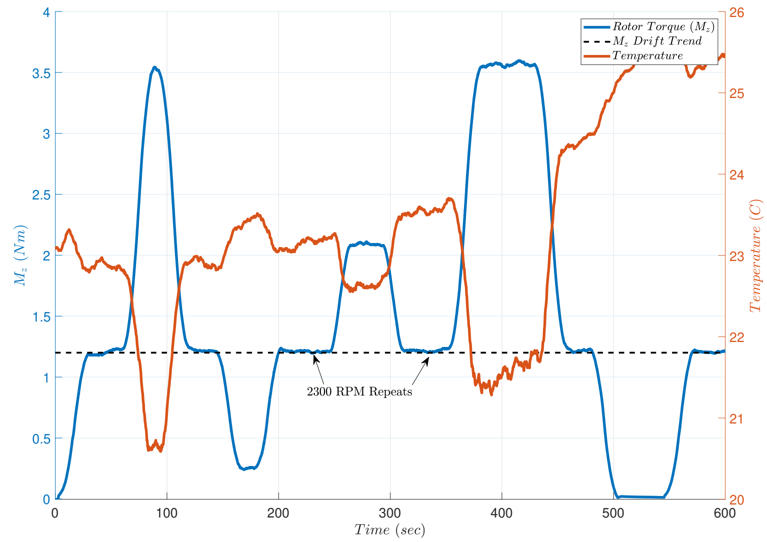

Figure 2.28: M_z (left y-axis) and temperature (right y-axis) versus time. M_z drift was found to be negligible.

Final Test Setup Insulation

To reduce this temperature drift, an additional 1/4 inch Garolite G-10 insulation was added between the motor and load cell. The plate was made with a diameter smaller than that of the motor in order to expose the cooling holes on the bottom of the motor for additional cooling. An image of the test setup with and without the additional insulation plate is shown in Figure 2.29.

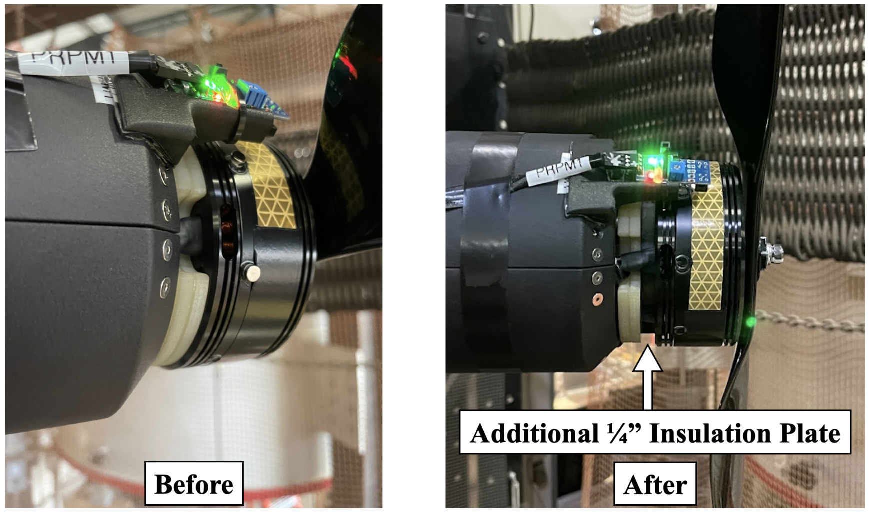

Figure 2.29: Motor and load cell assembly before and after adding additional 1/4 inch insulation plate.

From Fourier’s Law for heat conduction, Equation 2.1 for thermal resistance can be derived, where R_θ is the absolute thermal resistance (K/W) across the thickness, Δx is the thickness (m), A is the cross-sectional area (m^2), and k is the thermal conductivity W/(K·m) of the sample.

$$R_\theta = \frac{\Delta x}{A \times k} \tag{2.1}$$

By adding the additional 1/4 inch plate, Δx is increased from 10 mm to 16 mm, thereby increasing the thermal resistance by 60%. Additionally, the decreased cross sectional area of the plate was decreased from 60 cm^2 of the original plates to 20 cm^2. This also exposed the motor cooling holes which further reduced the heat transfer.

Again, the same 2300 RPM repeat test procedure described in section 2.1.10 was run to quantify the load cell drift over time with the greater insulation. Results shown in Figure 2.30 indicate a 60% decrease in thermal drift over the initial test setup with the modifications. As earlier, the initial 2300 RPM run logged between 30 and 60 seconds shows an approximate force $F_z = 34$ N. Repeating the same run 8 minutes later between 460 and 480 seconds, the force measured was 36.5 N, resulting in 2.5 N (7% increase) of drift. Similar drift was found by Haag when testing with a high-power electric propulsion device and load cell setup [24]. This is significantly reduced compared to the initial drift of 20% following the same procedure with the original setup. Temperature change is also reduced, showing less than 1 °C increase from the initial and final temperature. This procedure was repeated multiple times with varying RPMs and the same approximate linear trend was found. Moment M_z was again found to have insignificant drift as shown in Figure 2.31.

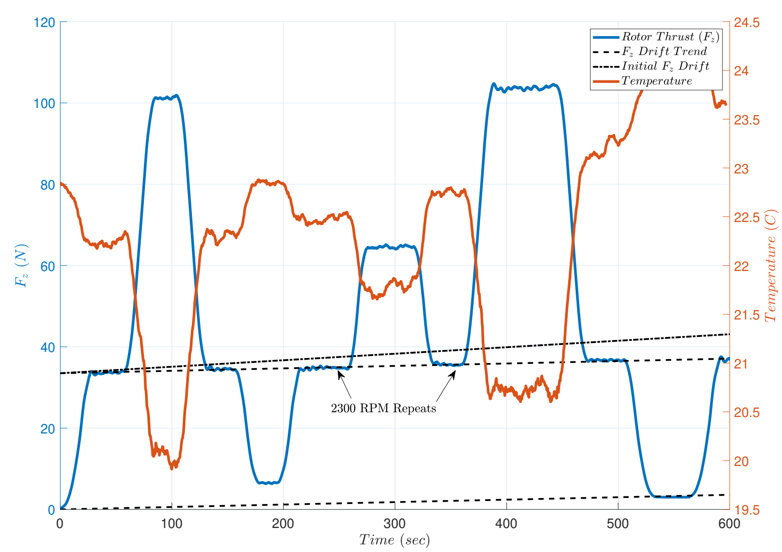

Figure 2.30: F_z (left y-axis) and temperature (right y-axis) versus time. F_z drift was found to be linear with a slope of $m = 0.006$, a 60% decrease over the initial test setup drift of slope $m = 0.016$.

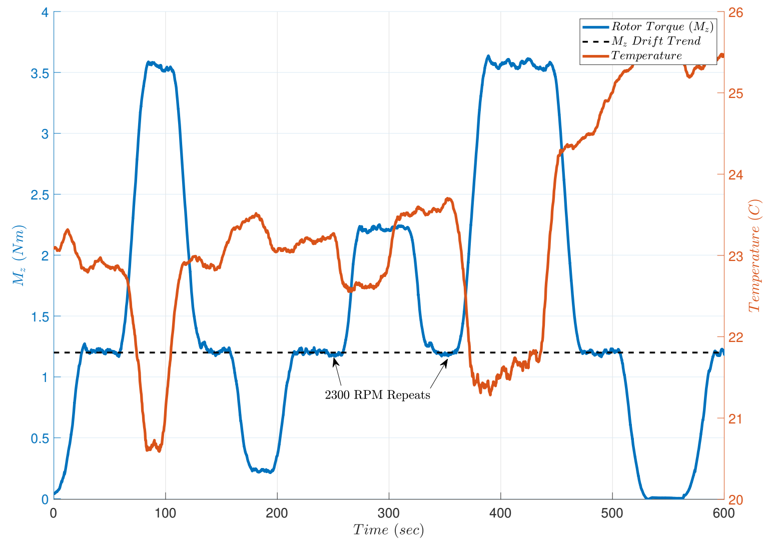

Figure 2.31: M_z (left y-axis) and temperature (right y-axis) versus time. M_z drift was again found to be negligible.

Thermal Drift Conclusions

Based on the results of these hover tests, it is clear that the load cell drift is linear in trend and significantly reduced with the test stand modifications. It is also clear that the drift accumulates with time running the motor. Thus, data collected earlier in the test immediately after tare can be considered more accurate than runs performed later.

To correct for the drift in wind tunnel data, two approaches can be taken: 1) Data can either include error bars which account for the expected drift found in these tests or 2) the drift can be subtracted out based on an initial tare 0 RPM run and a repeated tare 0 RPM run at the end of the specific test sequence. The latter procedure is similar in methodology to the wind tunnel test performed by Russell [12]. Figure 2.32 shows example uncorrected and corrected data required due to a temperature increase of 4.5 °C (54.6°F to 62.9 °F) over the span of the run as was found by Russell. After correction, the final static point differed from the initial static point by 0.003 lb. Ultimately, the second method of subtracting out the drift based on tare data was used in this study to account for load drift due to temperature variation. In addition, a warm up run was conducted prior to testing wherein the rotor would be spun for over 10 minutes to bring all components closer to thermal equilibrium, thereby reducing drift. For tests outside of the wind tunnel on a hover stand, tests never exceeded 1 minute in length, thus, thermal drift was found to be minimal.

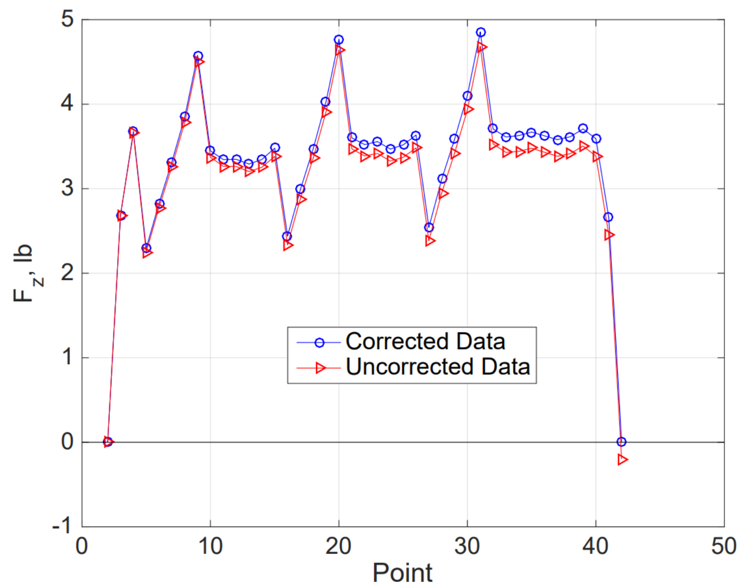

Figure 2.32: F_z drift with and without temperature drift corrections [12].

2.1.11 Test Safety and Fault Tolerance

Multiple safety measures were implemented to limit any potential risk involving the high RPM rotor. First, a software E-stop was integrated into the LabVIEW data recording system which would trigger the power supply relay if a recorded load fell outside of the specified range. Second, a software and physical push button E-stop could be used to trigger the power supply relay. Third, two sets of fuses in the AC three phase and DC power cable were installed in the event of a short circuit scenario. Fourth, a camera was used with a live video feed to visually monitor the rotor while testing. Lastly, a 3 inch thick wooden and polycarbonate barrier protected operators in the control room from the model.

Fault tolerance measures were also implemented to ensure tests could continue if a sensor were to fail. These include dual-redundancy for RPM measurement and load cell temperature reading. General fastener hardware also incorporated dual redundancy on any critical attachments or fixtures such as the rotor to motor mount.

2.2 Test Articles

2.2.1 Rotors

Two rotors were used in this study. The first rotor is a commercial-off-the-shelf (COTS) T-motor 28 inch (0.71 m) diameter ('28x9.2') used on the TRV-80 platform. (The value of 9.2 in the rotor name is used to classify the pitch of the rotor in a simplified manner. That is, with each full rotor rotation, the rotor moves forward 9.2 inches.) The second rotor was fabricated in-house with a NACA0012 airfoil to serve as a comparison. A NACA0012 airfoil was chosen because it is well understood and would therefore serve as a good comparison. In addition, the NACA0012 airfoil is has a variable collective mechanism which the T-motor rotor does not. The rotor geometry and collective angles for the NACA0012 custom blade were selected to best match the T-motor rotor for a relatable comparison. The thrust weighted solidity for both the T-motor rotor and NACA0012 rotor were compared using Blade Element Momentum theory to ensure the thrust operating range would be similar. The NACA0012 blade twist is linear and matches the θ_{75} blade twist of the T-motor rotor. The chord length of the NACA0012 blade also matches the $\frac{r}{R} = 75\%$ chord length of the T-motor rotor. A mechanism to adjust the collective manually was manufactured to test four different θ_{75} positions spaced in three degree increments: $\theta_{75} = 5°$, $8°$, $11°$, and $14°$. These collective angles were chosen to cover the blade element alpha range of the T-motor rotor. The rotor geometries for normalized chord length, normalized thickness and twist are shown in Figures 2.33 - 2.35.

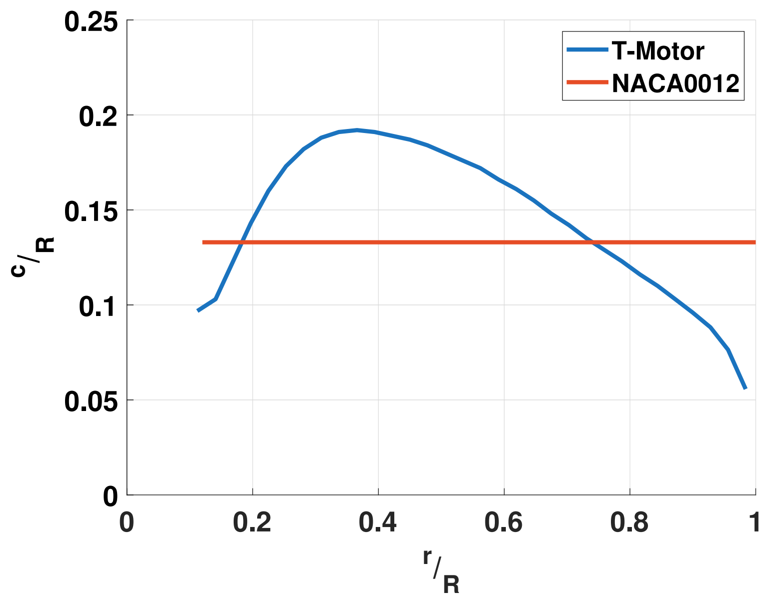

Figure 2.33: Normalized airfoil chord vs. span location.

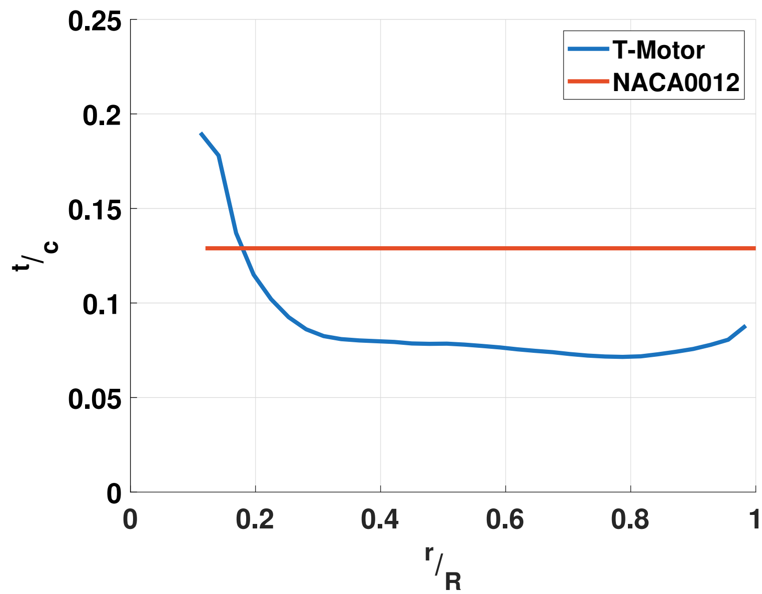

Figure 2.34: Normalized airfoil thickness vs. span location.

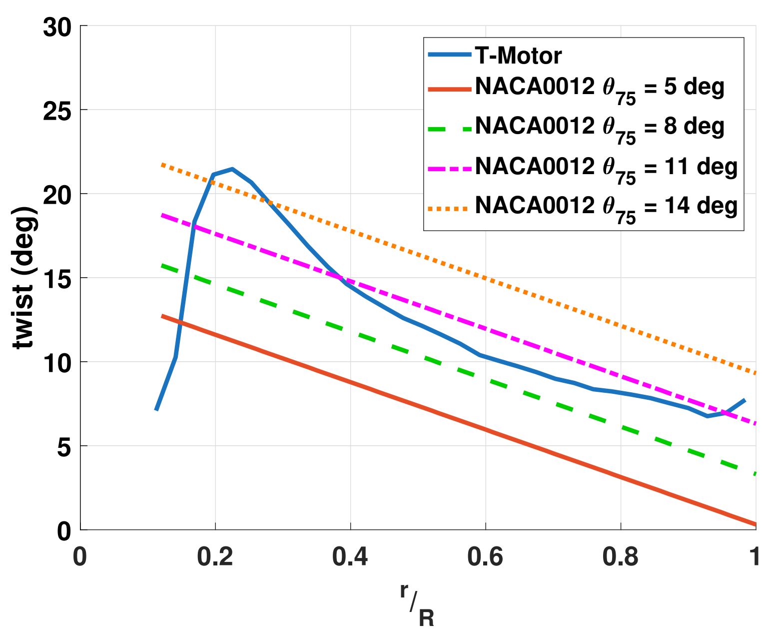

Figure 2.35: Twist vs. span location.

The NACA0012 rotor consists of a dense foam core wrapped in adhesive and +45/-45 and +90/-90 carbon fiber prepreg for maintaining torsional stiffness, bending stiffness and carrying the centrifugal loads. The foam core is made from Rohacell 31 and carbon fiber from 3K-70-CSW ±45 degree graphite-epoxy composite plies using Cytec FM 300 adhesive film for adhesion between the foam and carbon fiber. As shown in Figure 2.36, an aluminum root insert was embedded inside the blade to serve as a hard point for mounting to the blade grip. To ensure sufficient centrifugal loading stiffness, the blade was pulled from the root insert with varying weights as shown in the experimental test setup in Figure 2.37. These weights were tested without failure up to an equivalent inertial load of 3000 RPM.

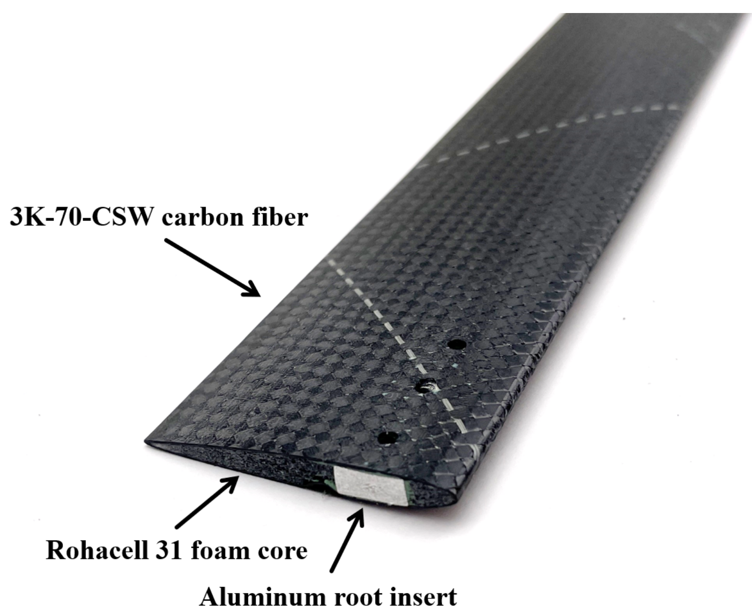

Figure 2.36: NACA0012 rotor blade cross section.

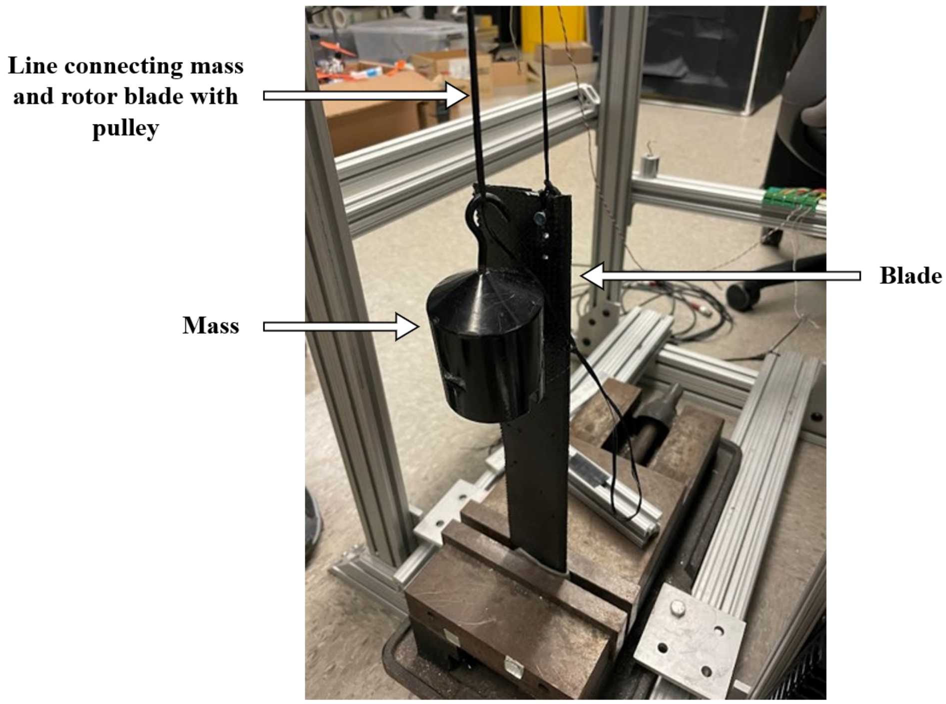

Figure 2.37: Centrifugal loading bench test.

The NACA0012 blade fabrication process is shown in Figure 2.38. The procedure is as follows: 1) A blank sheet of Rohacell 31 foam is cut to the approximate size. 2) The foam is inserted into an aluminum blade mold which is then clamped together and placed in an oven at 350 °F (177 °C) for one hour. 3) After cooling, the foam core is removed from the mold and trimmed. A rectangular section at the root is precisely cut out to allow room for the aluminum root insert. 4) The blade is wrapped in prepreg carbon fiber and a layer of release fabric is used to cover the blade for easy removal from the mold post cure. The blade is then placed back in the aluminum mold, clamped together and again placed in the oven at 350 °F (177 °C) for 1.5 hrs. 5) After cooling, the blade is removed from the mold.

6) The blade is trimmed to match the geometry of the second blade. Weight and balance checks follow to limit 1/rev vibration.

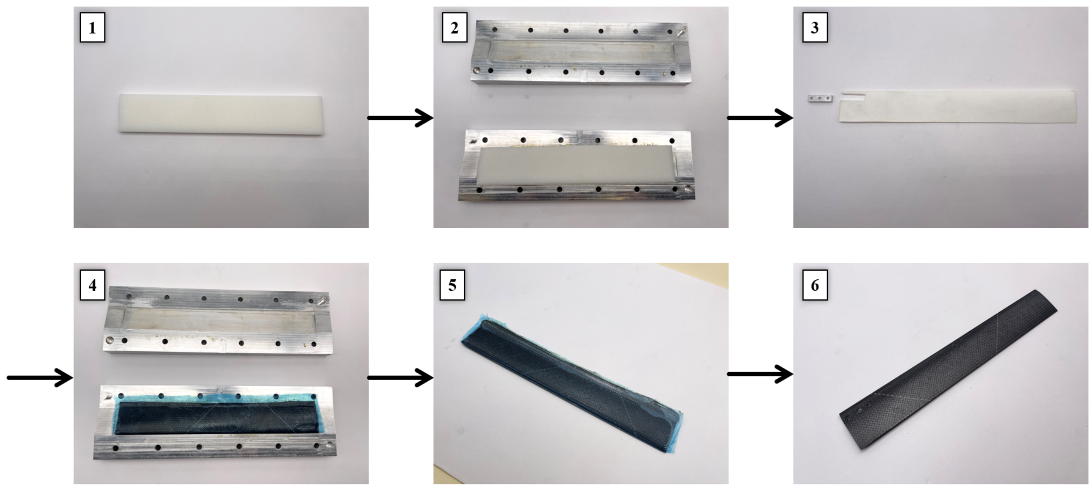

Figure 2.38: NACA0012 carbon fiber blade fabrication process.

The final NACA0012 rotor blade is compared with the T-motor blade in Figure 2.39. The T-motor blade is manufactured as a single part and has a fixed pitch. The NACA0012 rotor blade requires additional parts but allows for the collective pitch angle change. The assembly and exploded view of this mechanism is shown in Figure 2.40. The symmetrical assembly consists of three aluminum mounts and a 3D printed shim to match the contour of the surface of the airfoil to the flat surface of the aluminum fixture. Figure 2.41 shows the NACA0012 rotor mounted to the universal test stand.

Figure 2.39: Top view scale comparison of NACA0012 rotor blade (top) and TRV-80 T-motor ‘28x9.2’ rotor (bottom).

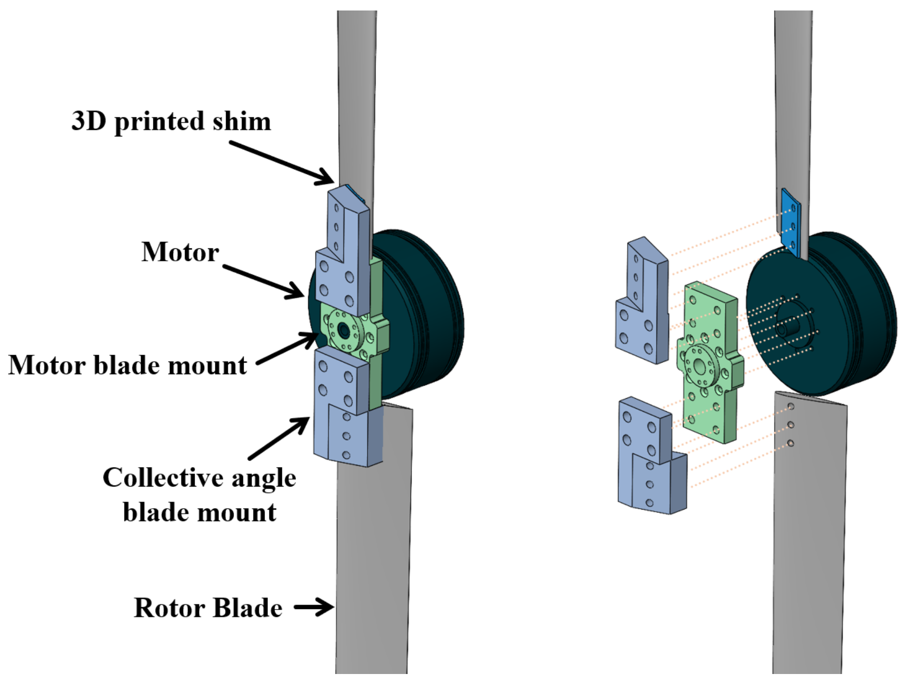

Figure 2.40: NACA0012 manually adjustable collective blade mount assembly (left) and exploded view (right).

Figure 2.41: NACA0012 rotor blade mounted to motor with aluminum mounts.

2.2.2 Shroud

Design

The model was designed based off a NASA shroud and was scaled 75% to fit a 28 inch diameter rotor as shown in Figure 2.42 [25]. Because the goal of the design was to validate Helios CFD, the shroud was not designed to maximize performance and was therefore only intended to capture interactions between the rotor and shroud. Tests with the T-motor and NACA0012 rotor were performed in hover to investigate performance differences. In the wind tunnel, the T-motor rotor was the only rotor used. To prevent blade strike, the rotor tip to duct wall clearance is 0.275 inches; within 2% of the rotor radius.

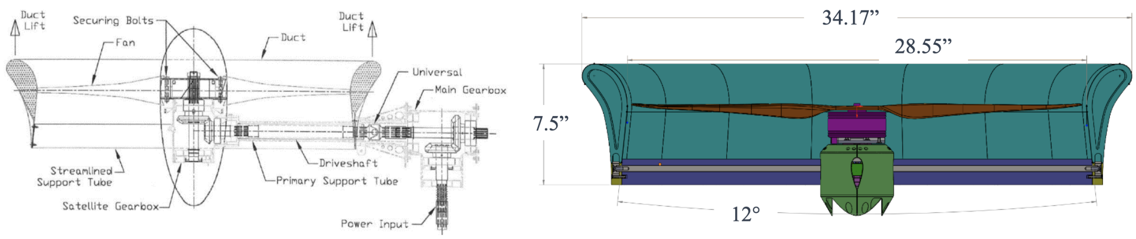

Figure 2.42: NASA shroud (left) and shroud design of this study (right).

The shroud structure is made from sheet metal, linear rails, and machined steel parts as shown in Figure 2.43. The shroud was fabricated in-house using 3D printing. The shroud outer geometry is made from 3D printed plastic parts using a HP Multi-jet fusion 3D printer and is secured together with keyed inserts and fasteners as shown in Figure 2.44. To simplify the fabrication process, the shroud was split into 16 sections and printed individually. Each of the 16 sections consists of three parts: ‘Duct Top’, ‘Duct Key’, and ‘Duct Bottom’. This was done to fit the steel frame inside the shroud and create a seamless outer mold line. The 3D printer material chosen was glass filled nylon PA12, giving the shroud a total weight of 17 lbs, of which 7 lbs is steel structural weight and 10 lbs 3D printed plastic sections, as shown in Figure 2.43.

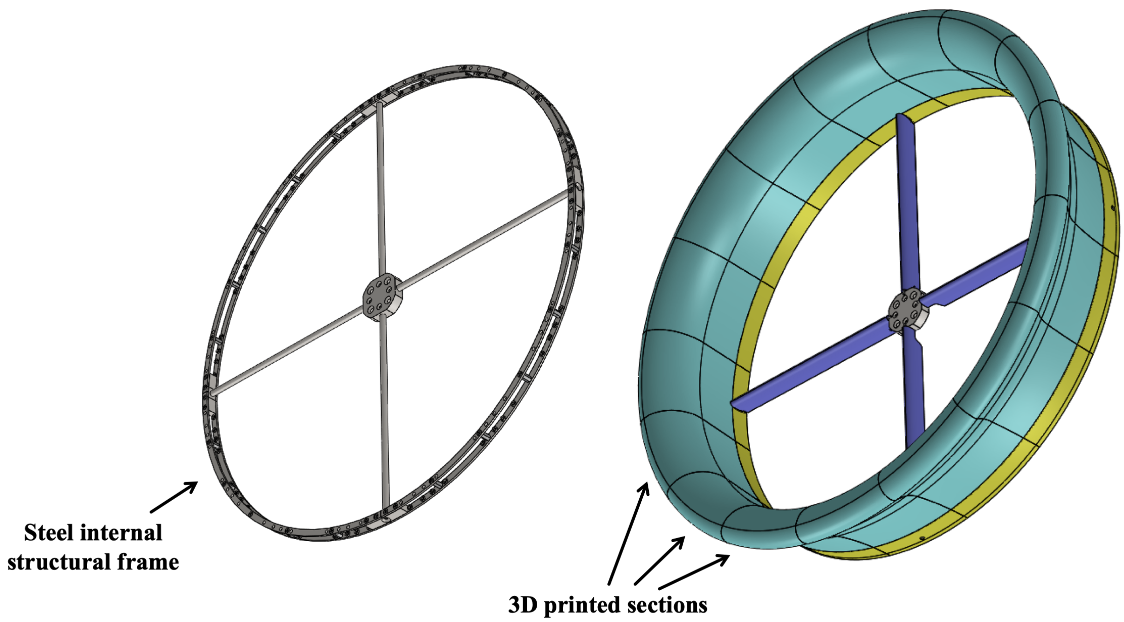

Figure 2.43: Internal steel structure (left) and fully assembled shroud (right).

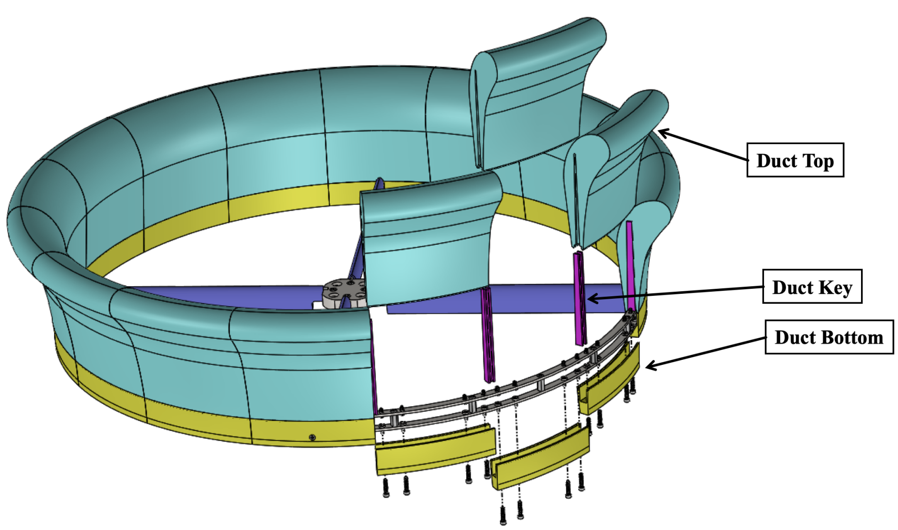

Figure 2.44: Shroud assembly with keys to join parts together.

The rotor and shroud loads are measured independently with two 6-DOF load cells. The structure to fasten the rotor and shroud load cell together is separated with a sufficient gap to avoid coupled measurements. The load cells are mounted in parallel to maximize the system stiffness. The sensing origin for the load cells is centered on the mounting plate surface of the load cell as shown in Figure 2.45. Thus, post processing of the raw data is required to calculate the true moment data based on the offset distance.

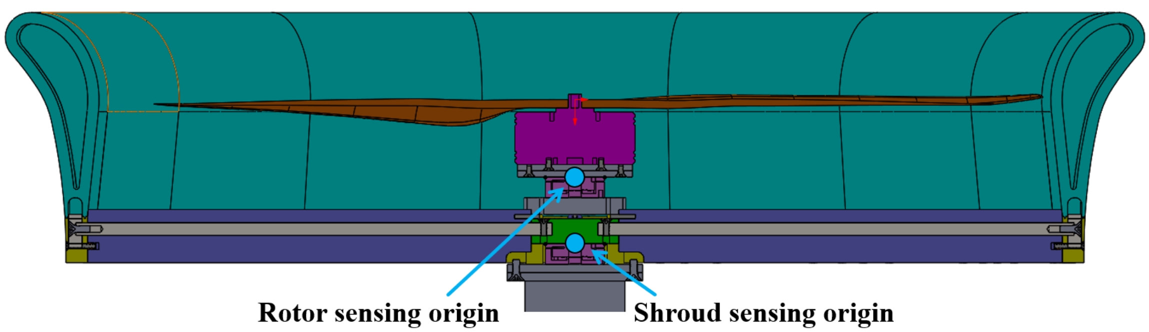

Figure 2.45: Cross section view of two 6-DOF load cells for rotor and shroud.

Structural Analysis

Finite element analysis (FEA) of the shroud was performed to determine the maximum deflection. With the geometry of the shroud, a drag side load is expected to cause the most strain on the duct. With this loading, the load cell's maximum moment reading is 20 Nm. Thus, a remote side load of 20 lbs with a moment arm of 9.0 inches was applied to the external side face of the shroud as shown in Figure 2.46.

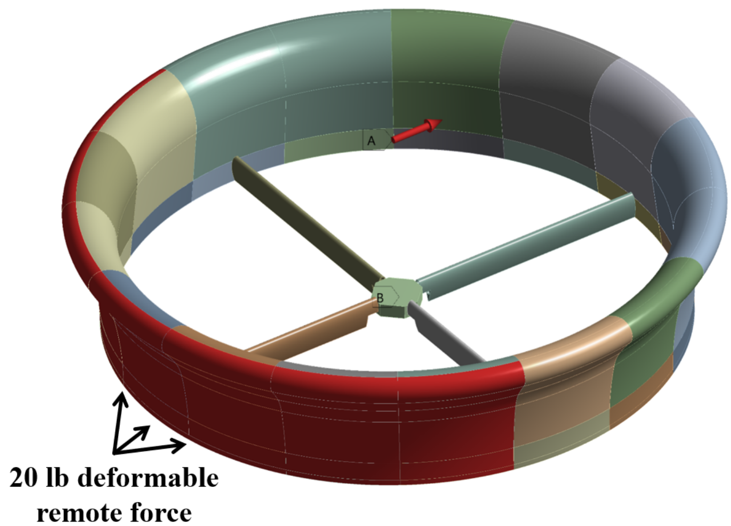

Figure 2.46: A 20 lb deformable remote force was applied to the section in red with an equivalent loading equal to the maximum moment measurement range of the load cell.

The final deflection result is shown in Figure 2.47. Located at the edge of the shroud, the maximum deflection is 0.089 inches in the upward Z direction. For all loading cases, there was nearly zero deflection in the direction of the rotor clearance.

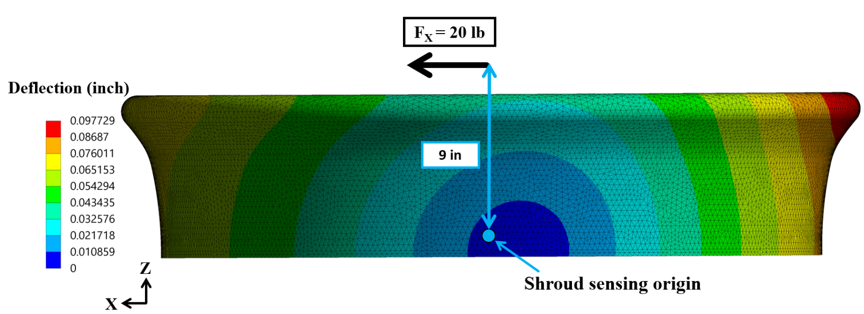

Figure 2.47: Deflection of the shroud under a maximum loading condition. The deflection is nearly zero in the direction of the rotor clearance.

Modal Study

With the design complete, a modal frequency test in SolidWorks was conducted to determine the resonant frequencies of the shroud both independently and with the stand. Figure 2.48 shows a modal study of the shroud with the mounting point fixed. The first mode was 13 Hz, second and third 14.3 Hz, and fourth 17.98 Hz. The second and third modes are symmetrical and therefore yielded identical resonant frequencies. Based on the test stand resonant frequency of 24 Hz, there is likely less than an octave of separation from the stand making coupling between the shroud and stand likely.

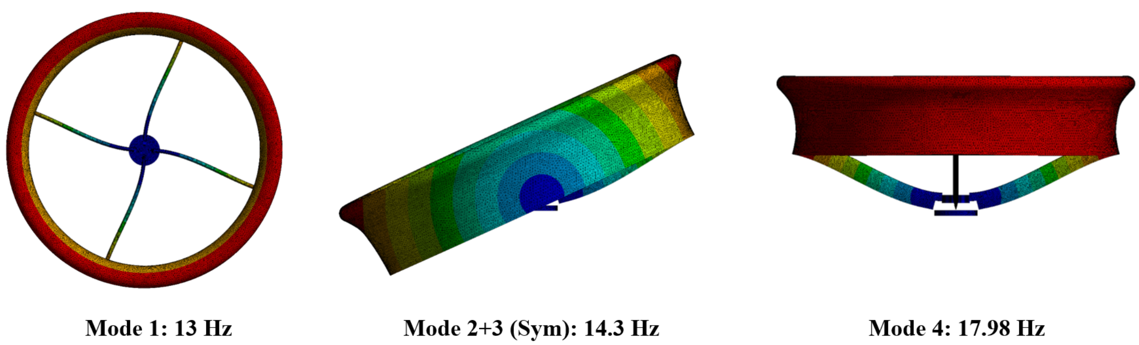

Figure 2.48: Modal study of independent shroud with mount fixed.

A second modal study was performed as shown in Figure 2.49 with the shroud to investigate the complete system. The first mode was found to be independent with movement from the shroud alone at 13 Hz (780 RPM 1/rev). The second and third modes are coupled movements of the stand and shroud together and have frequencies of approximately 15 Hz (900 RPM 1/rev). These frequencies were later used to determine test RPMs to prevent exciting the natural frequencies of the structure while collecting data.

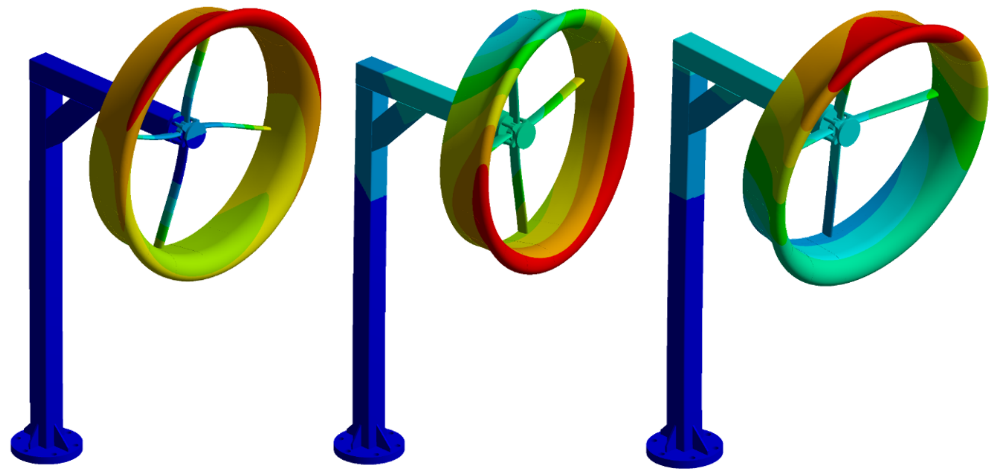

Figure 2.49: Shroud modal frequencies are below test RPMs (2300, 3100, 3900 RPM).

2.2.3 TRV-80 Bare Airframe

The TRV-80 bare airframe model required secure fastening in order to hold the model's 25 lb weight and withstand the predicted drag forces. In addition, it was important to place the load cell at the center of the airframe such that the six degree of freedom forces and moments measured would not require offset from the actual vehicle's origin.

Figure 2.50 shows the assembly procedure to mount the TRV-80 model to the test stand. The procedure is as follows: 1) An aluminum plate is secured to the aft side of the TRV-80 airframe with 3D printed inserts to morph the round carbon fiber tubes of the airframe to the flat surface of the aluminum plate. 2) Additional 3D printed inserts are secured to the opposite side. 3) A second aluminum plate sandwiches the pieces together using fasteners. 4) A third plate is mounted to provide the necessary offset which keeps the load cell centered at the origin of the airframe. The internal structure with the 3D printed inserts is shown in Figure 2.51. The final structure shown in Figure 2.54 shows the TRV-80 airframe mounted to the test stand on the hover tower. Once the model is mounted to the test stand, an aluminum cover is secured to the outer housing of the airframe to provide a continuous outer mold line geometry that resembles the vehicle with an installed battery.

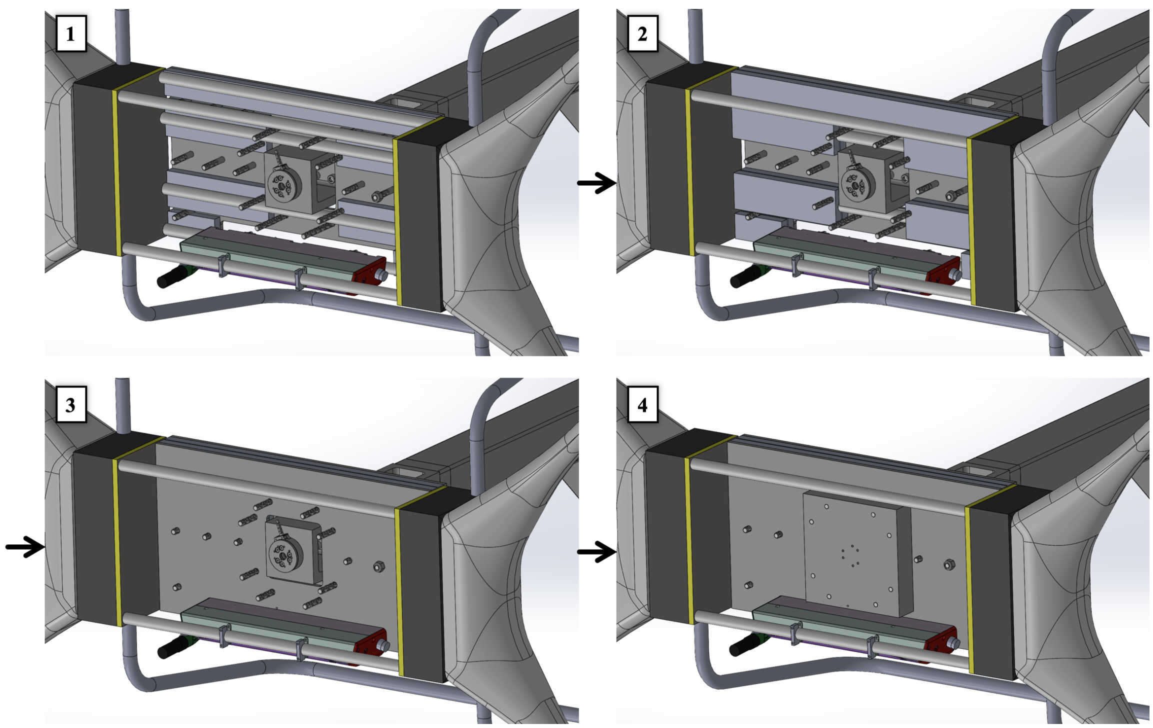

Figure 2.50: Assembly procedure of wind tunnel support structure fastened to the TRV-80 airframe carbon fiber structural rods.

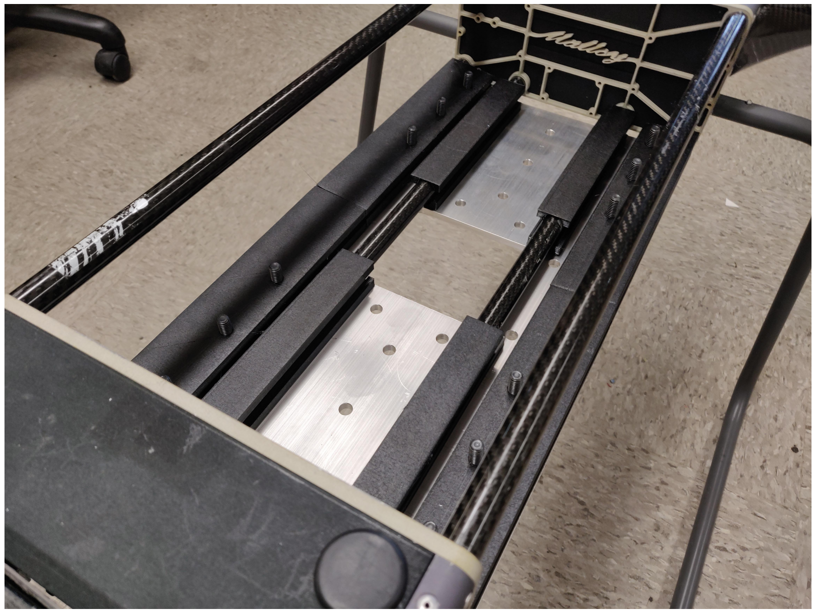

Figure 2.51: Internal structure of the TRV-80 airframe mounting assembly for test stand.

Figure 2.52: TRV-80 airframe mounted to test stand on hover tower.

2.3 Wind Tunnel Testing

2.3.1 Operating Procedure

Before collecting data, the load cells were tested to validate the calibration by hanging known weights in the F_Y, F_Z, and M_Z directions. The wind tunnel velocity readings from the dynamic-pressure measurements were cross-checked with a hot wire probe and a pitot-static tube installed in the empty test section. Measurements for the rotor were initially performed at -90° or a full climb orientation to avoid wall effects. These tests were conducted with climb inflow only, as the rotor alone would drive the closed loop tunnel to approximately 3-5 m/s depending on the rotor RPM, so purely static cases were not possible in the wind tunnel. As stated earlier, static hover tests were conducted outside of the wind tunnel on a hover tower to prevent recirculation.

In general, data for three rotational speeds were recorded: 2300, 3100, and 3900 RPM for an angle of attack sweep from -90° to 90°. These RPMs were chosen based on their advance ratio range (up to 0.25), tip Mach numbers (up to 0.4), and tip Reynolds numbers (up to 500,000).

2.3.2 Axis Convention

The testing rig shaft angle of attack α_s definition is shown in Figure 2.53. With the flow direction coordinate frame fixed and the stand able to rotate in a rotating frame, the α_s angles are as follows: In pure descent $\alpha_s = 90°$, in edgewise flight with the rotor plane parallel to the flow $\alpha_s = 0°$, and in pure axial climb $\alpha_s = -90°$. The direction of positive drag is $\alpha_s = 90°$ and is in the same direction as the flow and vice-a-versa for negative drag. Because the load cell rotates with the rotor, post processing is required to calculate the drag and lift of the rotor loads relative to the fixed frame flow direction.

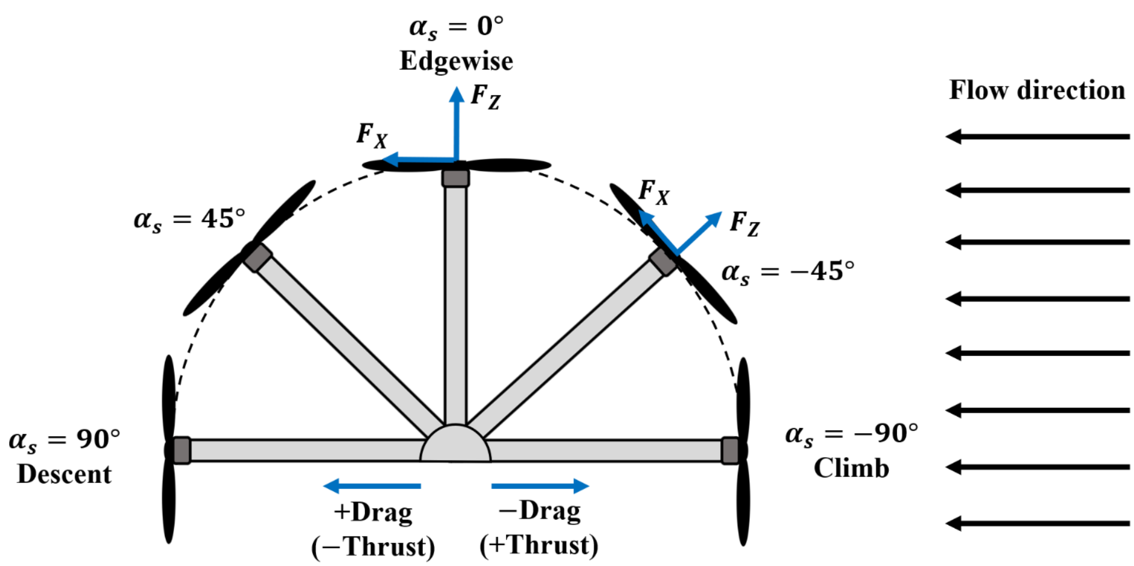

Figure 2.53: Angle of attack definition.

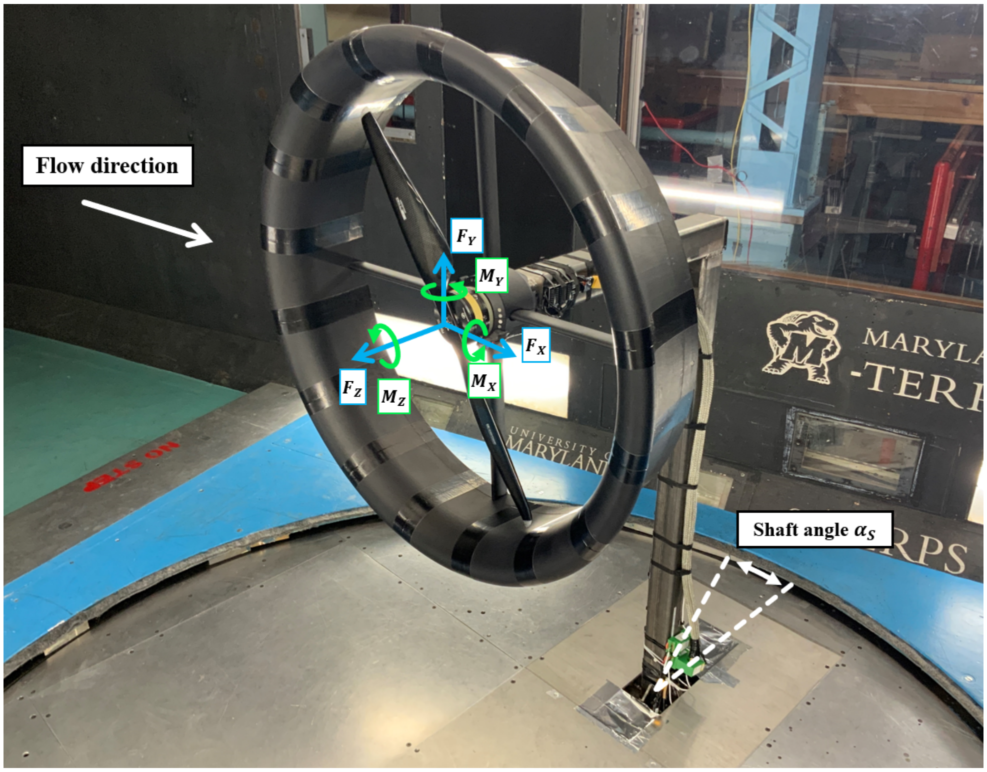

Figure 2.54: TRV-80 airframe mounted to test stand on hover tower.

2.3.3 Chosen Test RPMs

In general, three rotational speeds were recorded: 2300, 3100, and 3900 RPM. These were chosen based on the TRV-80 vehicle's notional gross take-off weight (GTOW), battery power output limits, and stand resonant frequencies. Due to the wide payload range of the vehicle, it is important to capture a set of RPMs that accounts for this change in hover thrust. In addition, these RPMs correlate to advance ratios up to 0.25, tip Mach numbers up to 0.4, and tip Reynolds numbers up to 500,000. Based on thrust and power experimental measurements for a single rotor, the hover GTOW and power estimates for a four and eight rotor configuration were calculated and is shown in Table 2.3. This was done to ensure the chosen test RPMs are realistic for a notional multi-rotor powered by a battery rather than an external power supply as is used in testing. The four rotor configuration shows a GTOW range of 29-86 lbs and total power 1000-5600 W for the chosen test RPMs. These are acceptable values for a quadrotor configuration powered by an installed battery. For the eight rotor configuration such as the TRV-80, the approximate GTOW for 2300 and 3100 RPM is 58 and 108 lbs with a total power requirement of 2000 and 5100 W. These are also acceptable values which cover the expected payload range of the TRV-80 [26].

Table 2.3: Four and eight rotor vehicle configuration estimated thrust and power values for chosen test RPMs.

RPM	2300	3100	3900
4 rotors:			
GTOW (lbs)	29	54	86
Total Power (W)	1000	2550	5600
8 rotors:			
GTOW (lbs)	58	108	172
Total Power (W)	2000	5100	11200

2.4 Transient Rotor Testing

In addition to quasi-steady tests, transient tests were conducted to derive and validate an isolated rotor model using system identification. Unlike the steady RPM tests, the transient RPM tests are intended to vary the RPM over time instead of keeping the RPM constant. The results from these tests can be used to develop a physics based model of a complete multi-rotor simulation. These tests were conducted both in static hover conditions as well as in the wind tunnel. Unlike the steady tests, it is important to measure at a faster log rate in order to capture unsteadiness with the system. Thus, all measurements were collected at 5 kHz. For the isolated rotor, the control input was the PWM signal sent to the ESC. Both step inputs and chirps were used to characterize the response of the ESC, motor and rotor system as a single unit. The output data of primary interest included the six DOF loads of both the motor and rotor and transient RPM reading that measures and calculates the RPM one time every rotation. The RPM was measured using two infrared reflective IR photoelectric switches. RPM is then calculated from the measured voltage and associated with time as defined by Equation 2.2. The result is a square wave that changes voltage from 5V to 0V depending on whether it measures the reflective tape on the motor. t_i is the time in which the voltage is above 2.5V and the next time step's voltage is below 2.5V. t_f is the next time that this occurs. In essence, this process measures the period in seconds which is then used to calculate RPM.

$$RPM = \frac{1}{t_f - t_i} * 60 \tag{2.2}$$

The PWM signal was sent to the ESC using a Teensy Arduino. The PWM commands were stored on the Arduino and an operator switch was used to manually begin the sequence.

It is important to ensure the data collected into the DAQ is in sync with the commanded PWM signal from the Arduino. To guarantee this, the Arduino is connected to the DAQ with an analog wire that changes from 0V to 2.5V when the PWM sequence is triggered to begin. Thus, when the first PWM signal in the sequence is sent, the Arduino switches its analog output signal to 2.5V to indicate the sequence has begun. An example of this voltage change is shown in Figure 2.55. These commands are located within the same code loop to ensure they occur at the same time. This 2.5V signal is received by the same DAQ that is used to measure all the data. This is done to ensure that when the prescribed PWM signal is sent, the timestamp of the voltages from the various sensors will be in sync with the PWM signal. Finally, in post processing, the data prior to the 0 to 2.5V switch is omitted and the data after the switch occurs is used for analysis. In summary, the PWM signal is an output whereas the sensor data is an input. Therefore, the PWM output signal requires an input to be sent to the DAQ to ensure it is in sync with the various DAQ input sensors to ensure that the commanded output PWM signal corresponds to the same time stamp as the input signals.

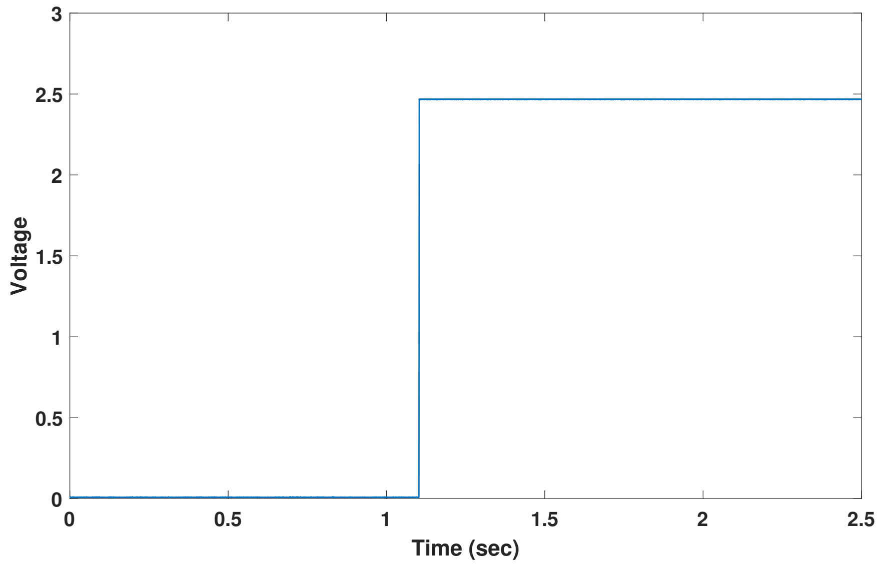

Figure 2.55: Trigger voltage to indicate the start time of the PWM input signal.

Chapter 3: Isolated Rotor Performance in Hover

3.1 Introduction to BEMT modeling

Blade element momentum theory (BEMT) is used to predict distributed blade loads. It accounts for the complex geometrical features of the T-motor and custom NACA0012 rotor which includes varying sectional chord length, twist, and airfoil geometry described in section 2.2.1. Airfoil tables were produced using in-house HAM2D computational fluid dynamics (CFD) and were input into the in-house BEMT code [27]. The results generated from BEMT provide insight into the magnitude and source of differences between experimental and predicted data.

BEMT works by calculating non-uniform inflow along the blade using 2D airfoil cross-sections by applying basic principles from both blade element and momentum theory. In effect, the angle of attack across the span of the blade changes. 3D aerodynamic effects are ignored to simplify the numerical calculation and appropriate corrections are applied to maintain accuracy.

With the complex geometry of the rotors, this approach is capable of capturing effects of twist, chord and airfoil profile variation at multiple sections along the span. In addition, it accounts for tip loss and appropriate Reynolds number correction based on the discretized section's Reynolds number. These advantages in accuracy and fast run time provide fast insight into rotor performance characteristics.

3.1.1 BEMT Inflow

Calculating non-uniform inflow λ without making assumptions on its magnitude or form is a key feature in predicting rotor performance with BEMT. This is carried out by calculating incremental thrust dC_T along the span r using both momentum (MT) and blade element theory (BET) as shown in Equation 3.1. For the static hover conditions tested, $\lambda_c = 0$.

$$dC_T = 4r\lambda(\lambda - \lambda_c)dr \tag{3.1}$$

A trailed vortex is formed at the tip of the blade which produces a high local inflow resulting in loss of lift. This tip loss is described by Equation 3.2

$$F = \frac{2}{\pi}cos^{-1}(e^{\frac{N_b}{2}(\frac{1-r}{r\phi})}) \tag{3.2}$$

Here, $N_b = 2$ and $r = 0.2$ to 1 due to the root cutout. Combining equations 3.1 and 3.2 we have a function for dC_T that includes the Prandtl tip loss as shown in Equation 3.3.

$$dC_T = 4Fr\lambda^2 dr \tag{3.3}$$

From here, the resulting sectional lift and drag coefficients can be found based on the inflow λ to determine coefficient of thrust C_T and coefficient of power C_P. The airfoil cross section air flow components are shown in Figure 3.1.

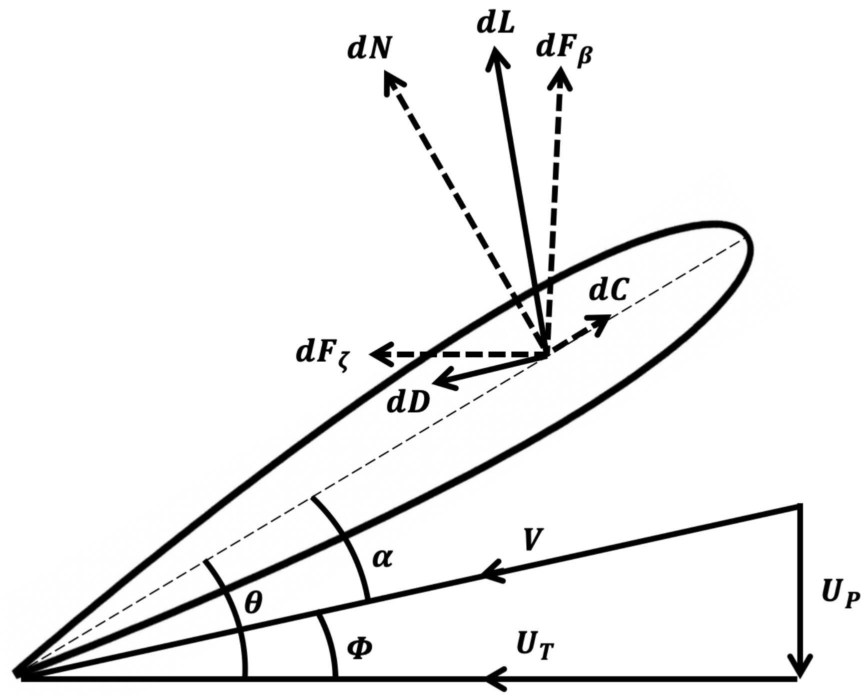

Figure 3.1: Blade element forces in hover.

The incremental thrust coefficient is expressed using the standard BET equation to find non-uniform inflow as shown in Equation 3.4.

$$dC_T = \frac{\sigma C_{l_\alpha}}{2}(\theta - \frac{\lambda}{r})r^2 dr \tag{3.4}$$

In a numerical approach, the inflow of the blade is found using the discretized equation shown in Equation 3.5. Iteration is required because an algebraic solution does not exist due to the tip loss component F which is itself a function of λ.

$$\lambda = \frac{\sigma C_{l_\alpha}}{16F}\left(\sqrt{1+\frac{32F}{\sigma C_{l_\alpha}}\theta r}-1\right) \tag{3.5}$$

For all inflow calculations, a relaxation of $f = 0.01$ is used. In addition, elastic effects are ignored for blade flap (out of plane bending), blade twist due to torsion, and blade lead-lag motion as the rotor was found to have high stiffness in all directions. Trailing edge vortex interaction is also ignored in these hover performance predictions.

3.2 Aerodynamic Correction

Flow compressibility can affect the aerodynamic performance for rotors when operating at high tip speeds. The equation for Mach number along the span of the blade is described in Equation 3.6 where $\frac{r}{R}$ is the radial station and a_s is the speed of sound.

$$M = \frac{\frac{r}{R}\Omega R}{a_s} = xM_T \tag{3.6}$$

The plot shown in Figure 3.2 shows the mach number trend along the span of the blade for 3000 RPM. For the majority of the blade, the mach number is below 0.3, and thus, compressibility effects are neglected to simplify the solution process as they would have minimal effect.

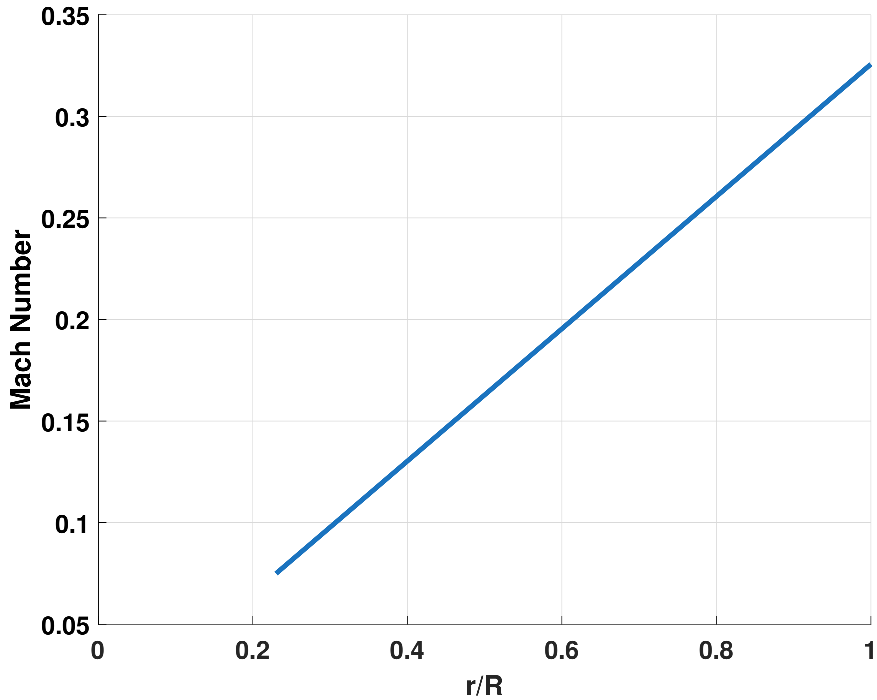

Figure 3.2: Mach number vs radial station for the R=14 inch rotor.

For these small scale rotors, the Reynolds number variation along the span can significantly affect the performance of the rotor. With a constant chord, the NACA0012 blade Reynolds number varies linearly from Re = 50,000 to 500,000. The T-motor rotor has varying chord length so Reynolds number varies with chord length distribution. The approximate Reynolds number variations are shown in Figures 3.3 and 3.4.

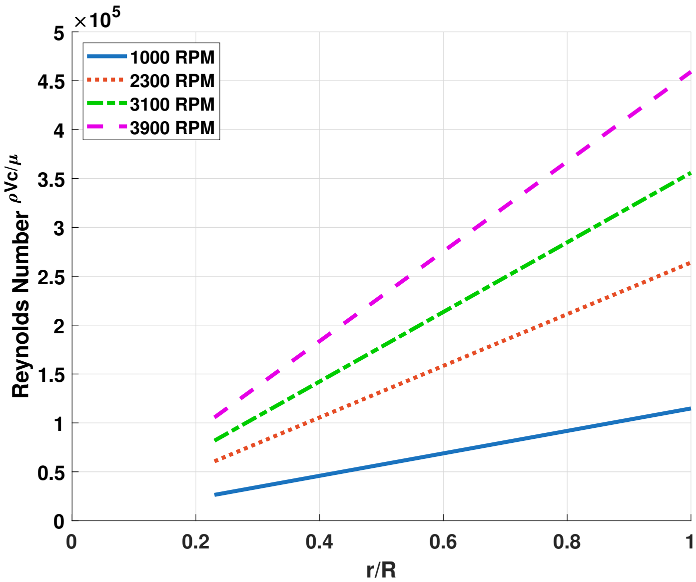

Figure 3.3: Reynolds number vs radial station for NACA0012 rotor.

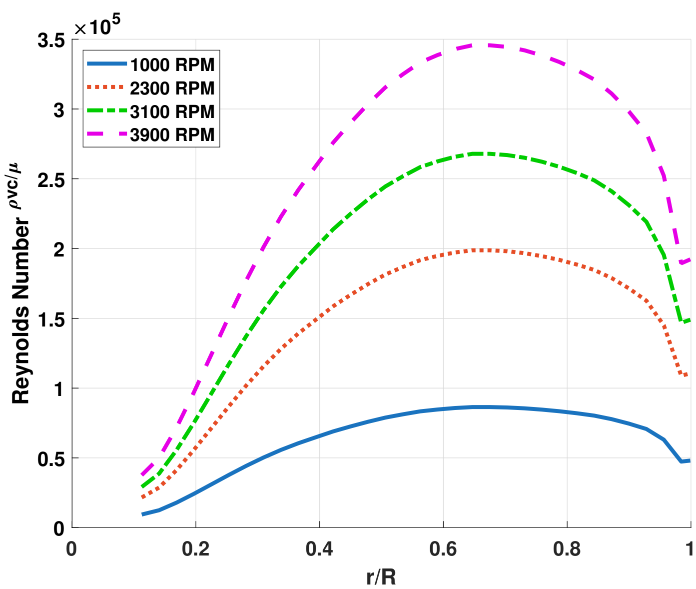

Figure 3.4: Reynolds number vs radial station for the T-motor rotor.

Due to the low Reynolds number operating regime of the $R = 14$ inch rotor and variation along the span, two forms of Reynolds number correction were applied to calculate the resulting non-dimensional thrust C_T and power C_P with RPM. The first form is an empirical approach which uses a single lift C_l and drag C_d airfoil table generated at one Reynolds number as described by Yamauchi and Johnson [28]. The second approach is an interpolation method using multiple airfoil tables generated at different Reynolds numbers and interpolating among them.

Reynolds number is defined by equation 3.7 where U is the tangential velocity and c is the chord length of the airfoil cross section. The atmospheric conditions are defined by air density ρ and viscosity μ_v. Thus, for the same atmospheric conditions, two factors that affect the operating Reynolds numbers are rotational speed and chord length. Pitch angle is a third factor which is included to account for change in angle of attack as it affects airfoil velocity along the chord.

$$Re = \frac{\rho U c}{\mu_v} \tag{3.7}$$

3.2.1 Reynolds Number Empirical Method

The empirical approach applies an easily implemented method to account for the Reynolds number effects. This method was originally validated for Reynolds numbers above 1,000,000.

First, the incremental Reynolds number Re is calculated based on the radial position. Next, a value K is calculated as described by equation 3.8 where Re_t is the airfoil table's characteristic Reynolds number. The value K is used to correct the single set of airfoil tables generated at a single Reynolds number Re_t to match the true Reynolds number Re of the specific radial station location. In this case, $Re_t = 200,000$ was used to generate airfoil table in CFD and a constant $n = \frac{1}{8}$ was used.

$$K = \left(\frac{Re}{Re_t}\right)^n \tag{3.8}$$

The corrected lift coefficient C_l is next found based on the corrected value $\frac{\alpha}{K}$ which is then multiplied by the factor K as shown in equation 3.9. For non-symmetrical airfoils, a factor C_{l_o} is also accounted for as shown.

$$C_l = K\left(C_{lt}\left(\frac{\alpha}{K}\right) - C_{l_o}\right) + C_{l_o} \tag{3.9}$$

The corrected drag coefficient C_d is found based on α and divided by the factor K as shown in equation 3.10.

$$C_d = \frac{C_{dt}}{K} \tag{3.10}$$

With these corrected values for C_l and C_d, BEMT follows the same procedure in determining C_T and C_P.

3.2.2 Reynolds Number Interpolation Method

Instead of generating airfoil table data at a single Reynolds number and applying correction, values for C_l and C_d are generated at multiple Reynolds numbers and it is linearly interpolated based on the radial station's Reynolds number. Based on the Reynolds number range shown in Figures 3.3 and 3.4, CFD data was generated at Re $=$ 50,000, 100,000, 200,000, and 500,000.

With these interpolated values for C_l and C_d, BEMT follows the traditional procedure in determining C_T and C_P.

3.3 2D Airfoil CFD

HAM2D Computational Fluid Dynamics (CFD) code was used to create the airfoil tables for its functionality in generating meshes from 3D scanned blades and low Reynolds number accuracy [27]. Tables were generated by the Army Research Laboratory (Aberdeen). The angle of attack α varied across a range of values with greater precision between -10 and 15 degrees. Due to variation in airfoil geometry along the span of the T-motor blade, multiple airfoil cross sections were used to generate airfoil tables which were then interpolated in BEMT. Meshing was performed using an O-grid approach using coordinates from a 3D scanned airfoil cross section and fully turbulent flow approximation.

For the T-motor rotor, the cross sectional airfoils used were located at a radial station of 31%, 82%, and 98% as shown in Figure 3.5. These were chosen as the geometry at these locations was different from one another and would therefore yield well separated airfoil table results. Using the data from these airfoils, the intermediate locations were linearly interpolated based on their position to determine the C_l and C_d coefficients.

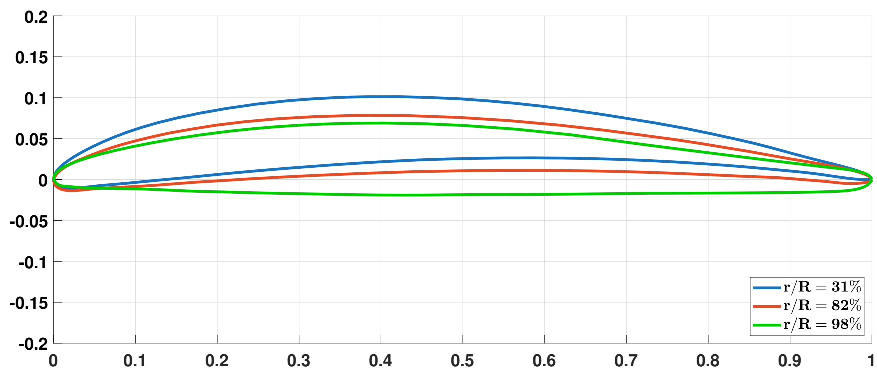

Figure 3.5: T-motor rotor airfoil cross sections.

The C_l and C_d trend with varying angles of attack α of both the NACA0012 and T-motor rotors were generated and results are shown in Figures 3.6, 3.7, 3.8, and 3.9.

Figure 3.6 shows the C_l versus α trends for the rotor blade cross sections based on the Reynolds number to compare variation among the airfoils. At lower Reynolds numbers, such as Re = 50,000 and 100,000, the airfoil cross sections along the span of the T-motor blade have similar slopes with a similar C_{l_o}. However, the $\frac{r}{R} = 31\%$ airfoil stalls around $\alpha = 6°$ while the $\frac{r}{R} = 81\%$ and 98% airfoils stall later around $\alpha = 9°$. The NACA0012 airfoil has similar slope compared to the T-motor airfoils, but lower magnitude as it is a symmetrical non-cambered airfoil unlike the T-motor blade. At greater Reynolds numbers, such as Re = 200,000 and 500,000, there is greater discrepancy among the T-motor airfoils. Again, they have similar slopes but have greater C_{l_o} offset. Again, the NACA0012 airfoil has similar slope with $C_{l_o} = 0$.

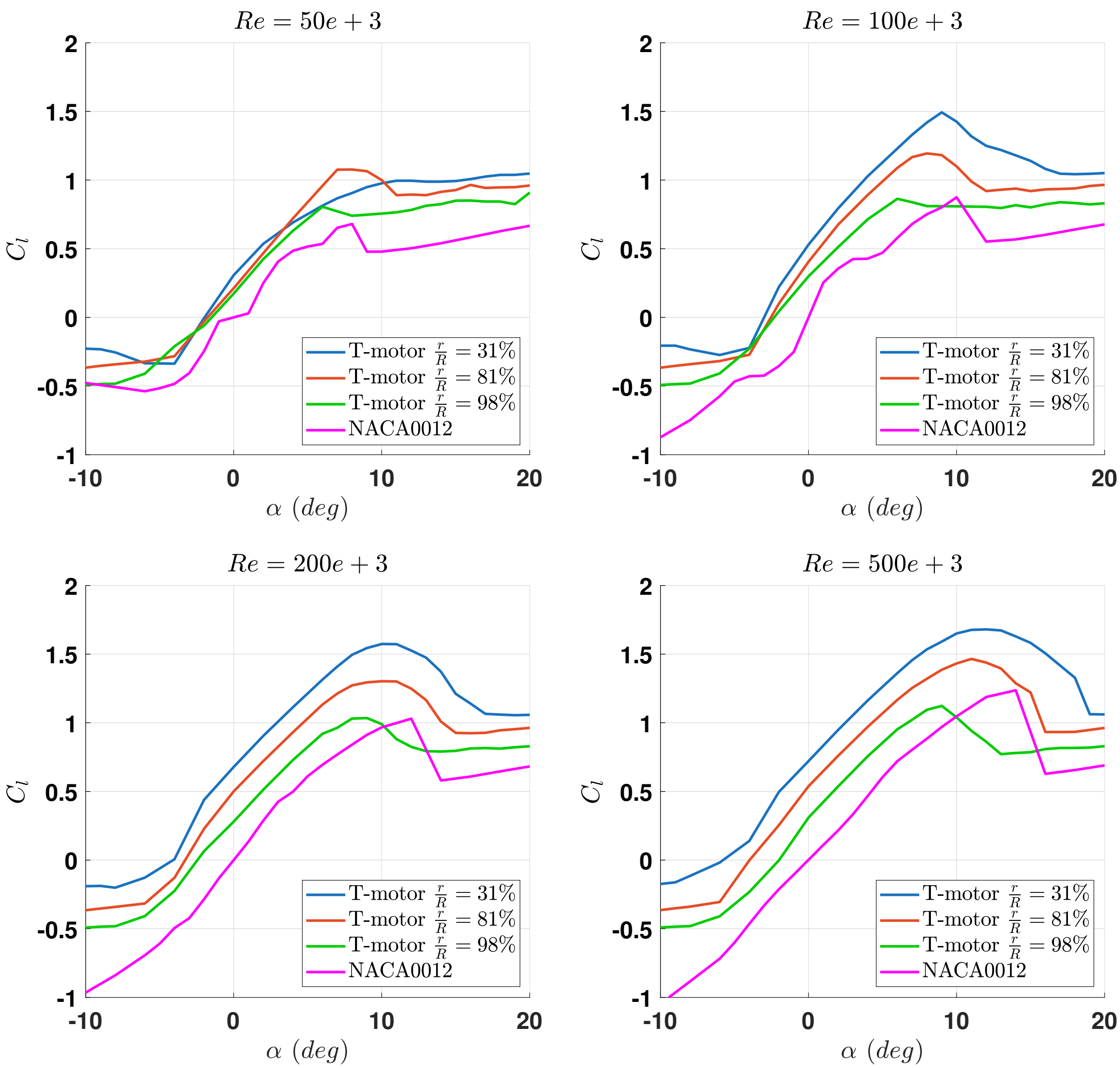

Figure 3.6: Four different Reynolds number plots of C_l versus α for T-motor and NACA0012 airfoils.

Figure 3.7 shows C_d trends for Reynolds number of 50,000, 100,000, 200,000, and 500,000. The difference between the T-motor airfoils located at $\frac{r}{R} = 81\%$ and 98% is minimal, with the NACA0012 airfoil following similar trends to the T-motor airfoils. However, the $\frac{r}{R} = 31\%$ airfoil experiences slightly greater drag compared to the other airfoils at the lowest value tested of Re = 50,000.

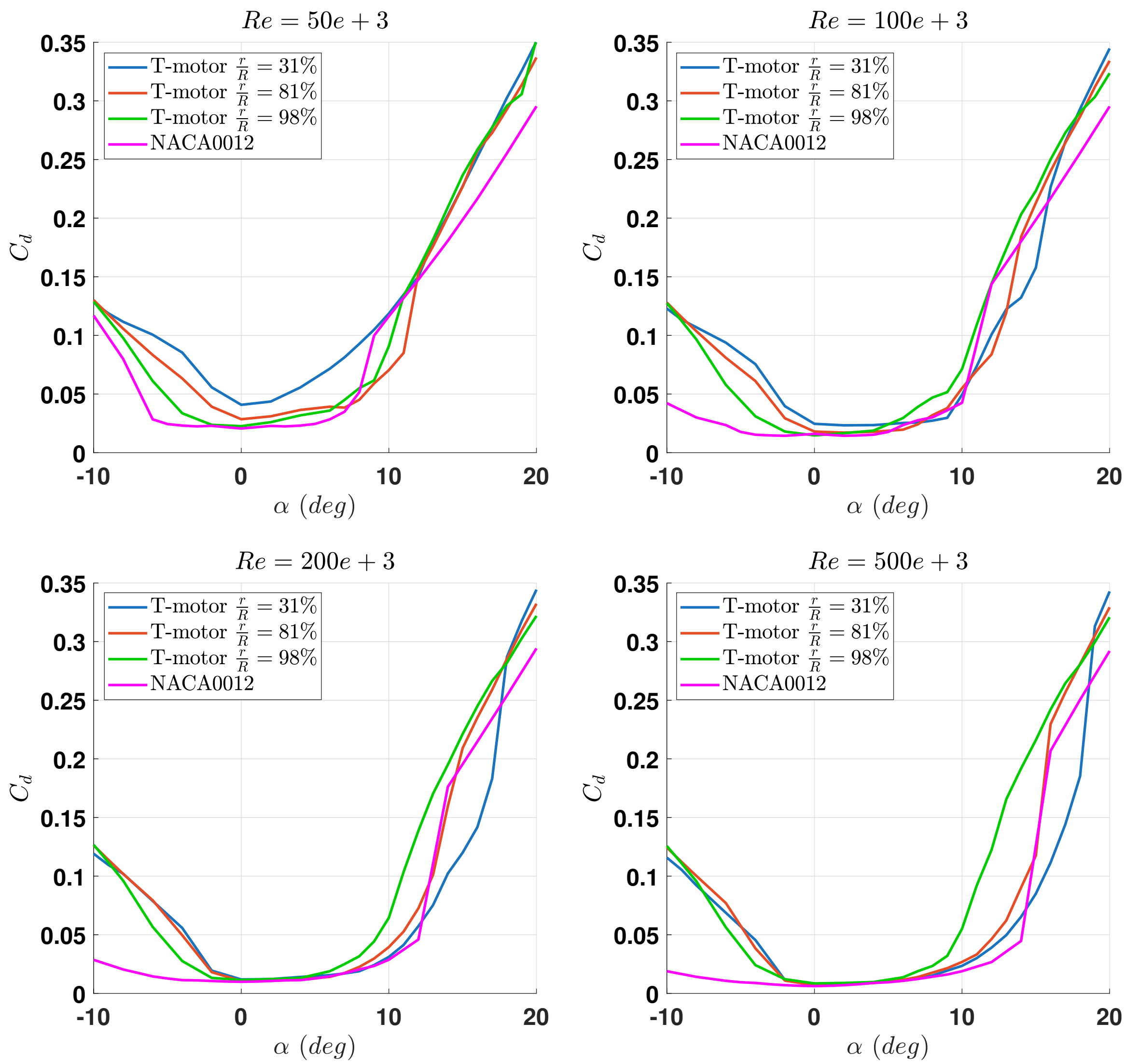

Figure 3.7: Four different Reynolds number plots of C_d versus α for T-motor and NACA0012 airfoils.

Figure 3.8 shows the C_l versus α trends for the T-motor and NACA0012 rotor based on the radial position to compare Reynolds number variation for a single airfoil. The slope of the airfoils with respect to Reynolds number variation is similar. However, C_{l_o} decreases with decreasing Reynolds number. Similarly, stall occurs earlier with reduced Reynolds number. For the NACA0012 airfoil, experimental wind tunnel data was included at Re = 54,400 [29]. This data matches well with the closest HAM2D CFD result at Re = 50,000 although the airfoil stalls at a slightly greater α angle compared to the CFD data. Overall, this data follows similar trends as described by Winslow et al. who studied low Reynolds number airfoils using TURNS2D, a similar CFD solver [30].

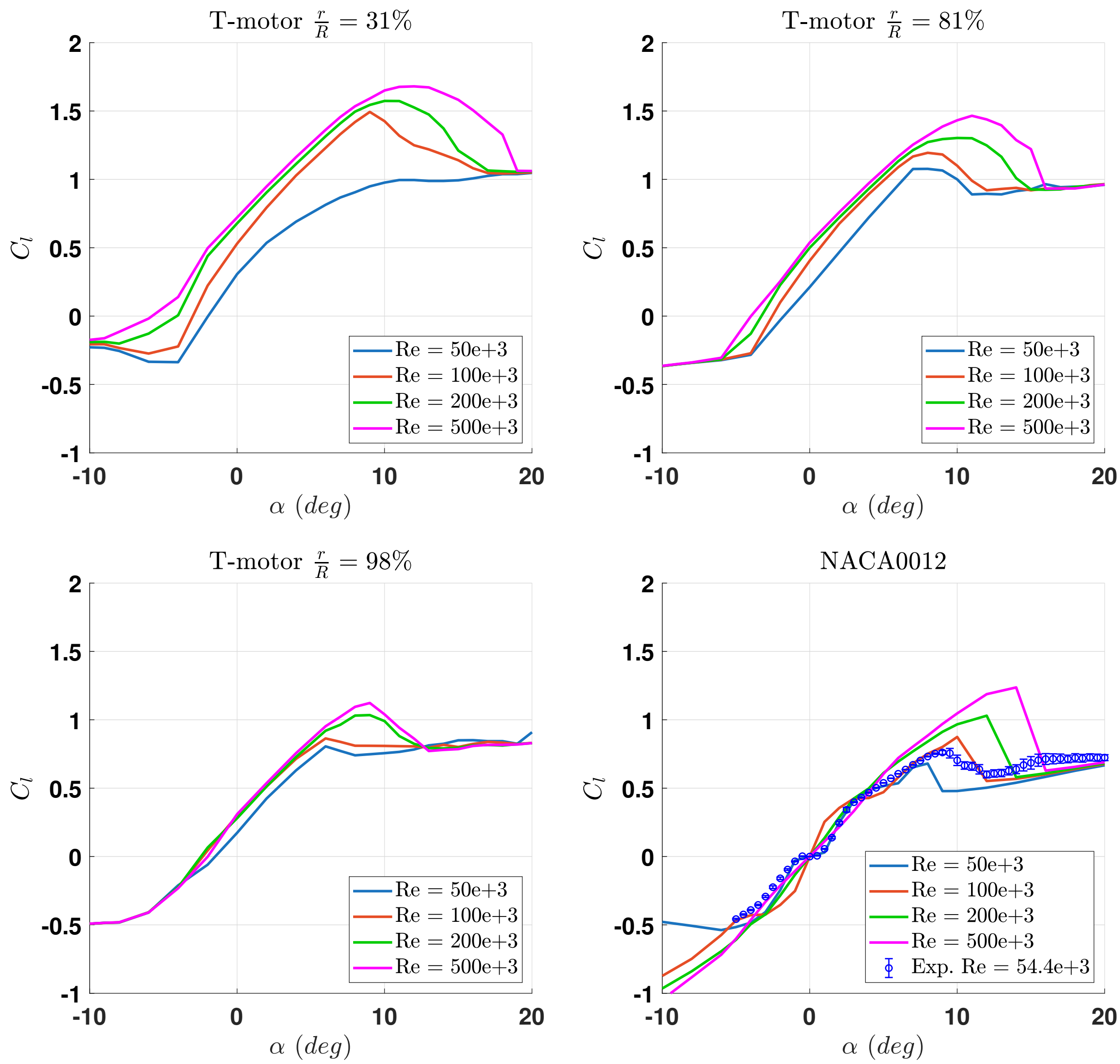

Figure 3.8: T-motor and NACA0012 airfoil plots of C_l versus α at four different Reynolds numbers.

Figure 3.9 shows the C_d versus α trends for the T-motor and NACA0012 rotor based on the radial position to compare Reynolds number variation for a single airfoil. The trend of the airfoils with respect to Reynolds number variation is similar. However, for all airfoils, there is greater drag at lower Reynolds numbers. This increase in drag increases as Reynolds number is decreased, thereby indicating the importance of capturing low Reynolds number effects for rotors operating below Re = 1,000,000.

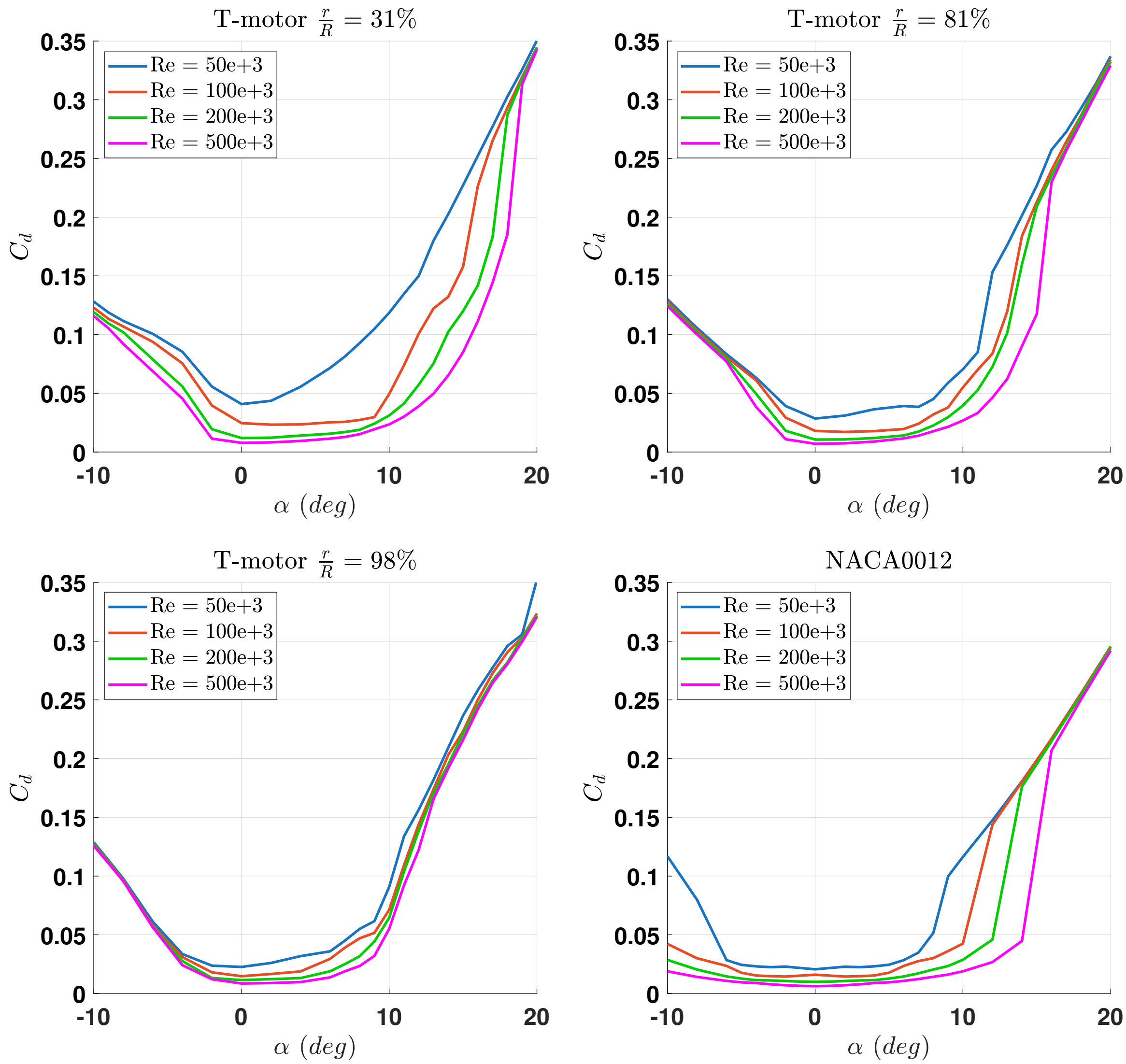

Figure 3.9: T-motor and NACA0012 airfoil plots of C_d versus α at four different Reynolds numbers.

3.4 BEMT Solution Process

An example set of NACA0012 and T-motor BEMT solution plots are shown in Figures 3.10-3.15 and 3.16-3.21, respectively. For these two cases, the rotational speed is fixed at 2000 RPM. For the NACA0012 blade, θ_{75} is fixed at 9°. For all plots, the Reynolds number empirical correction method is compared with the Reynolds number interpolation method discussed in Section 3.2.

Inflow distribution for the T-motor blade is shown in Figure 3.10. Near the root at $r/R < 0.5$, the interpolation method shows the most discrepancy compared to the empirical correction method. This can be attributed due to the low Reynolds number regime near the root at 2000 RPM. For $r/R > 0.5$, the interpolation method matches the empirical method better.

Figure 3.12 shows the coefficient of lift versus radial station. For $r/R < 0.5$, the blade is approaching the stall region in the interpolation results. Drag also increases at a greater rate as r/R approaches the root. These trends are a direct result of the C_l and C_d tables discussed in Section 3.3. As discussed earlier, with reduced Reynolds number, the airfoils stall at lower α angles and produce greater drag with reduced lift. In effect, the interpolation method trends for dC_T and dC_P shown in Figures 3.14 and 3.15 show greater differences at low RPMs compared to the empirical correction data.

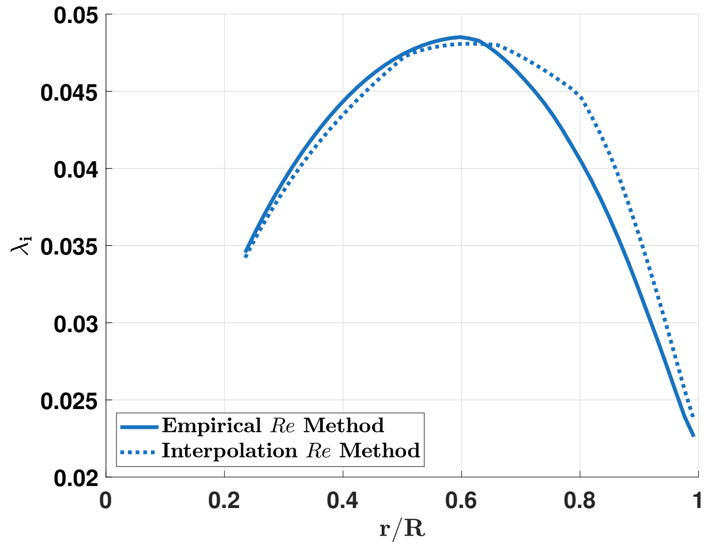

Figure 3.10: Inflow λ_i distribution over the span of the NACA0012 blade for $\theta_{75} = 5°$ and at 1000 RPM.

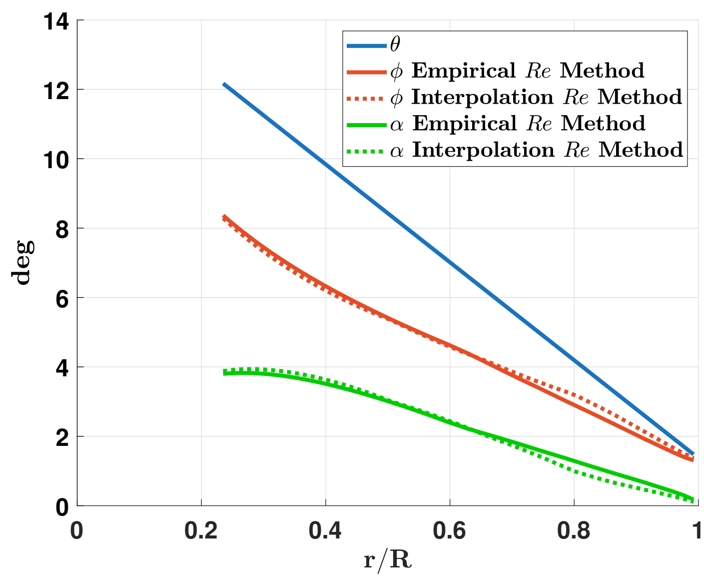

Figure 3.11: Blade pitch θ, inflow angle ϕ, and angle of attack α distribution over the span of the NACA0012 blade for $\theta_{75} = 5°$ and at 1000 RPM.

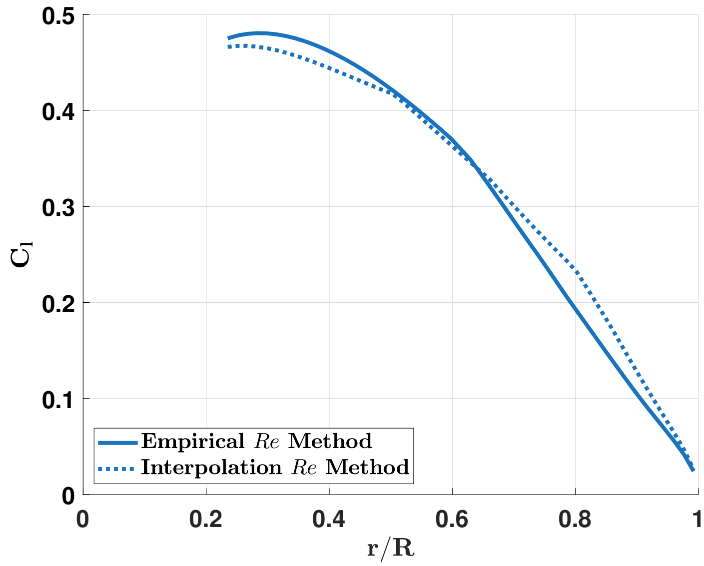

Figure 3.12: Coefficient of lift C_l distribution over the span of the NACA0012 blade for $\theta_{75} = 5°$ and at 1000 RPM.

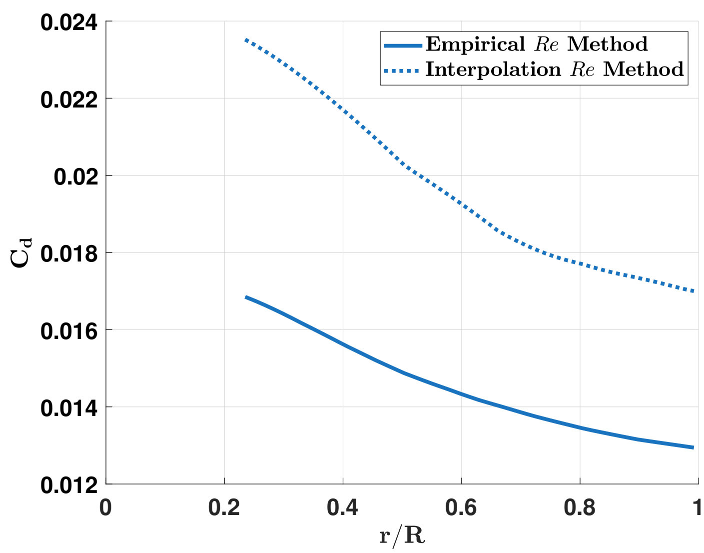

Figure 3.13: Coefficient of drag C_d distribution over the span of the NACA0012 blade for $\theta_{75} = 5°$ and at 1000 RPM.

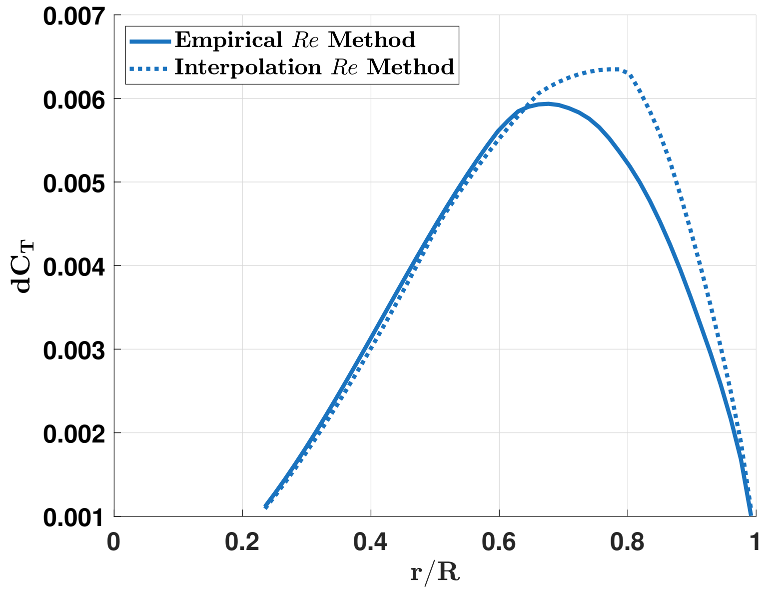

Figure 3.14: Coefficient of thrust dC_T distribution over the span of the NACA0012 blade for $\theta_{75} = 5°$ and at 1000 RPM.

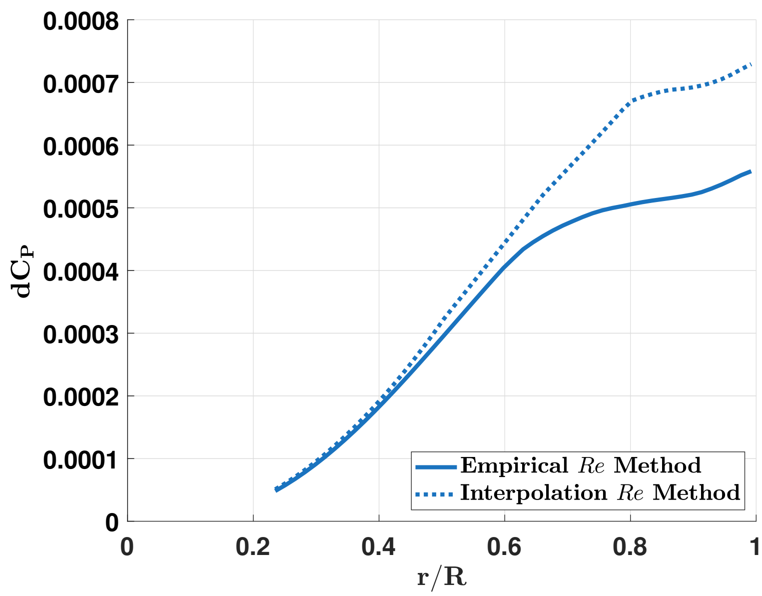

Figure 3.15: Coefficient of power dC_P distribution over the span of the NACA0012 blade for $\theta_{75} = 5°$ and at 1000 RPM.

Figures 3.16-3.21 show the BEMT results of the T-motor blade. Inflow distribution is shown in Figure 3.16. Along the total span of the blade, the interpolation method predicts lower induced inflow compared to the empirical method.

Figure 3.18 shows the coefficient of lift versus radial station. Similar to the NACA0012 blade, lift is reduced along the span. Drag also increases at a greater rate as r/R reduces towards the root.

The results for the T-motor blade and NACA0012 blade follow similar trends due to the same low Reynolds number effects. Overall, these calculations show that accurate BEMT results are dependent on accurate CFD data which can capture the low Reynolds number effects.

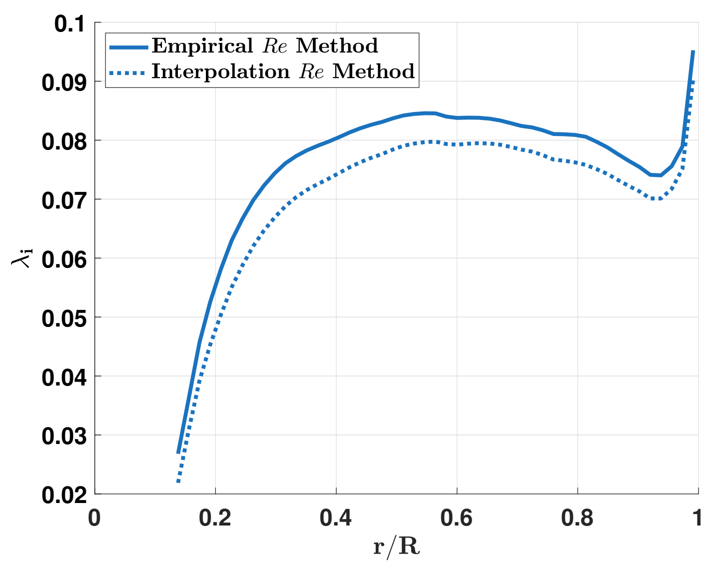

Figure 3.16: Inflow λ distribution over the span of the T-motor blade at 1000 RPM.

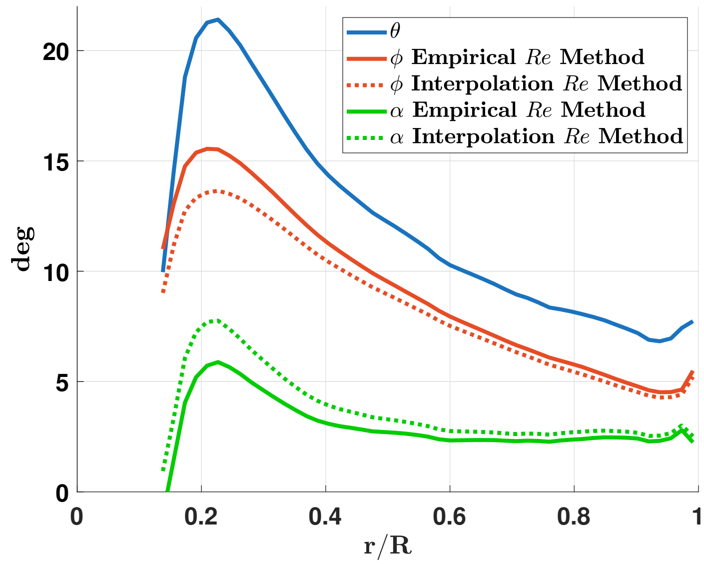

Figure 3.17: Blade pitch θ, inflow angle ϕ, and angle of attack α distribution over the span of the T-motor blade at 1000 RPM.

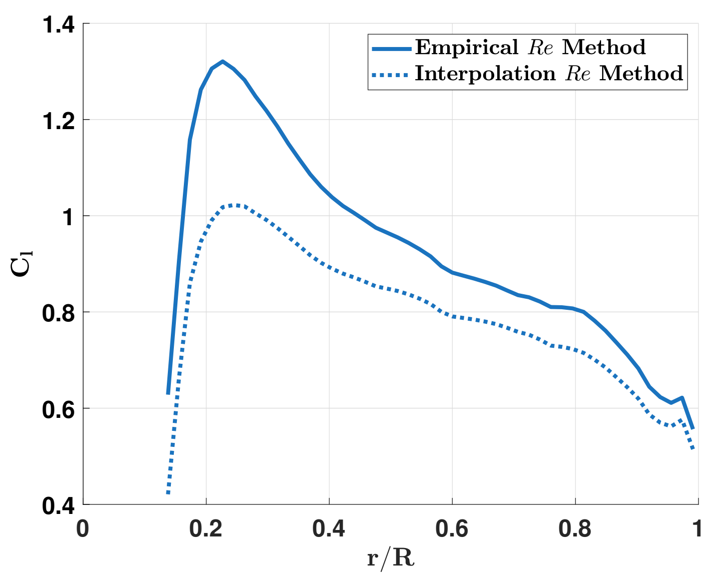

Figure 3.18: Coefficient of lift C_l distribution over the span of the T-motor blade at 1000 RPM.

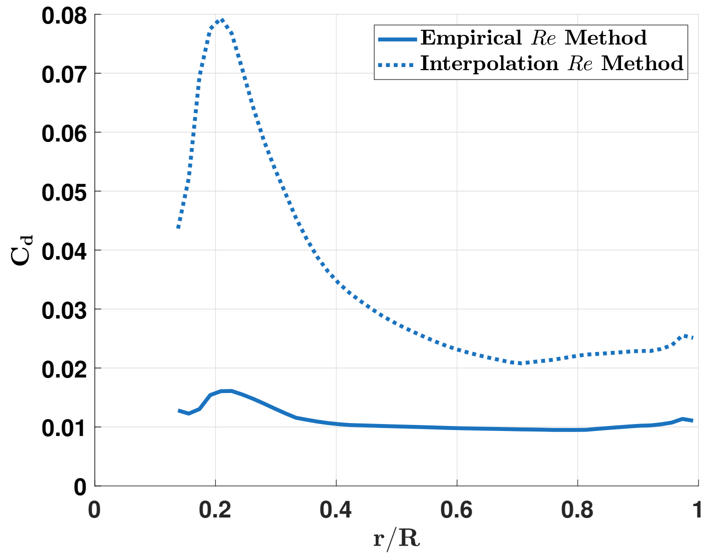

Figure 3.19: Coefficient of drag C_d distribution over the span of the T-motor blade at 1000 RPM.

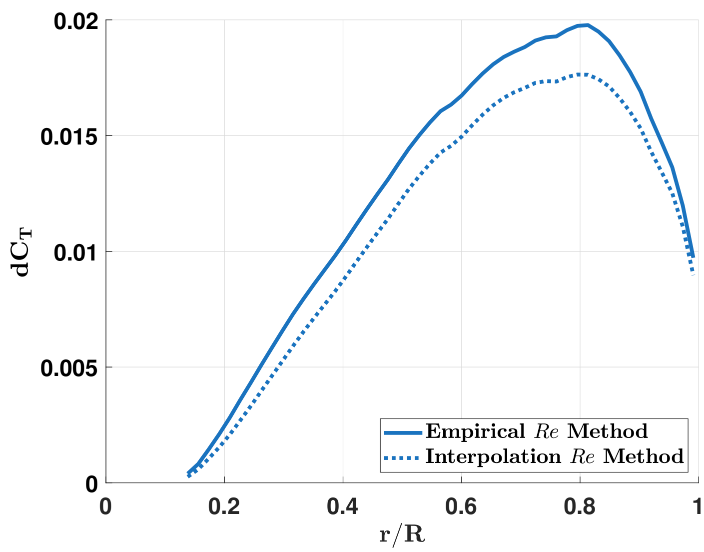

Figure 3.20: Coefficient of thrust dC_T distribution over the span of the T-motor at 1000 RPM.

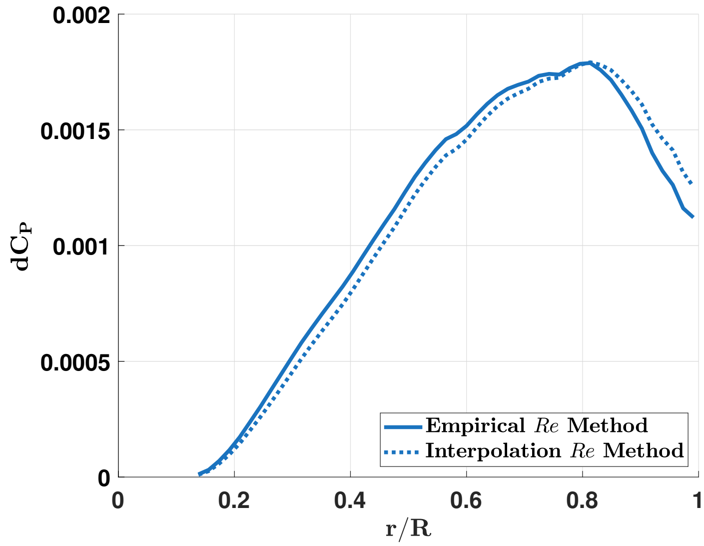

Figure 3.21: Coefficient of power dC_P distribution over the span of the T-motor blade at 1000 RPM.

3.5 Hover Experimental Data and Analysis Comparison

The T-motor and NACA0012 blades were tested on the experimental apparatus mounted on the hover tower and compared with BEMT results. The T-motor rotor was tested up to 4000 RPM at a single fixed collective as manufactured. The NACA0012 rotor was tested up to 3000 RPM for $\theta_{75} = 5°$, $8°$, $11°$, and $14°$. Minimal deflection was observed as both of these rotors have high bending and torsional stiffness.

3.5.1 Reynolds Number Empirical Correction Method

Figures 3.22 and 3.23 shows non-dimensional thrust and power normalized by solidity with BEMT results using the empirical correction approach described in Section 3.2.1 with airfoil tables generated at Re = 200,000. The T-motor rotor is plotted with the NACA0012 at varying collectives for comparison. The experimental data shows repeated data to represent the approximate spread in the measured values. At lower RPMs, the thrust and torque measurements are smaller and therefore more sensitive to measurement error. Thus, there is greater spread in the data at lower RPMs.

For C_T/σ, there is increasing slope with RPM for nearly all cases. For the NACA0012 rotor, this positive slope increases with increasing collective. In this case, the BEMT results were generated using the empirical correction method. The predictions correlate well for high RPM but show less correlation for lower RPM. Because the prediction matches better with greater RPM, the empirical correction approach is better suited for higher Reynolds numbers. For C_T/σ, this error varies between 5% and 30% between the predicted and experimental results. For C_P/σ, the error varies between 0% and 15%.

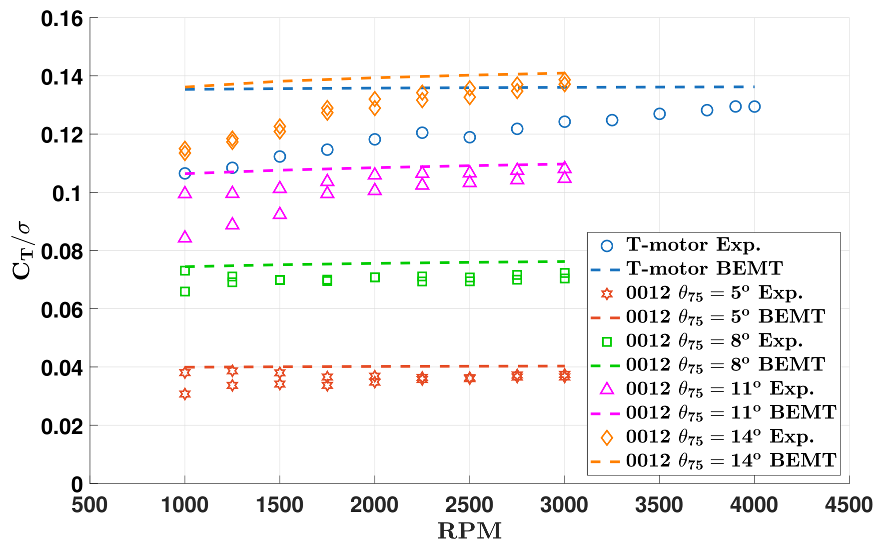

Figure 3.22: Thrust coefficient C_T/σ versus RPM for T-motor and NACA0012 rotor with Reynolds number empirical correction method.

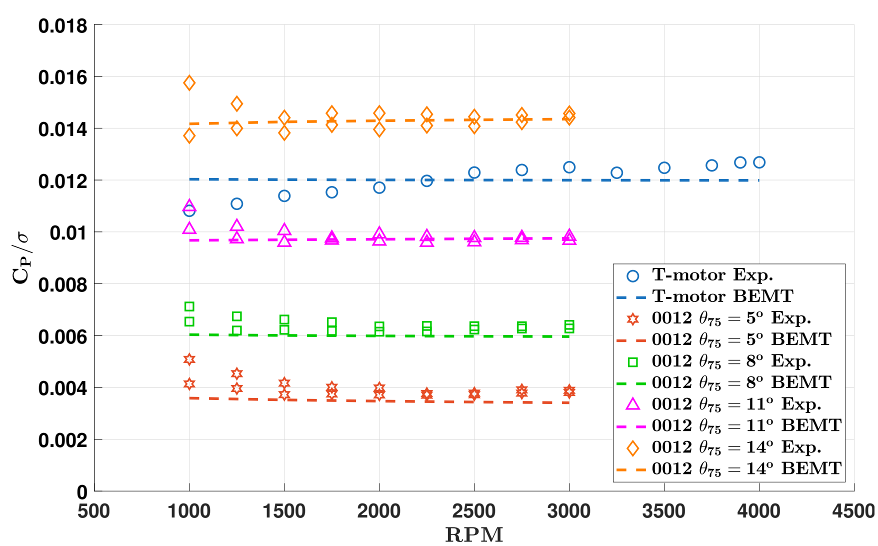

Figure 3.23: Power coefficient C_P/σ versus RPM for T-motor and NACA0012 rotor with Reynolds number empirical correction method.

3.5.2 Reynolds Number Interpolation Method

Figures 3.24 and 3.25 shows non-dimensional thrust and power normalized by solidity with BEMT results using the interpolation method described in Section 3.2.2. Here, the BEMT results match the experimental results with greater accuracy than the empirical approach. At low RPMs, the lower values for C_T are captured. At greater RPMs, the greater values for C_T are also captured and within the experimental data points collected. For C_P, there is again greater correlation with experimental results, with the negative slope captured across the range of RPMs. This improvement in BEMT predictions is a direct result of capturing the Reynolds number effects in the CFD airfoil table data. For C_T/σ, this error varies between 0% and 10% between the predicted and experimental results. For C_P/σ, the error varies between 0% and 10%. Thus, there is less error compared to the empirical correction approach.

At lower collectives of $\theta_{75} = 5°$ and 8°, there is less effect of RPM, and therefore Reynolds number, in the C_T/σ and C_P/σ data. This is because the airfoil cross sections at these lower collectives do not achieve a high enough angle of attack to enter the stall region of the C_l versus α plot where the greatest distinction as a result of Reynolds number effects occurs. Therefore, there is less dependence on Reynolds number effects at reduced collectives compared to greater collectives.

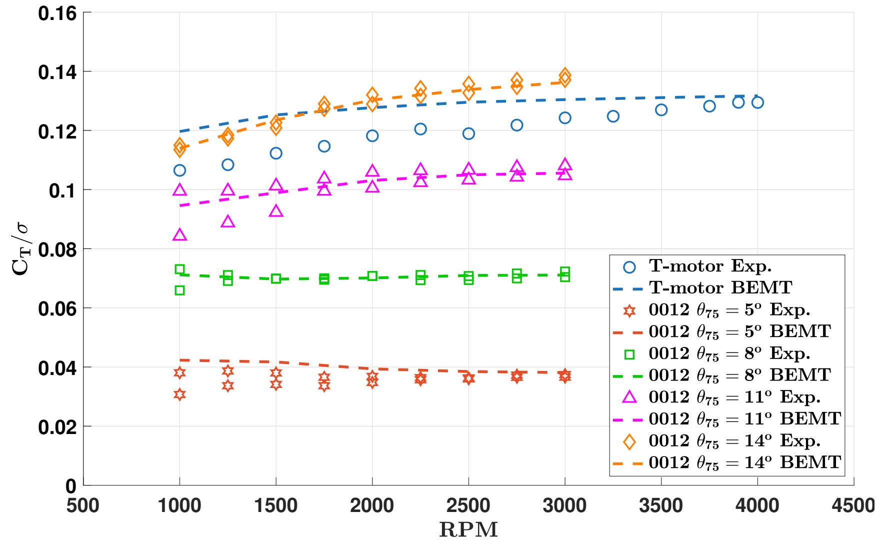

Figure 3.24: Thrust coefficient C_T/σ versus RPM for T-motor and NACA0012 rotor with Reynolds number interpolation method.

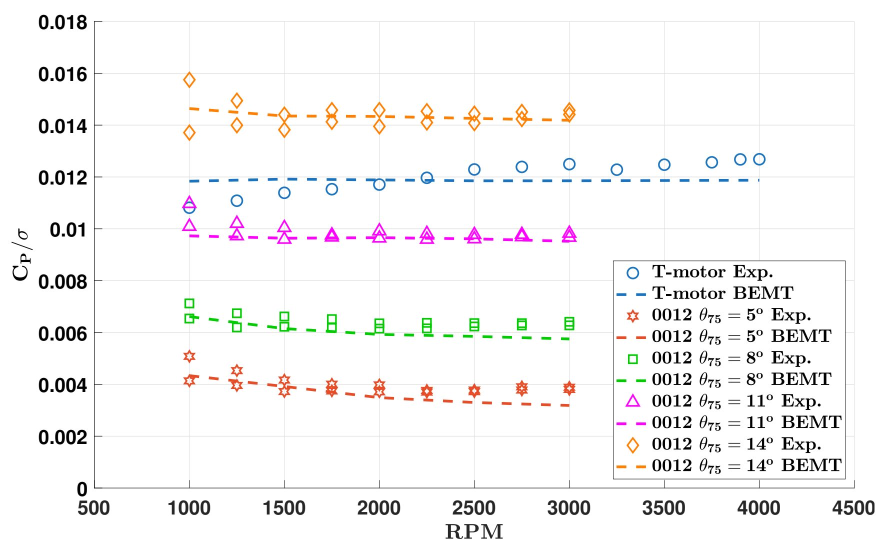

Figure 3.25: Power coefficient C_P/σ versus RPM for T-motor and NACA0012 rotor with Reynolds number interpolation method.

3.5.3 Steady Performance Results

Figure 3.26 shows power versus thrust coefficient normalized by solidity. The spread in the data is again a result of Reynolds number variation effects caused by RPM. BEMT results use the Reynolds number interpolation method with varying collectives to capture the trend for both the NACA0012 and T-motor rotor. Results indicate good agreement with experimental data.

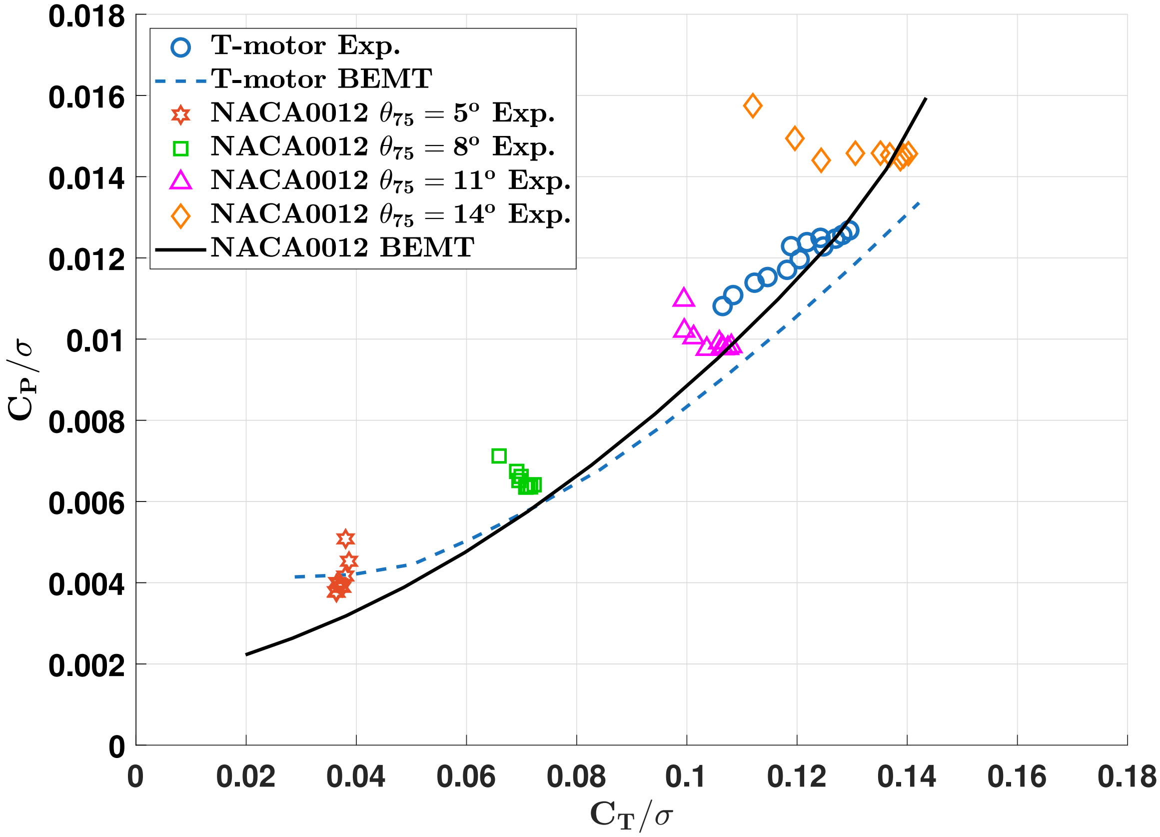

Figure 3.26: Power coefficient C_P/σ versus thrust coefficient C_T/σ for T-motor and NACA0012 rotors.

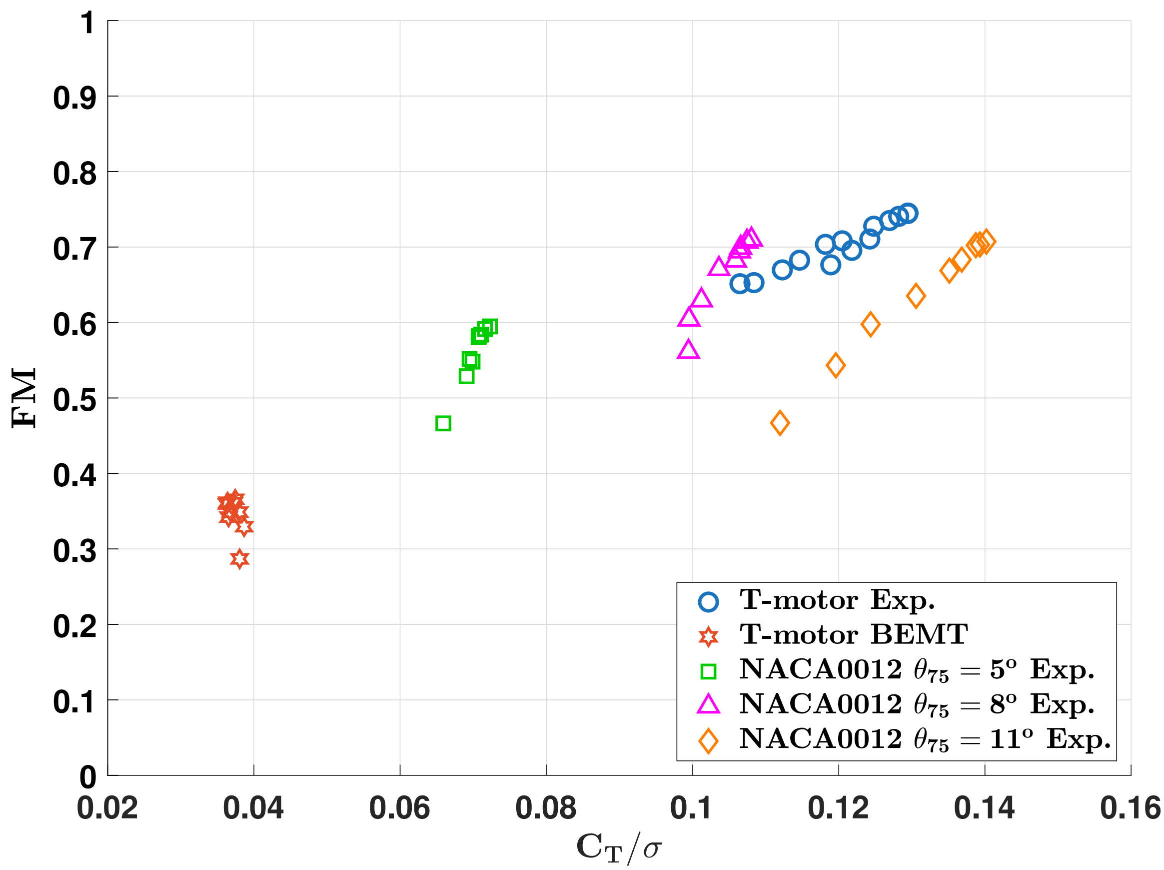

Figure 3.27: Figure of Merit FM versus thrust coefficient C_T/σ for T-motor and NACA0012 rotors.

Figure 3.28 shows dimensional thrust versus RPM and Figure 3.29 shows dimensional power for both the T-motor and NACA0012 rotors with BEMT Reynolds number interpolation prediction. These predicted BEMT solutions again show good correlation with experimental data, with an error not exceeding 6% in thrust and 6% in power. For a given RPM, the T-motor rotor produces greater thrust and extracts more power than all NACA0012 rotors excluding the $\theta_{75} = 14°$ rotor.

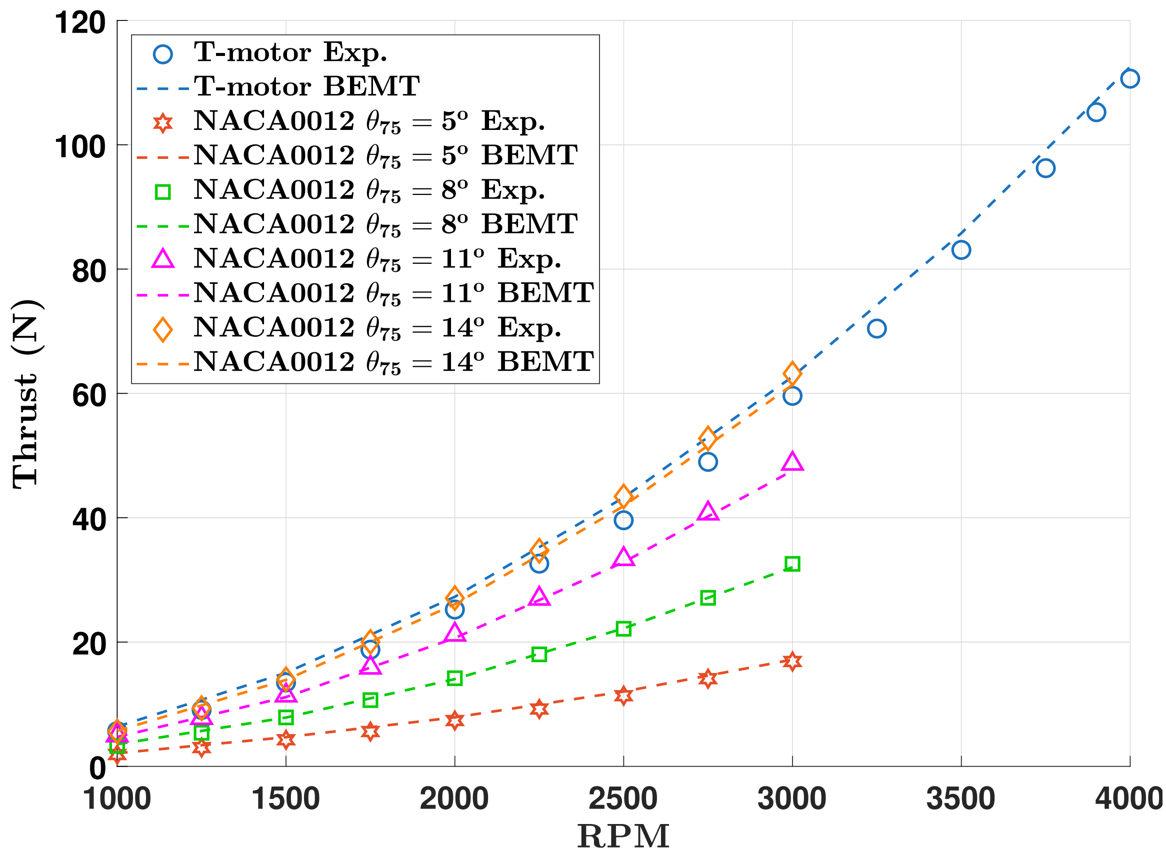

Figure 3.28: Thrust versus RPM for T-motor and NACA0012 rotors.

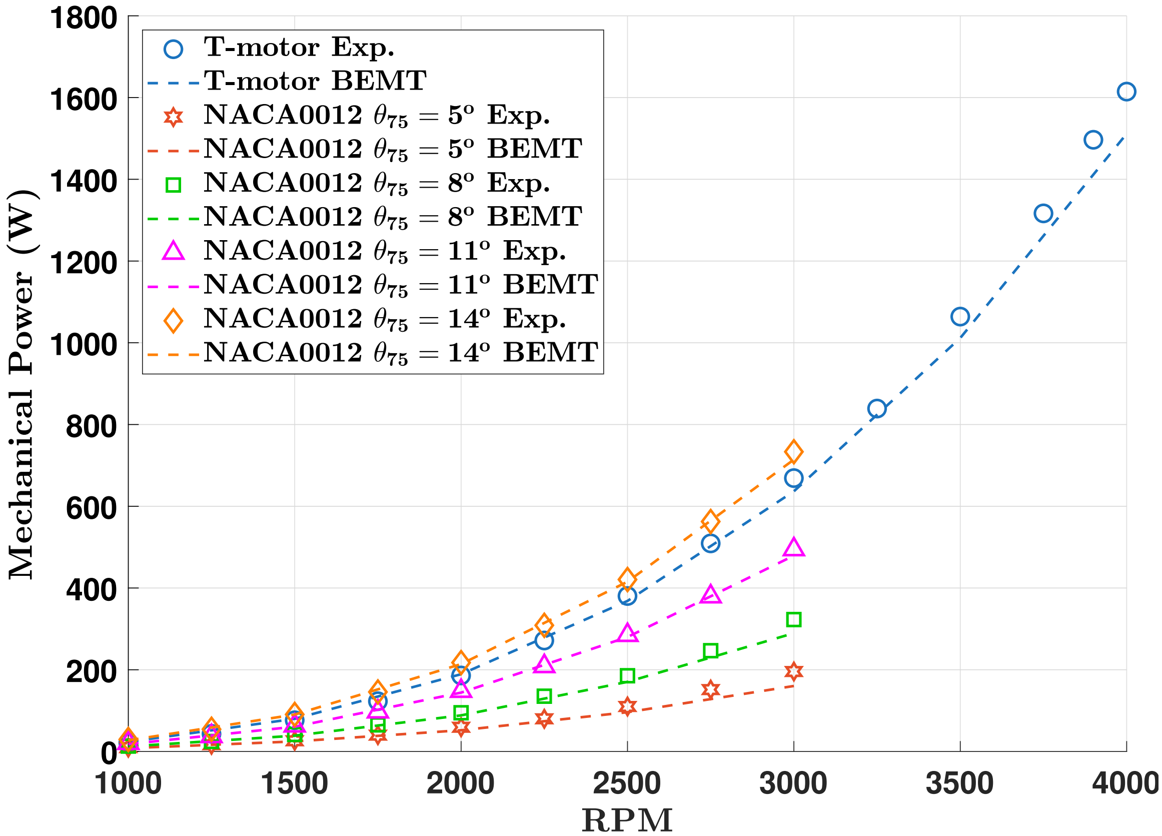

Figure 3.29: Mechanical power versus RPM for T-motor and NACA0012 rotors.

Figure 3.30 shows power loading versus disk loading. For the entire range of disk disk loading, the T-motor rotor produces maximum power loading, indicating it is a well tuned rotor for a range of RPMs in hover.

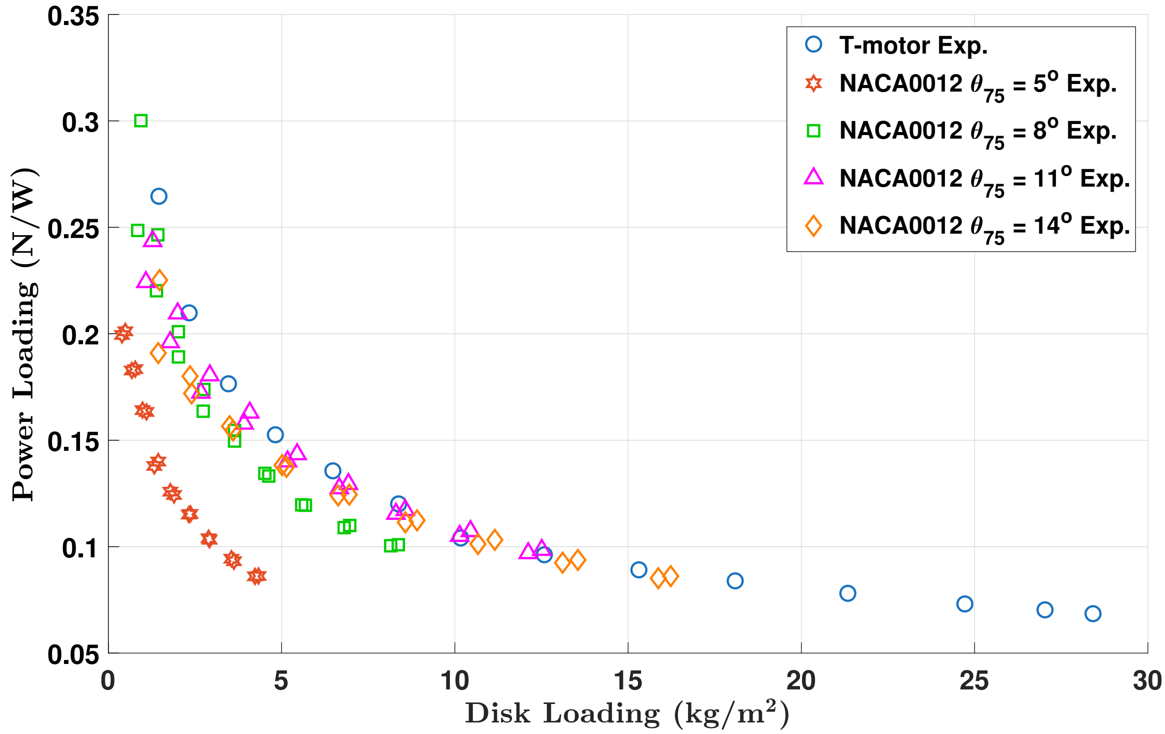

Figure 3.30: Power loading versus disk loading for T-motor and NACA0012 rotors.

3.6 Transient Rotor Performance

Transient tests were performed to better understand the performance of the rotor, motor and ESC due to RPM variation. The data collected describes how the outputs change for a given set of inputs. The data is a function of the frequencies excited which can be determined by transferring time domain data to the frequency domain. This is done using a Comprehensive Identification from Frequency Responses (CIFER) tool [31]. The input for all cases is the PWM signal commanding the ESC. Unlike the steady hover tests, for the RPM transient tests, the T-motor rotor was the only rotor tested.

3.6.1 Step Response

With a PWM step input of approximately 1430 to 1525, the RPM increases from 2500 to 3000 within 0.15 seconds. An example of this input-output relationship is shown in Figure 3.31. The RPM data is recorded at a rate of once every revolution. Therefore, the rate of a new RPM reading is dependent on the rotational speed.

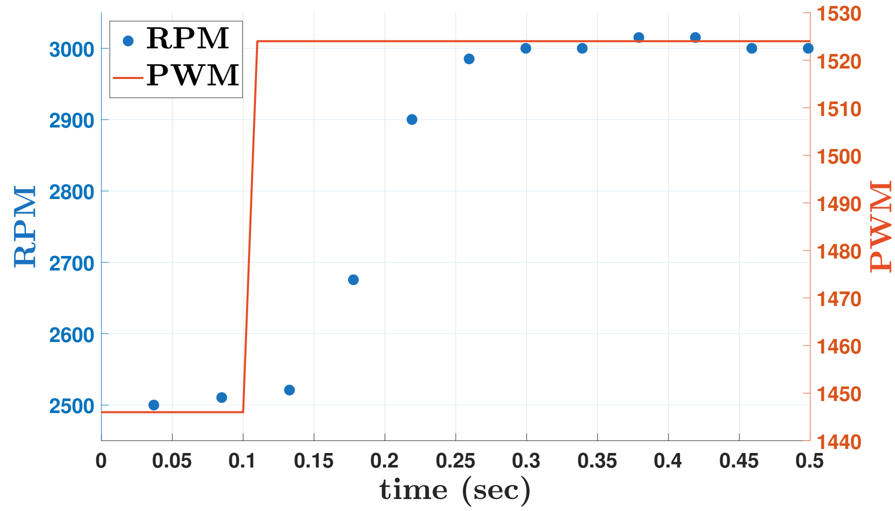

Figure 3.31: Step up response of RPM with an input PWM command.

A prediction for thrust was generated based on a constant relationship between thrust and RPM^2. Thrust is defined by the static aerodynamic thrust equation:

$$T = F_Z = \rho A \Omega^2 R^2 C_T \tag{3.11}$$

Plotting this relationship in the time domain, good agreement is found between the predicted thrust and experimental thrust as shown in Figures 3.32 and 3.33. Calculating the thrust based on the transient RPM using the constant relationship described in Equation 3.11, the difference in thrust is within 2 N (4%).

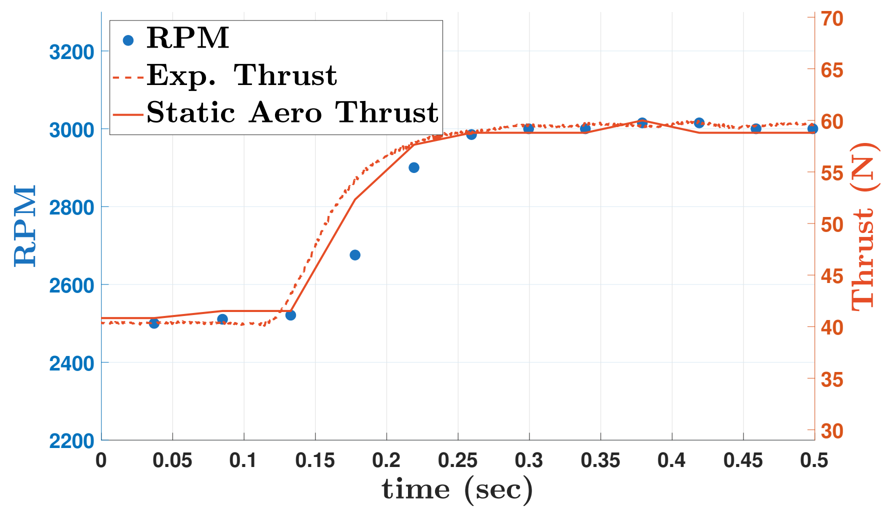

Figure 3.32: Step up response comparison of RPM and thrust.

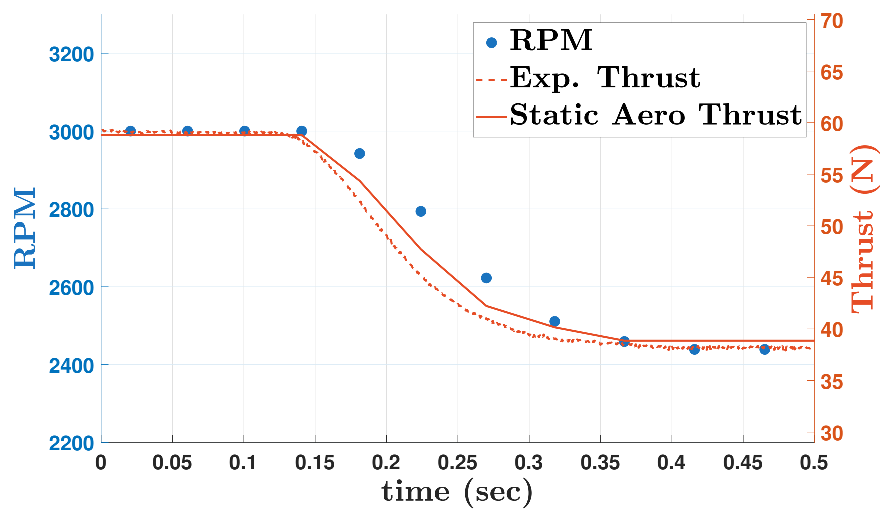

Figure 3.33: Step down response comparison of RPM and thrust.

A prediction for torque was generated based on the static aerodynamic torque and motor and rotor inertia. Motor and rotor inertia was found using SolidWorks to be $I_{tot} = .002983$ kg m^2. Total torque is then defined by:

$$Q = M_Z = I\dot{\Omega} + \rho A \Omega^2 R^3 C_Q \tag{3.12}$$

The change in rotational speed is dependent on consecutive RPM measurements and the time difference of the two readings, as defined by:

$$\dot{\Omega} = \frac{\Omega_{t+\Delta t} - \Omega_{t-\Delta t}}{2\Delta t} \tag{3.13}$$

Step up and step down plots for torque are shown in Figures 3.34 and 3.35. These plots show good agreement between the predicted torque and experimentally measured torque. Due to the RPM velocity inertia relationship, there is significant sensitivity in the prediction with small change in RPM which is seen in the steady response following the step change. As expected, inertia from the motor and rotor causes an overshoot which can be observed.

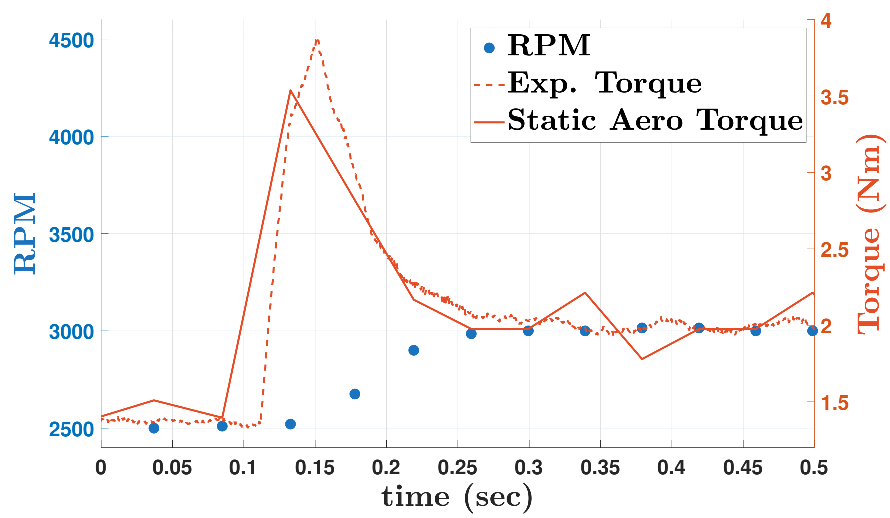

Figure 3.34: Step up response comparison of RPM and torque.

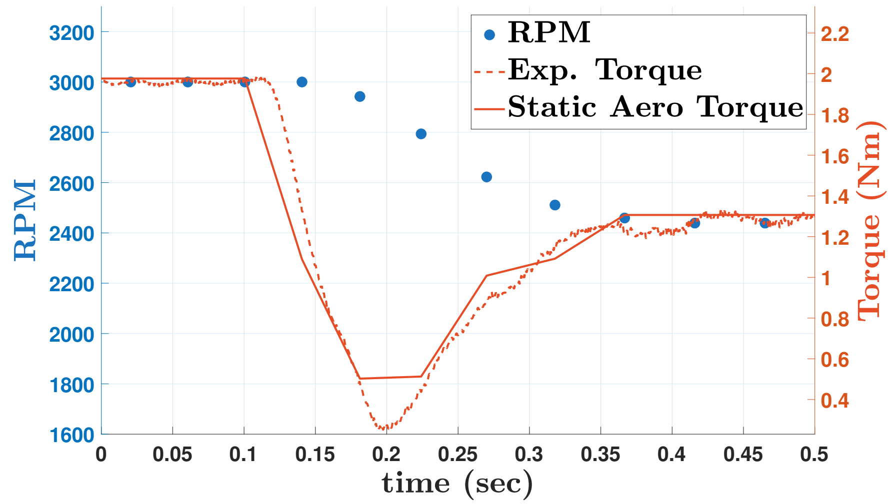

Figure 3.35: Step down response comparison of RPM and torque.

3.6.2 Identification of Thrust Responses

Figure 3.36 shows the chirp PWM input and the resulting RPM output. Over the duration of the test, the RPM tends to increase with time. This is assumed to be because the ESC and motor is capable of greater positive angular acceleration than negative acceleration.

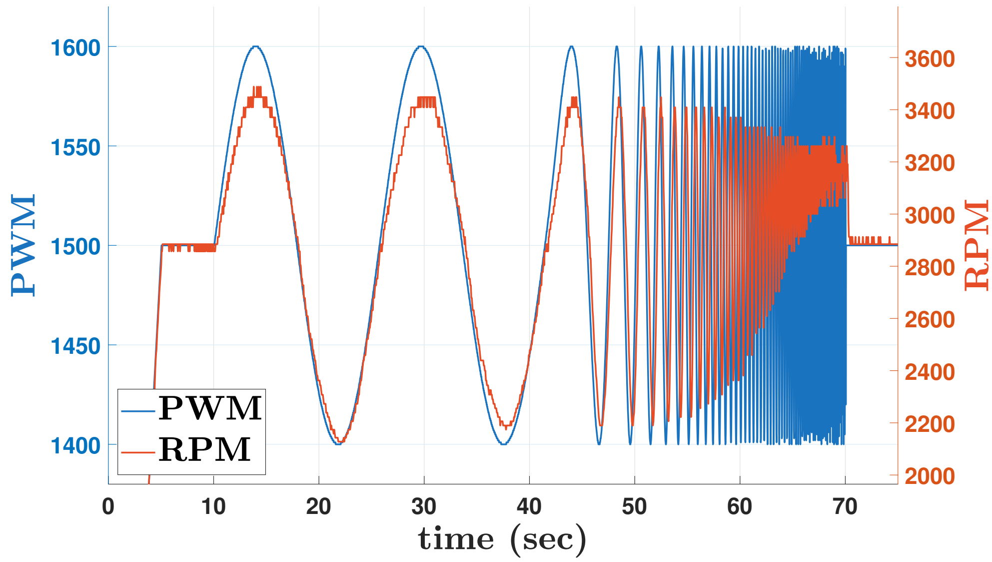

Figure 3.36: Chirp response PWM and RPM versus time.

Figure 3.37 shows thrust output with RPM in the time domain. Using the static thrust equation based on a constant thrust coefficient value, Figure 3.38 shows good correlation with the experimental measured thrust for the frequency range tested. This indicates that the thrust coefficient does not vary with frequency. The time history data was then put into the frequency response identification tool, FRESPID, in CIFER. The linear thrust responses to RPM and RPM^2 are shown in Equations 3.14 and 3.15. FRESPID was used to generate frequency responses for a series of windows optimized for the frequency range of the experiment. Then the responses were optimally combined in the window combination tool, Composite. Figure 3.39 shows magnitude, phase, and coherence results for PWM input amplitudes of 50, 100, and 150 for both the RPM and RPM^2. Notice that the phase for the frequency responses due to RPM and RPM^2 are the same, and the magnitude is shifted by 55.3 dB which is the expected $2\Omega_0$ difference between Equations 3.14 and 3.15. Since the magnitude remains constant and the phase remains around 0°, the transfer function is expected to be a constant gain. This implies that there are no aerodynamic inflow dynamics in the frequency range of interest. Finally, coherence is a measure of the data linearity, signal to noise ratio, and if there is enough data captured in the window. Reliable data is defined to have a coherence of 0.6 and above [31]. Since Figure 3.39 shows a coherence close to 1 for all of the frequency range, the data is well suited for system identification. Therefore, both inputs are valid.

$$\frac{\Delta T}{\Delta \Omega} = \rho A (2\Omega_0) R^2 C_T \tag{3.14}$$

$$\frac{\Delta T}{\Delta(\Omega^2)} = \rho A R^2 C_T \tag{3.15}$$

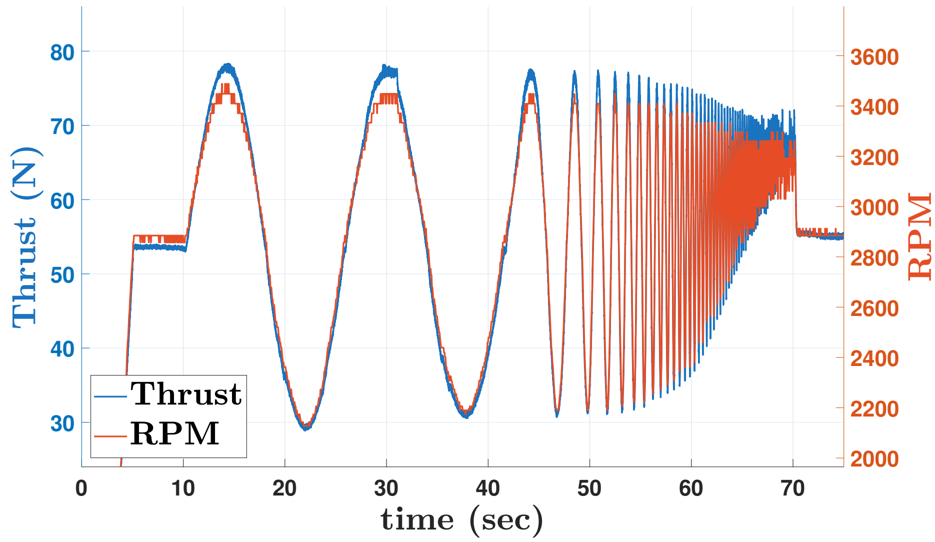

Figure 3.37: Chirp response of Thrust and RPM versus time.

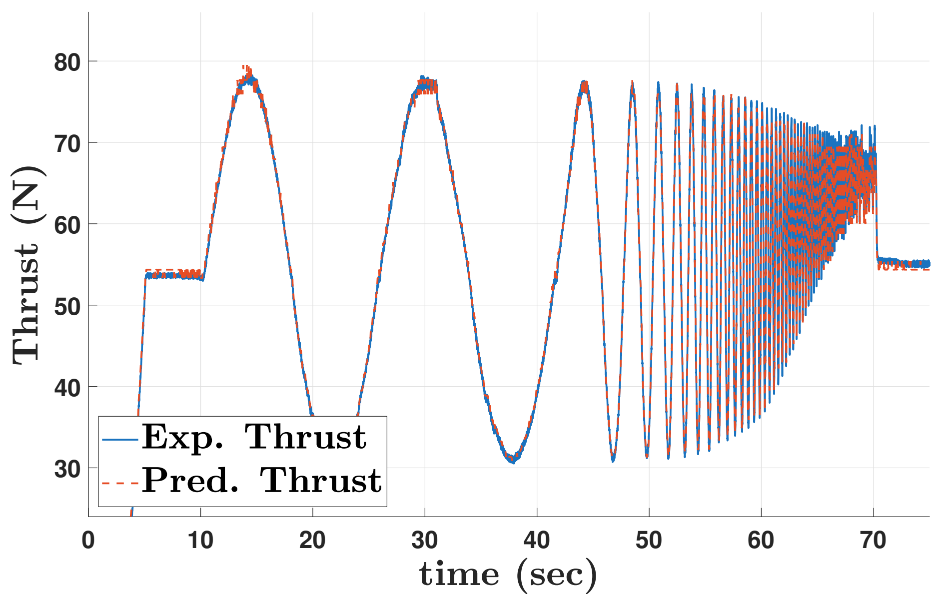

Figure 3.38: Chirp response of experimental measured thrust and predicted thrust based on static thrust equation.

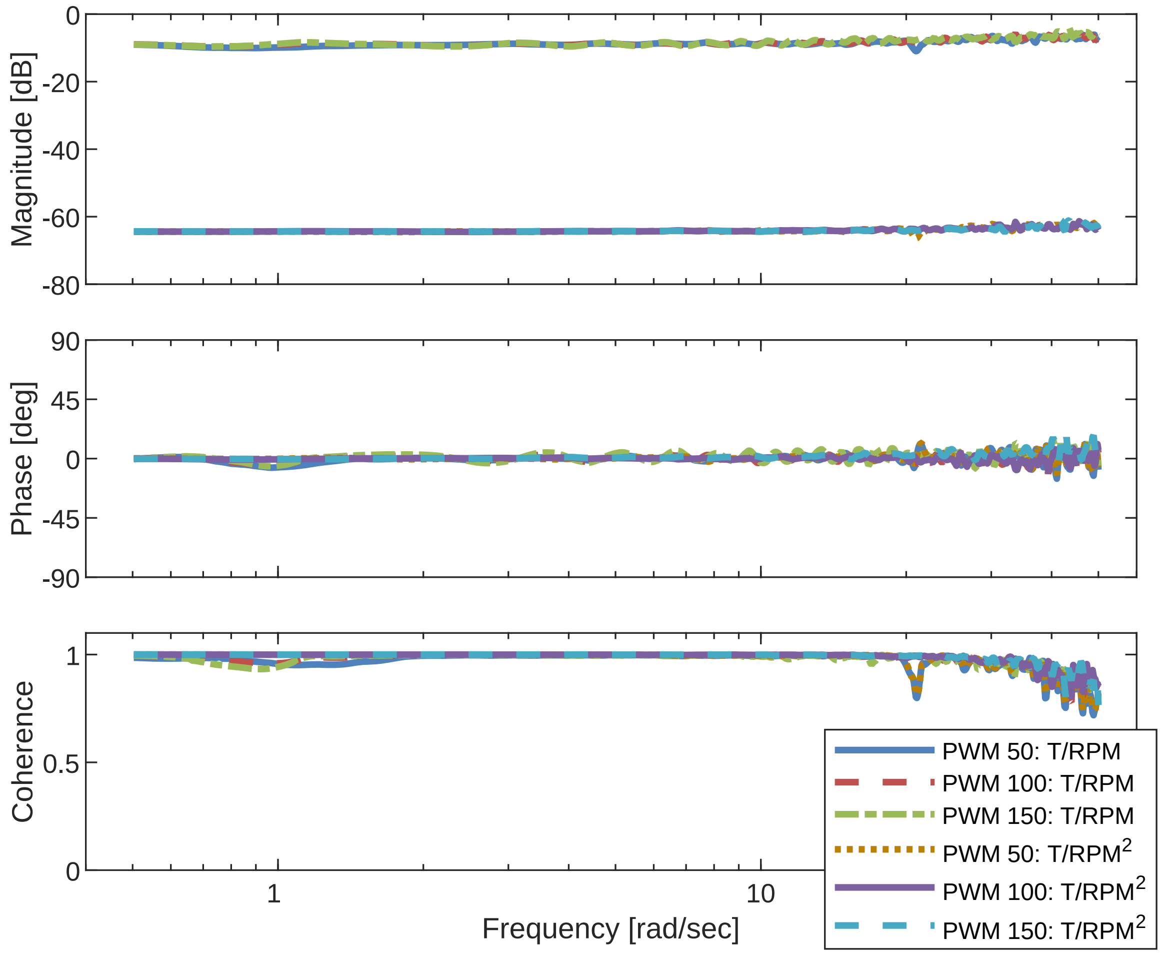

Figure 3.39: Thrust due to RPM and RPM^2 frequency response.

Through inspection of Equations 3.14 and 3.15 a pure gain transfer function is expected for thrust due to RPM and RPM^2 which agrees with the assessment of the Bode plot in Figure 3.39. These transfer functions were fitted in the frequency response fitting feature in CIFER, NAVFIT, for the 3 PWM amplitude sweeps shown in Equations 3.16 and 3.17 for RPM and RPM^2 respectively. These equations follow the form of Equation 3.11. Frequency ranges listed in Table 3.1 were chosen for the specified PWM amplitude tests. Associated error of the fitted transfer function to the frequency response data is also shown in Table 3.1 with values of cost. All of the frequency response functions have a cost below 50 which is considered to be a perfect model[31]. However, the fit of RPM^2 to thrust improved the cost significantly compared to the fit of RPM to thrust. Note that the thrust measurement was found to lead the RPM measurement by 24 to 30 ms.

Table 3.1: NAVFIT: Frequency ranges and costs for T/RPM and T/RPM^2

PWM	Frequency Range	RPM Cost	RPM^2 Cost
50	0.4–55	12.75	6.15
100	0.4–50	17.45	6.82
150	0.4–50	23.96	4.88

$$\begin{aligned} \text{50 PWM:} \quad & \frac{T}{\Omega}e^{-0.025s} = 0.364 \\ \text{100 PWM:} \quad & \frac{T}{\Omega}e^{-0.030s} = 0.374 \\ \text{150 PWM:} \quad & \frac{T}{\Omega}e^{-0.024s} = 0.378 \end{aligned} \tag{3.16}$$

$$\begin{aligned} \text{50 PWM:} \quad & \frac{T}{\Omega^2}e^{-0.025s} = 6.19 * 10^{-4} \\ \text{100 PWM:} \quad & \frac{T}{\Omega^2}e^{-0.030s} = 6.23 * 10^{-4} \\ \text{150 PWM:} \quad & \frac{T}{\Omega^2}e^{-0.024s} = 6.16 * 10^{-4} \end{aligned} \tag{3.17}$$

3.6.3 Identification of Torque Responses

In the same manner, Equations 3.18 and 3.19 are the linear frequency responses for torque due to RPM and RPM^2. Figures 3.40 and 3.41 show torque output with RPM in the time domain and with RPM and RPM^2 in the frequency domain respectively. It can be seen in Figure 3.40 that with increasing RPM frequency, there is increased torque overshoot, which reaches nearly twice the steady state torque. The magnitude plot in Figure 3.41 shows an increase in magnitude with a slope of 20 dB/decade and an increase in phase that rolls off at 90°. This indicates that the transfer function of torque due to RPM^2 can be represented as a zero. Once again, the magnitudes of the frequency response with RPM and RPM^2 vary by the $2\Omega_0$, 55.3 dB. However, since the magnitude and phase of the thrust and torque responses due to RPM is more wavy than the responses due to RPM^2 around 0.7–1.8 rad/s, the frequency responses of torque due to both inputs were compared to simulated doublets later on to determine which is more accurate.

$$\frac{\Delta Q}{\Delta \Omega} = I\,s + \rho A(2\Omega_0)R^3 C_Q \tag{3.18}$$

$$\frac{\Delta Q}{\Delta(\Omega^2)} = \frac{I}{2\Omega_0}\,s + \rho A R^3 C_Q \tag{3.19}$$

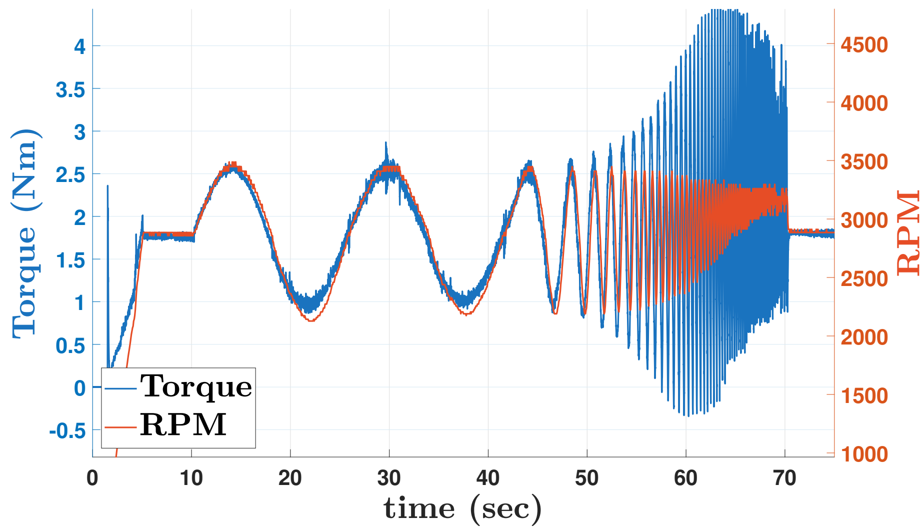

Figure 3.40: Chirp response of Torque and RPM versus time.

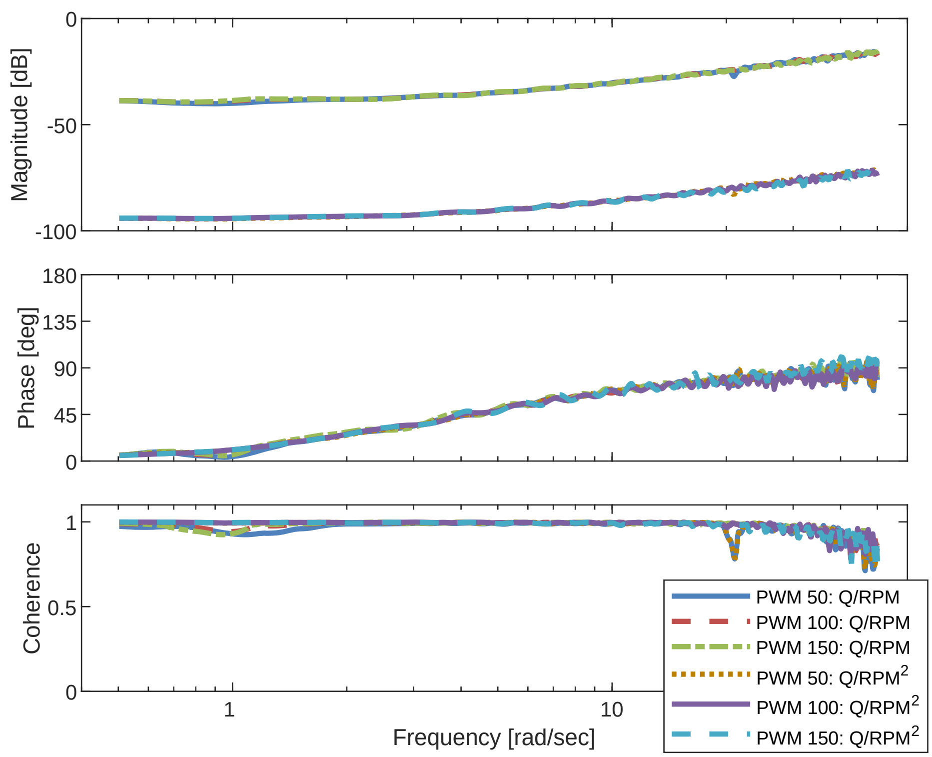

Figure 3.41: Torque due to RPM and RPM^2 frequency response.

Since linear torque responses can be derived for RPM and RPM^2, transfer functions were determined for both. Equations 3.18 and 3.19 imply that the transfer functions of torque due to RPM and RPM^2 have the form of a zero in the numerator which matches the analysis of the Bode plot in Figure 3.41. NAVFIT used this form to get the transfer function of torque due to RPM and RPM^2 for the 3 PWM amplitude sweeps shown in Equations 3.20 and 3.21 respectively. Frequency ranges listed in Table 3.2 were chosen for the specified PWM amplitude tests. Associated cost of the fitted transfer function to the frequency response data is also shown. Cost is an indicator used to describe the accuracy of the identification. As was found with thrust, all of the frequency response functions have a cost below 50 which is considered to be a nearly perfect model [31]. The costs of torque due to RPM and RPM^2 are roughly the same. Note that the thrust measurement was found to lead the RPM measurement by 24 to 30 ms. The zero for the torque response due to RPM and RPM^2 occurs at 3.9 and 4.2 rad/s respectively which can be seen in the the Bode plot in Figure 3.41. Lastly, a 24 to 30 ms time lead is observed.

Table 3.2: NAVFIT: Frequency ranges and costs for Q/RPM and Q/RPM^2

PWM	Frequency Range	RPM Cost	RPM^2 Cost
50	0.4–55	10.11	5.52
100	0.4–50	7.75	6.74
150	0.4–50	7.05	10.79

$$
\begin{aligned}
\text{50 PWM: } \frac{Q}{\Omega}e^{-0.025s} &= 2.86 \cdot 10^{-3}s + 0.0112 \\
\text{100 PWM: } \frac{Q}{\Omega}e^{-0.030s} &= 2.89 \cdot 10^{-3}s + 0.0115 \\
\text{150 PWM: } \frac{Q}{\Omega}e^{-0.024s} &= 2.84 \cdot 10^{-3}s + 0.0114
\end{aligned}
\tag{3.20}
$$

$$
\begin{aligned}
\text{50 PWM: } \frac{Q}{\Omega^2}e^{-0.025s} &= (4.75 \cdot 10^{-6}s + 1.95 * 10^{-5}) \\
\text{100 PWM: } \frac{Q}{\Omega^2}e^{-0.030s} &= (4.67 \cdot 10^{-6}s + 1.96 * 10^{-5}) \\
\text{150 PWM: } \frac{Q}{\Omega^2}e^{-0.024s} &= (4.38 \cdot 10^{-6}s + 1.98 * 10^{-5})
\end{aligned}
\tag{3.21}
$$

3.6.4 Time Delay in RPM Measurement

Since both the thrust and torque responses to RPM and RPM^2 have the same time lead, the time lead is assumed to be due to RPM measurement uncertainty. The torque and thrust were measured at a rate of 5 kHz. An infrared reflective photoelectric sensor was used to measure the RPM which measured at a rate of 50 Hz, once every revolution. Therefore, RPM measurement would be expected to have a time delay similar to a zero-order hold of 10 ms. The other 14 to 20 ms of the RPM measurement's time delay is believed to be due to measurement limitations of the infrared reflective photoelectric sensor. Since the time delay was constant for thrust and torque due to RPM and RPM^2 responses at each PWM amplitude, the delay was removed from the frequency responses shown in Figures 3.39 and

3.41.

3.6.5 Validation of CIFER Results

CIFER results were then used to estimate C_T, C_Q, and I values for the equations of thrust and torque. The derived transfer functions of thrust due to RPM and RPM^2, shown in Equations 3.14 and 3.15, can be compared to the transfer functions computed by NAVFIT, Equations 3.16 and 3.17, to compute C_T. Similarly, the derived transfer functions of torque due to RPM and RPM^2, shown in Equations 3.18 and 3.19, can be compared to the transfer functions computed by NAVFIT, Equations 3.20 and 3.21, to determine I and C_Q. C_T and C_Q were also calculated from steady hover results at 3000 RPM, and the moment of inertia was calculated in SolidWorks. C_T, C_Q, and I were compared between the steady hover results at 3000 RPM and the transient hover system identification results from CIFER. The differences in the values are shown in Table 3.3.

Table 3.3: Comparison between steady and transient hover values

	RPM	RPM^2
C_T	2.4–6.3%	3.4–4.6%
C_Q	3.8–6.3%	1.1–2.6%
I	3.1–4.8%	4.9–12.4%

3.6.6 Validity of RPM and RPM^2 as Inputs to Linear Responses

Linear models are currently found with RPM as the input. RPM is advantageous to being a state because it allows for constant mass matrix, simpler equations of motion, and the motor equations are already in terms of RPM. Since the frequency responses shown in Figs. 3.39 and 3.41 show that both RPM and RPM^2 inputs provide good fits to the test data, this research proved that RPM^2 is a valid input. To test if RPM or RPM^2 is a more accurate input, small and large amplitude doublets with torque as the input were simulated for Eqns. 3.12, 3.22, and 3.23 and are shown in Figs. 3.42 and 3.43. It can be seen that Eqn. 3.23 performs better than Eqn. 3.22.

$$\frac{\Omega}{Q} = \frac{1}{2.90 \cdot 10^{-3}s + 0.0114} \tag{3.22}$$

$$\frac{\Omega^2}{Q} = \frac{1}{4.60 \cdot 10^{-6}s + 1.93 \cdot 10^{-5}} \tag{3.23}$$

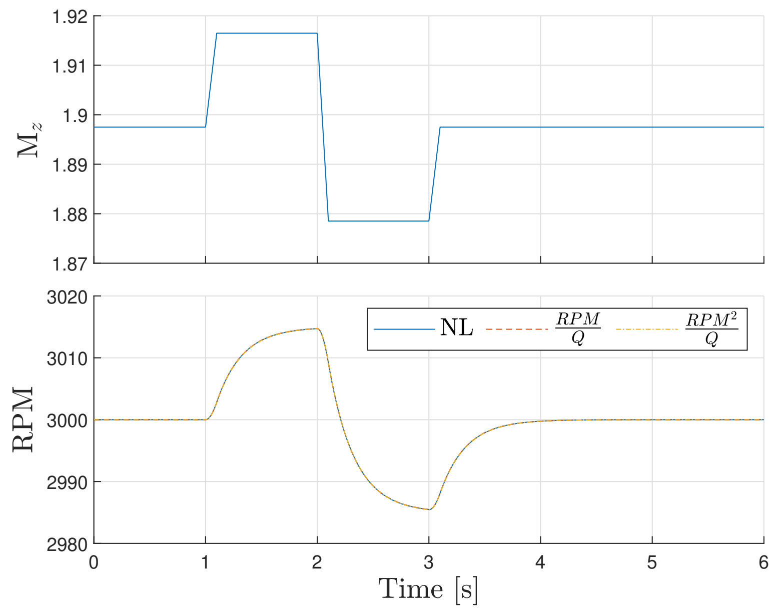

Figure 3.42: Small amplitude doublet

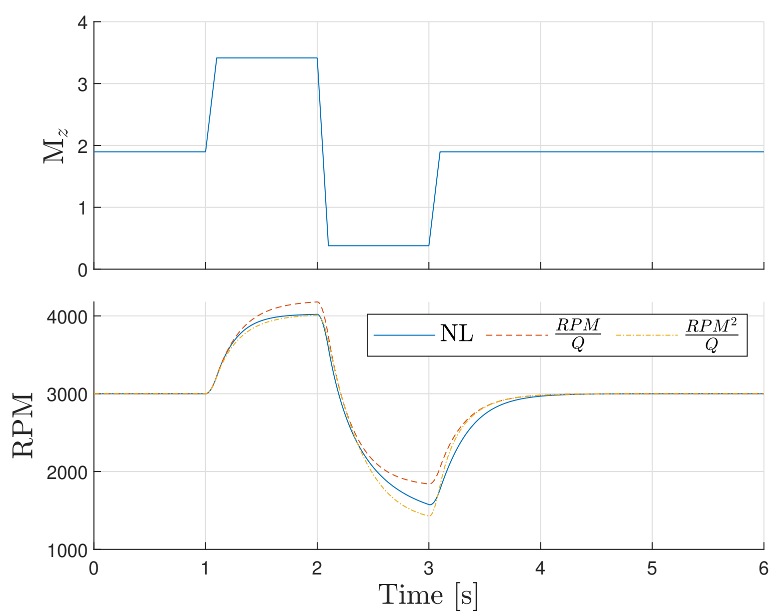

Figure 3.43: Large amplitude doublet

The RMS error is shown to increase with increasing doublet amplitude and increasing trim RPM in Fig. 3.44. However, both responses have an error less than 5% for nominal RPM and less than 10% for higher RPM. Note that there is still error using RPM^2. RPM^2 does not provide a global model since Eqn. 3.23 is dependent on $\dot{\Omega}$, but it is a closer approximation compared to RPM as an input about a given trim RPM.

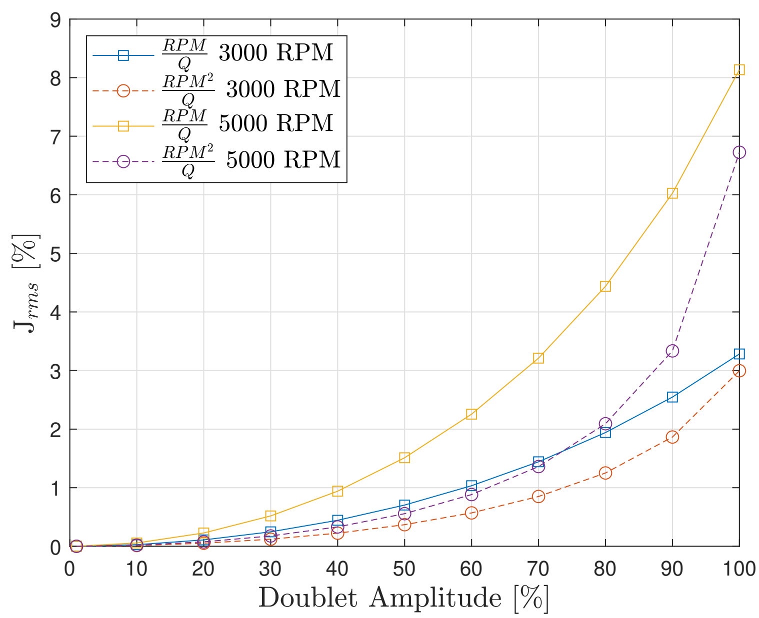

Figure 3.44: RMS error

3.7 Electrical Efficiency of System

The T-motor P80III 100 KV motor coupled with a Flame 80 A electronic speed controller (ESC) and rotor has additional power requirements due to inefficiencies in the system. These inefficiencies can be quantified by measuring electrical voltage and current into the ESC and comparing with the mechanical shaft power of the rotor as defined by

Equation 3.24.

$$\eta = \frac{P_{mech}}{P_{elec}} \tag{3.24}$$

Figure 3.45 shows the electrical power and mechanical power for the T-motor system. At rotational speeds below 1000 RPM, the motor experiences its lowest efficiency equal to 50% and below. The efficiency increases dramatically in the range of 1000-2500 RPM from 60% to 90%. The efficiency is then near constant at approximately 90%. This trend correlates well with past studies such as the electrical efficiency study of a DJI Phantom motor and ESC system as found by Russell et al. [12].

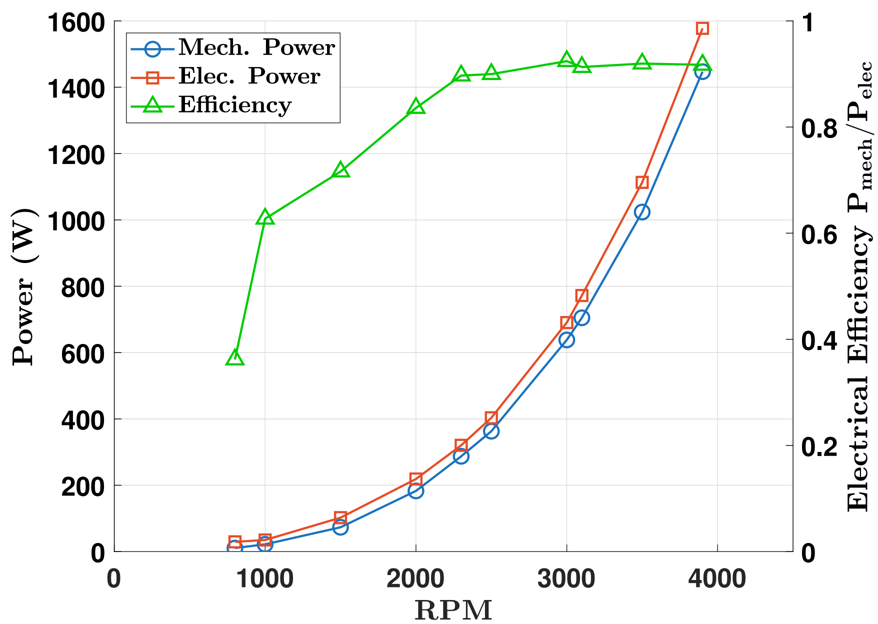

Figure 3.45: Experimental hover power and electrical efficiency for T-motor rotor, motor, and ESC system.

3.8 Chapter Summary

The effect of Reynolds number on small scale rotors has been characterized for Reynolds numbers in the range of 50,000 to 500,000. Experimental results indicate reduced thrust and increased power with decreasing Reynolds number. The empirical method described by Yamauchi and Johnson is found to only be valid for greater Reynolds numbers such as Re $> 1{,}000{,}000$. Experimental thrust and power results show dependence on Reynolds number variation along the span and with RPM for the 28 inch diameter rotors tested. The interpolation method which uses multiple airfoil tables generated at different Reynolds number showed good agreement with experimental results, indicating strong dependence on accuracy of airfoil C_l and C_d data.

System identification showed linear frequency responses between thrust and torque with RPM and RPM^2 in hover. Similar results for C_T and C_Q were calculated from both hover and transient data. Torque's frequency responses were used to derive the moment of inertia from the transient data which was within 15% to the moment of inertia found from SolidWorks. Additionally, modeling with RPM^2 as the input proved to be valid over a wider RPM range about the trim RPM than modeling with RPM as the input.

Electrical efficiency of the ESC and motor system peaks at 90% above 2000 RPM and has significantly reduced efficiency below 2000 RPM.

Chapter 4: Shrouded and Isolated Rotor Performance Comparison

For many electric vertical take-off and landing aircraft, shrouds are being considered to improve the safety and performance over an equivalently sized open rotor. However, there is a lack of public information for shrouded rotors at larger scales with Reynolds numbers up to 500,000. Collecting such data is useful in quantifying performance benefits between a shrouded and isolated rotor as well as validating CFD for shrouded rotor configurations. Thus, the shrouded and isolated rotor were tested in static hover conditions using the NACA0012 and T-motor rotor. The T-motor rotor was also tested in low speed wind tunnel conditions up to $\mu = 0.06$. These results were generated to validate Helios CFD and to draw performance related conclusions.

4.1 Hover Results

4.1.1 T-motor Rotor

The experimental test setup includes two load cells: one measures rotor loads and the second measures shroud loads as described in Section 2.1.4. For the shrouded rotor, the sum of thrust is equivalent to the thrust of the rotor and thrust of the shroud as shown in

Equation 4.1.

$$T = T_{rotor} + T_{shroud} \tag{4.1}$$

Figure 4.1 shows thrust versus RPM for the isolated rotor and shrouded rotor cases. The shrouded rotor components T_{rotor} and T_{shroud} are also plotted to investigate the ratio of thrust between the rotor and shroud. T_{rotor} is the rotor thrust component and T_{shroud} is the shroud thrust component of the shrouded rotor system. The shroud is found to account for 20% and the rotor 80% of the total thrust of the shrouded rotor system. The total shrouded rotor thrust was found to be approximately equivalent to the isolated rotor thrust for the same RPM.

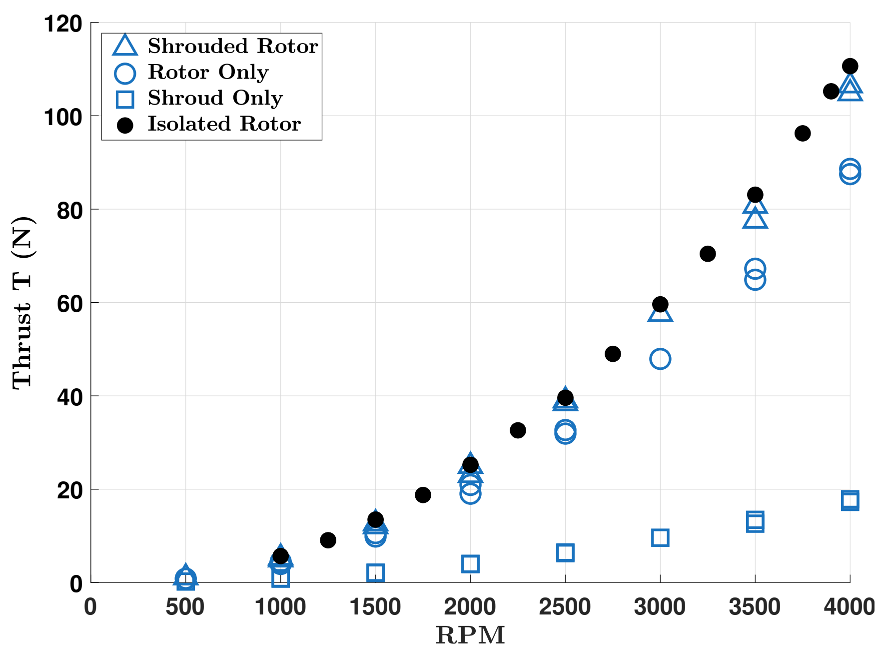

Figure 4.1: Thrust T versus RPM for shrouded and isolated T-motor rotor in hover.

As shown in Figure 4.2, for the same RPM, the shrouded rotor requires similar power as the isolated rotor.

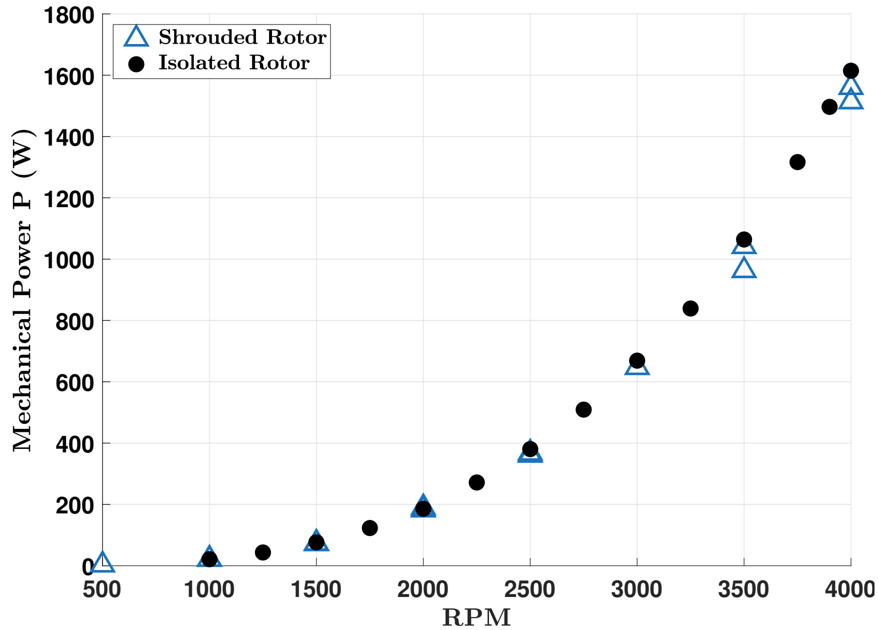

Figure 4.2: Mechanical power P versus RPM for shrouded and isolated T-motor rotor in hover.

Figure 4.3 shows thrust versus power. Again, the isolated rotor and shrouded rotor generate similar thrust for the same power.

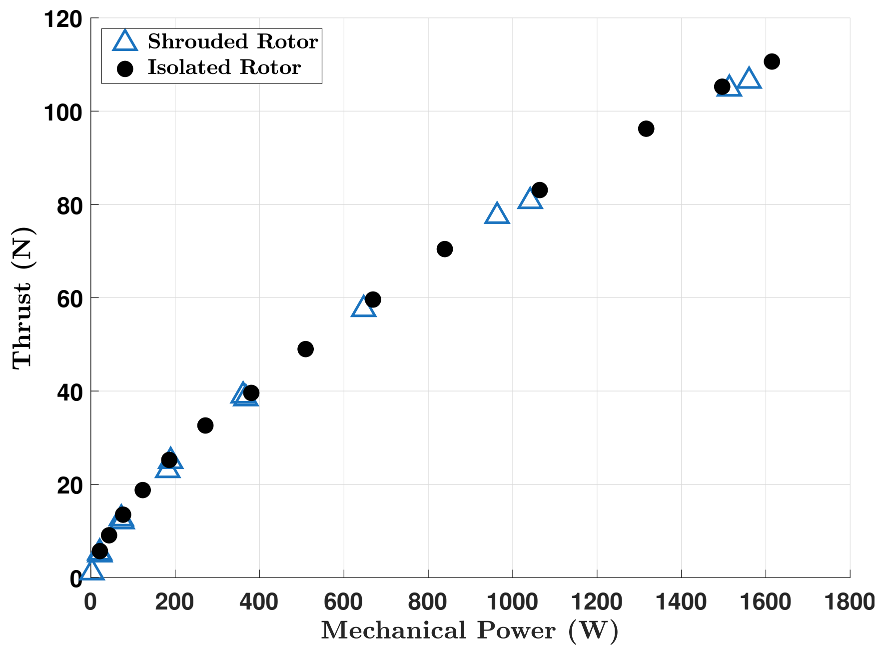

Figure 4.3: Thrust T versus mechanical power P for shrouded and isolated T-motor rotor in hover.

Power loading is used as the principal metric for hover performance. The greater power loading, the more efficient the system. The equations for power loading of the isolated rotor and shrouded rotor system are defined by:

$$PL = \frac{T}{P} \tag{4.2}$$

Disk loading is defined as thrust per disk area. Because both the shrouded rotor and isolated rotor use the same rotor, the rotor disk area for both configurations are the same. A power loading versus disk loading plot is shown in Figure 4.4. Again, this plot shows that the isolated rotor and shrouded rotor have similar performance.

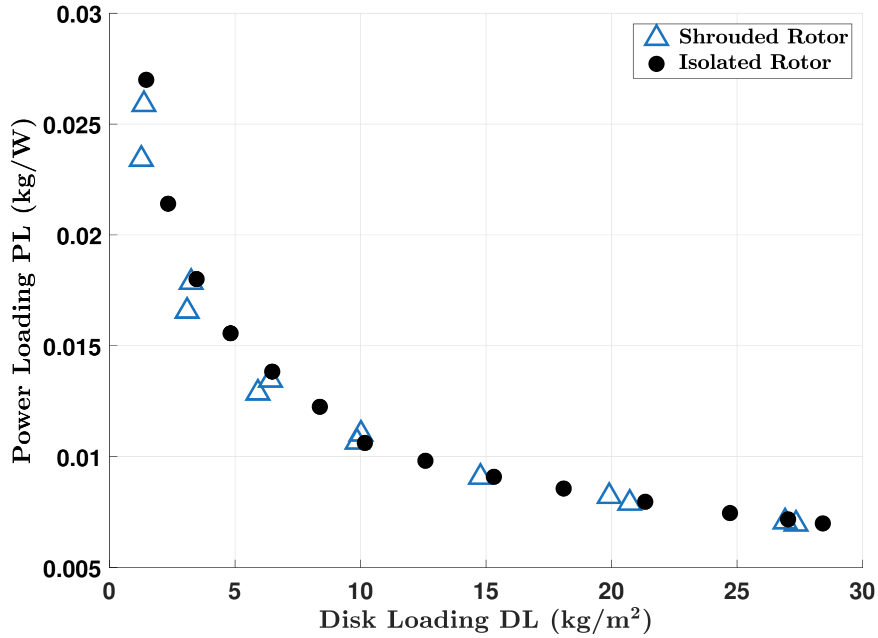

Figure 4.4: Power loading PL versus disk loading DL for shrouded and isolated T-motor rotor in hover.

The rotor thrust coefficient is a non-dimensional coefficient used to define the thrust of a rotor. For the isolated rotor, the rotor thrust is scaled relative to tip speed, blade area and air density as defined by Equation 4.3. For both the shrouded rotor and isolated rotor, the solidity σ is defined by the rotor blade.

$$\frac{C_T}{\sigma} = \frac{T}{\rho A_b (\Omega R)^2} \tag{4.3}$$

Thrust coefficient versus RPM is shown in Figure 4.5. With increasing RPM, C_T/σ increases due to Reynolds number effects. For all RPMs, the shroud component produces $C_T/\sigma \approx 0.02$ while the rotor component increases from $C_T/\sigma = 0.06$ to 0.1. The total shrouded rotor C_T/σ produces similar thrust to the isolated rotor.

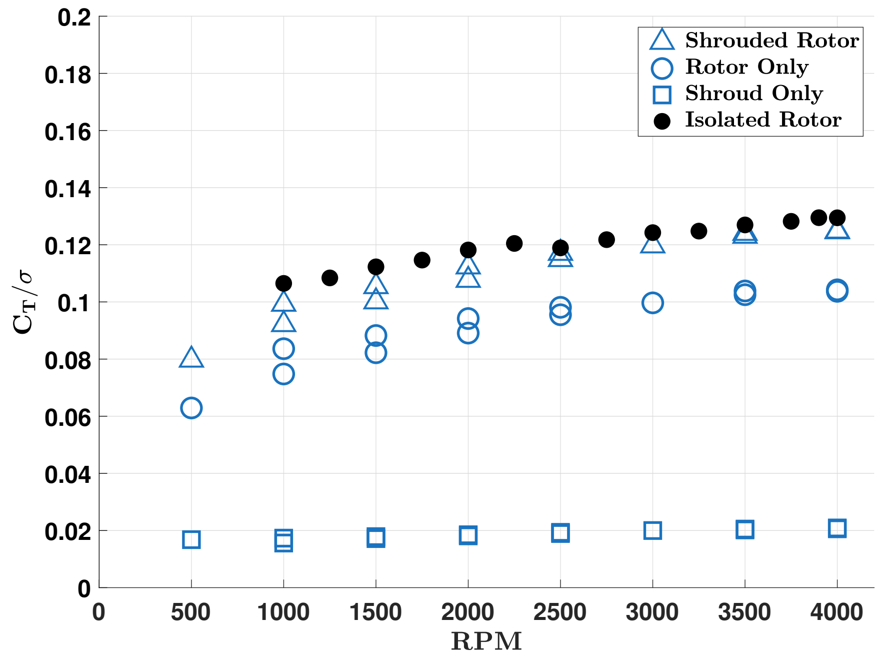

Figure 4.5: Coefficient of thrust C_T versus RPM for shrouded and isolated T-motor rotor in hover.

Power coefficient versus RPM is shown in Figure 4.6. With increasing RPM, C_P/σ increases due to Reynolds number effects. For all RPMs, the shrouded rotor requires similar C_P/σ as the isolated rotor.

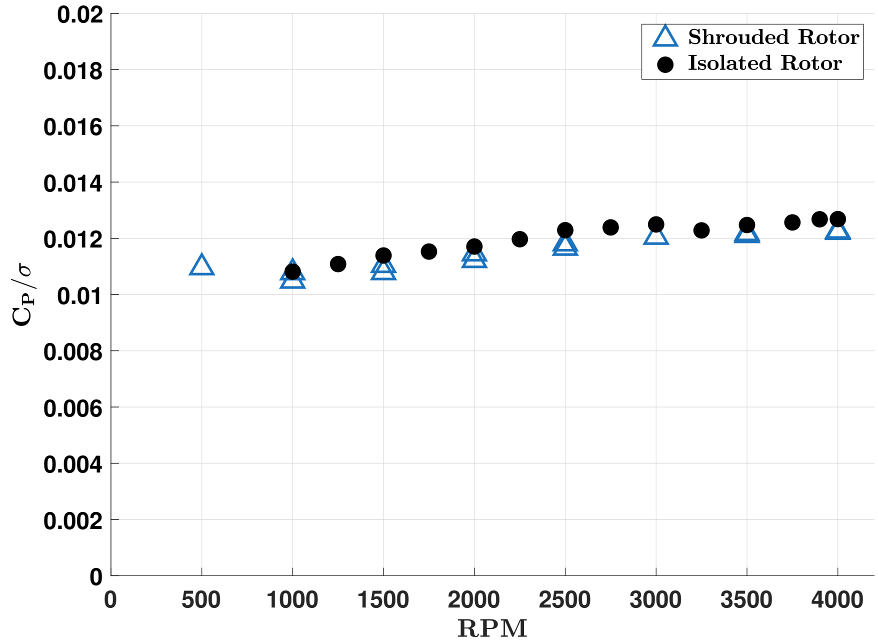

Figure 4.6: Coefficient of power C_P versus RPM for shrouded and isolated T-motor rotor in hover.

With the T-motor rotor, the shrouded rotor performance was similar to the isolated rotor with no net gain or loss in efficiency. A reason for this is likely due to the rotor operating at too low of a collective in an inefficient operating zone. Another potential reason is the tip clearance is too large, and thus, the shroud wall has less of an advantage in reducing induced drag losses. Similarly, the taper of the T-motor rotor is too large due to tip clearance. To investigate this further, the NACA0012 rotor with varying collective angles and constant chord distribution was tested next.

4.1.2 NACA0012 Rotor

The NACA0012 rotor was tested in hover to determine the variation of collective on the performance between the isolated and shrouded rotors. The rotor geometry is defined in Section 2.2. Of importance, the NACA0012 has a variable collective mechanism that is capable of testing $\theta_{75} = 5^\circ,\ 8^\circ,\ 11^\circ$, and 14°. The twist of the blade is linear with a slope of -14.125° and has a constant chord distribution.

Figure 4.7 shows thrust versus RPM for the isolated rotor and shrouded rotor cases of the NACA0012 rotor at all collectives tested. The shrouded rotor components T_{rotor} and T_{shroud} are also plotted to investigate the ratio of thrust between the rotor and shroud. For $\theta_{75} = 5^\circ,\ 8^\circ,\ 11^\circ$, and 14°, the shroud respectively accounts for 20%, 24%, 28%, and 31% of the total thrust of the shrouded rotor system. Thus, the shroud contribution increases with increasing collective. Thrust for $\theta_{75} = 5^\circ,\ 8^\circ$, and 11° was found to be similar to the isolated rotor. For the greatest collective tested of $\theta_{75} = 14^\circ$, the thrust was found to be 7% greater than the isolated rotor.

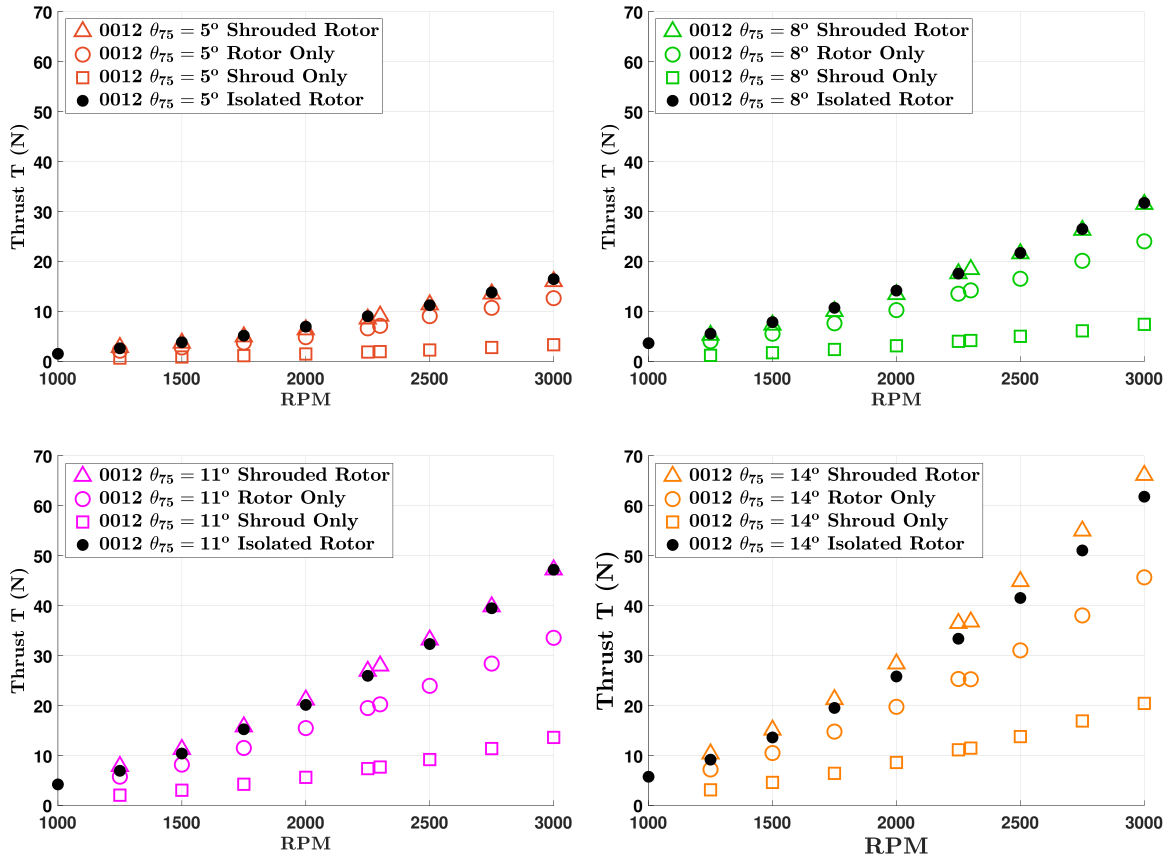

Figure 4.7: Thrust T versus RPM for shrouded and isolated NACA0012 rotor in hover.

Figure 4.8 shows power versus RPM for the isolated rotor and shrouded rotor cases of the NACA0012 rotor at all collectives tested. Power was found to reduce for all cases. For $\theta_{75} = 5°$, $8°$, $11°$, and $14°$, the respective power reduction from the isolated rotor was 16%, 15%, 11%, and 9%. Thus, the proportional power reduction decreased with increasing collective.

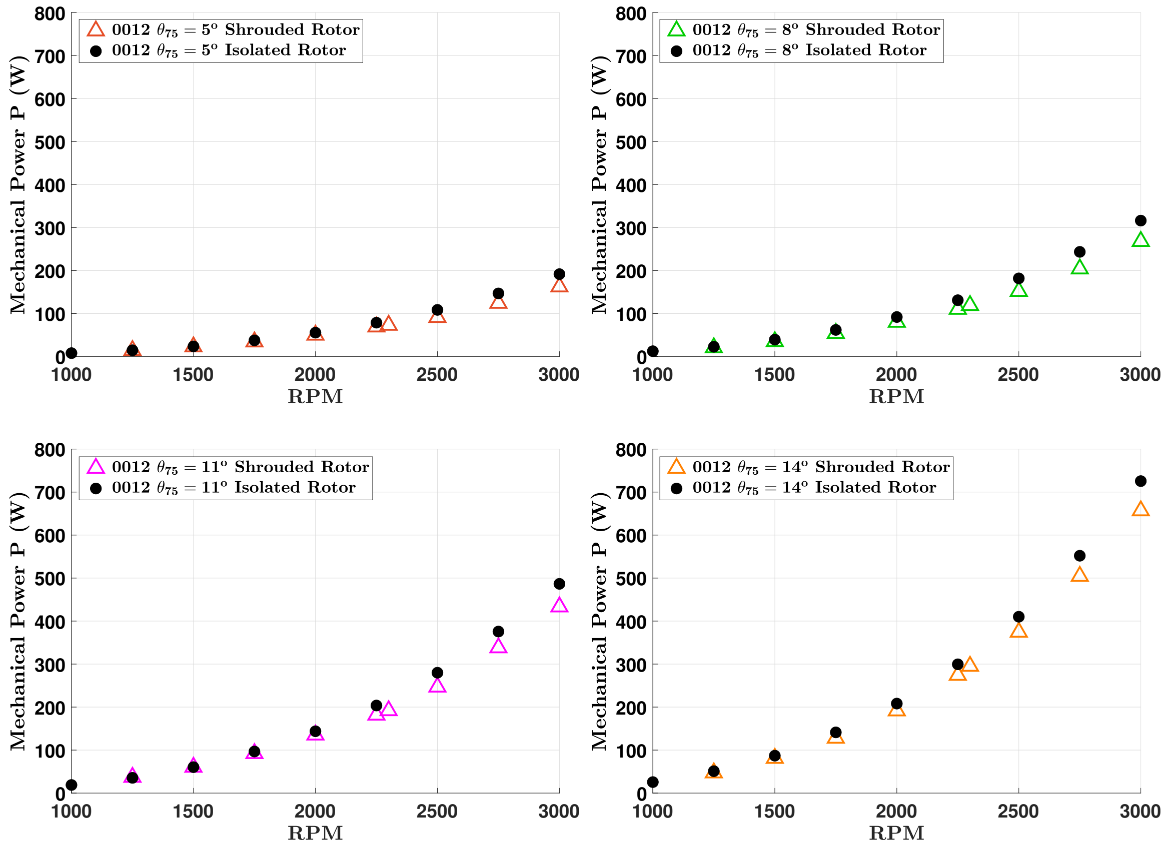

Figure 4.8: Mechanical power P versus RPM for shrouded and isolated NACA0012 rotor in hover.

Figure 4.9 shows the isolated and shrouded rotor thrust versus power curves. As expected from the previous thrust and power versus RPM figures, the shrouded rotor has increased thrust for the same power compared to the isolated rotor. Percentage gains were approximately 10% to 15%.

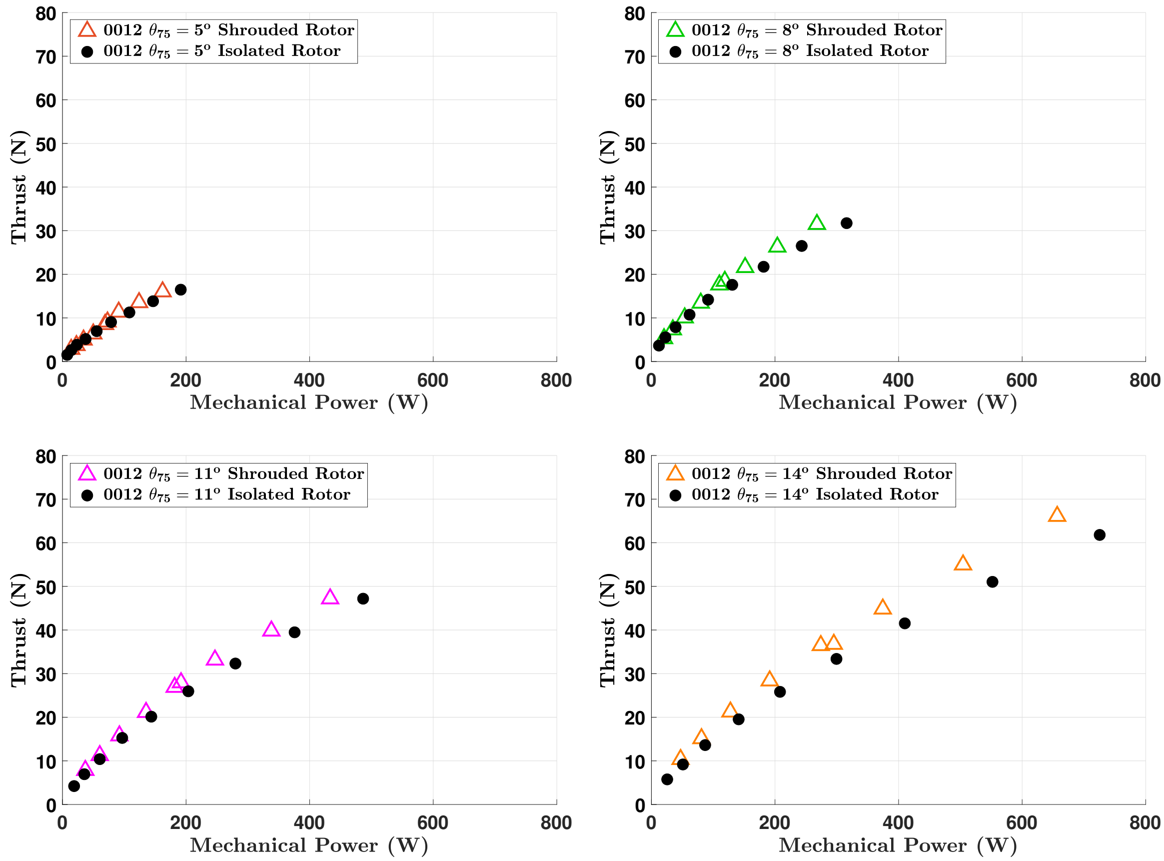

Figure 4.9: Thrust T versus mechanical power P for shrouded and isolated NACA0012 rotor in hover.

A power loading versus disk loading plot is shown in Figure 4.10. Again, performance improvement is seen with the shrouded rotor over the isolated rotor for all cases. For $\theta_{75} = 14^\circ$ and a disk loading of 4 kg/m^2, the power loading is 11% greater with the shrouded rotor compared to the isolated rotor.

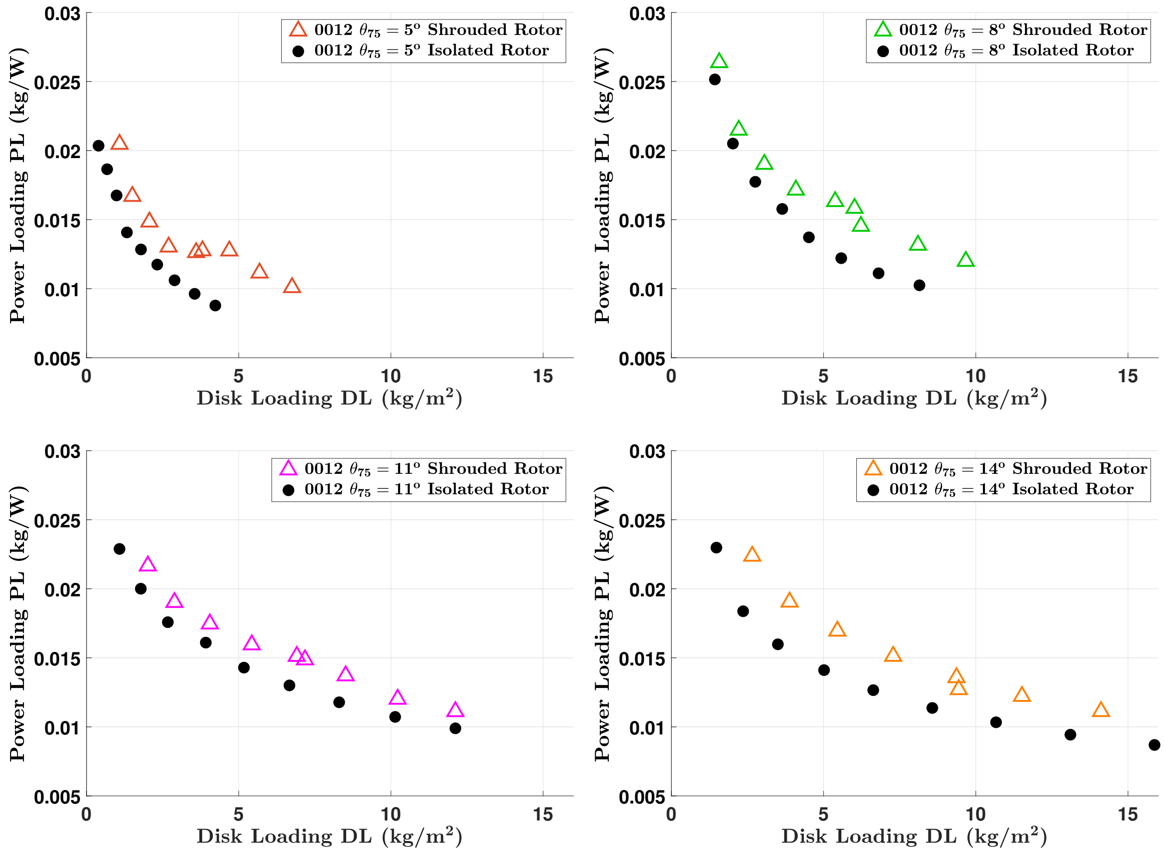

Figure 4.10: Power loading *PL* versus disk loading *DL* for shrouded and isolated NACA0012 rotor in hover.

4.1.3 T-motor and NACA0012 Rotor Comparison

To investigate the T-motor and NACAC0012 rotor performance differences, power loading for the shrouded rotor system and isolated rotor system are shown independently in Figures 4.11 and 4.12. The T-motor isolated rotor results are shown in comparison to both shrouded and isolated NACA0012 results to determine overall performance to the baseline isolated T-motor rotor.

Figure 4.11 shows shrouded rotor performance with the NACA0012 rotor compared to the isolated T-motor rotor. Among the shrouded rotor cases, the NACA0012 $\theta_{75} = 14^\circ$ performed with the greatest efficiency and the NACA0012 $\theta_{75} = 5^\circ$ performed with the worst efficiency. The T-motor isolated rotor performed worse than the shrouded NACA0012 $\theta_{75} = 11$, and 14° cases.

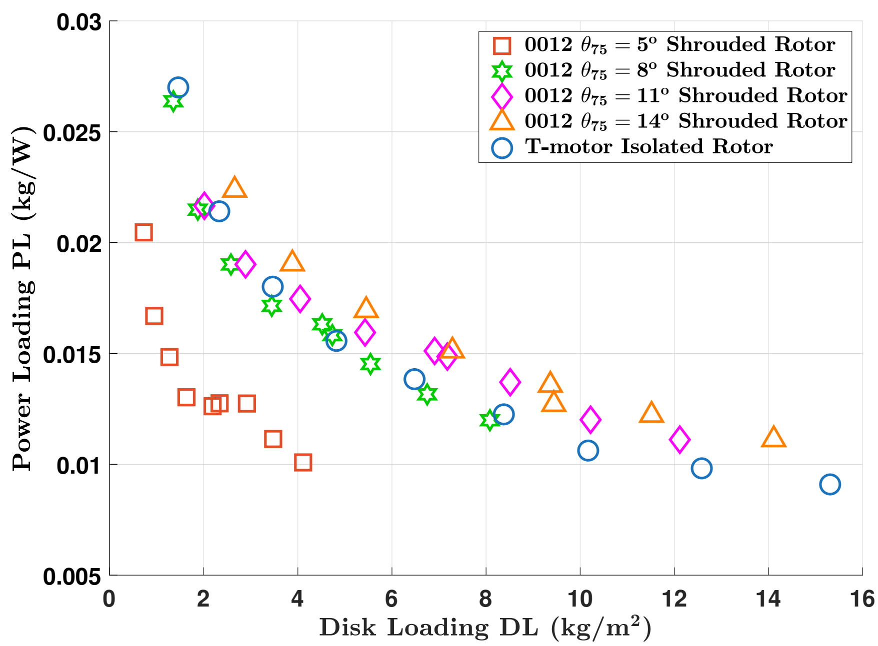

Figure 4.11: Power loading *PL* versus disk loading *DL* for shrouded NACA0012 rotor in hover.

For the isolated rotor cases, the T-motor rotor performed best across the range of disk loadings. The NACA0012 $\theta_{75} = 5^\circ$, 8°,and 11° followed similar power loading to disk loading trends while the shrouded rotor had greater separation between cases. Thus, these results indicate the shrouded rotor is most benefited when operating at greater collectives.

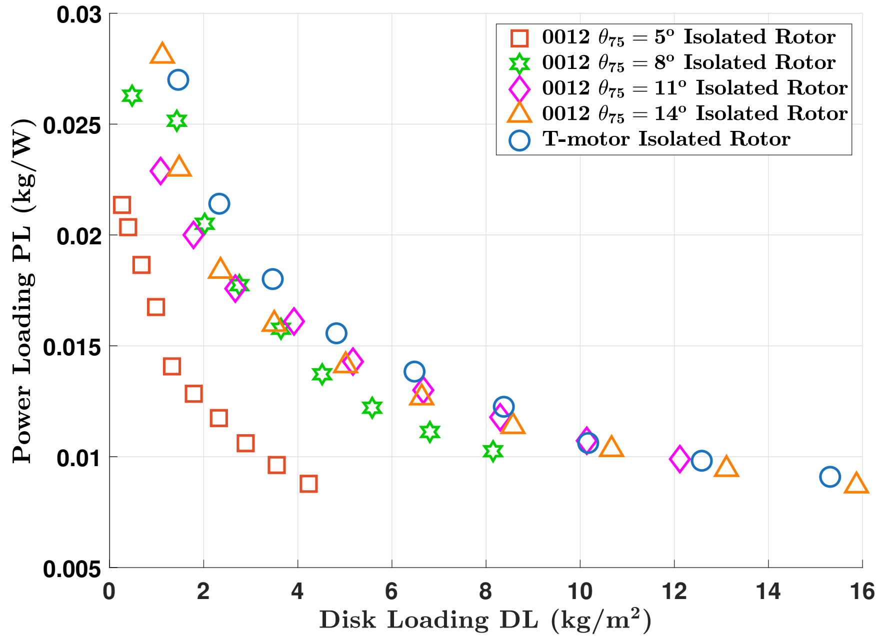

Figure 4.12: Power loading *PL* versus disk loading *DL* for isolated NACA0012 rotor in hover.

The best overall configuration tested was the NACA0012 $\theta_{75} = 14^\circ$ shrouded rotor. Interestingly, the same NACA0012 $\theta_{75} = 14^\circ$ rotor performed worse than other rotors tested in an isolated unshrouded configuration. Instead, the T-motor rotor performed best in an isolated rotor configuration. This suggests that with an optimized rotor and shroud design, an optimized isolated rotor will not reach the same level of efficiency as the optimized shrouded rotor. However, the same rotor from the optimized rotor and shroud design will not perform as well in an unshrouded configuration compared to an optimized isolated rotor. Thus, it is important to design an optimized coupled rotor and shroud system in order to maximize overall system performance.

4.2 Wind Tunnel Results

Wind tunnel tests were conducted up to a speed V of 5 m/s to investigate low speed forward flight shrouded rotor and isolated rotor performance differences. The T-motor rotor was used in these tests while the NACA0012 rotor was excluded. 2300, 3100 and 3900 RPM were the selected test RPMs investigated in the wind tunnel. These tests were conducted in edgewise flight ($\alpha = 0°$) and in climb ($\alpha = -15°$) as discussed in Section 4.2.1. Pure axial climb ($\alpha = -90°$) was also investigated and is discussed in Section 4.2.2. The wind tunnel coordinate frame is defined in Section 2.3.2.

4.2.1 Edgewise and Climb

Dimensional plots for the $V = 5$ m/s case are shown for edgewise flight in Figures 4.13 to 4.16. Comparing thrust in Figures 4.13 and 4.14, it is seen that the shrouded rotor system produces approximately 10% greater thrust for the same RPM compared to the isolated rotor in edgewise flight. In climb, for shaft tilt $\alpha_s = -15°$, the shrouded rotor and isolated rotor produce nearly equal total thrust. Comparing power in Figure 4.15, the shrouded rotor and isolated rotor are found to be nearly equal for both shaft tilt angles.

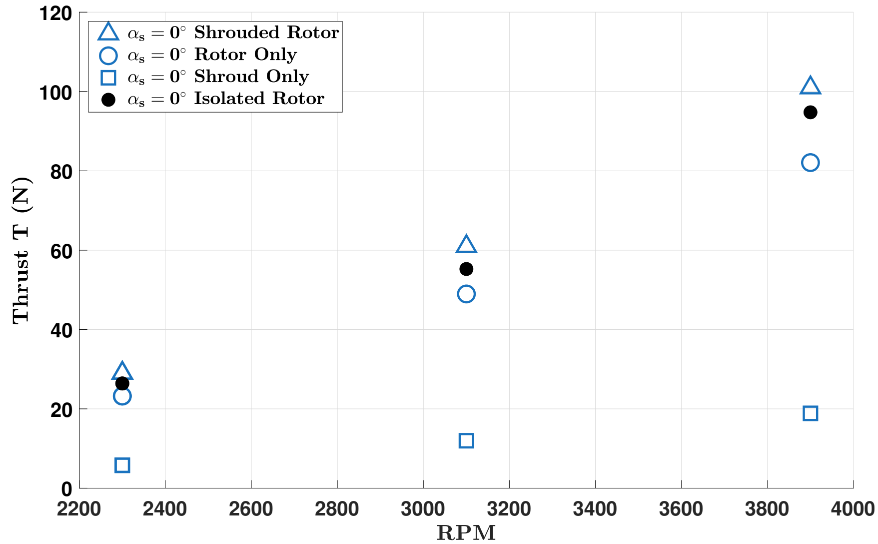

Figure 4.13: Thrust T versus RPM for shrouded and isolated T-motor rotor for edgewise $\alpha_s = 0°$ $V = 5$ m/s flight condition.

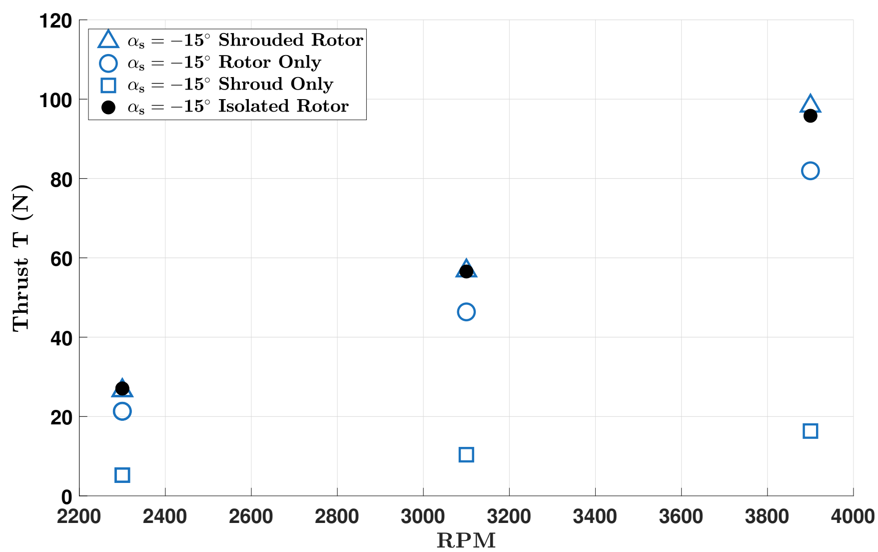

Figure 4.14: Thrust T versus RPM for shrouded and isolated T-motor rotor for climb $\alpha_s = -15°$ $V = 5$ m/s flight condition.

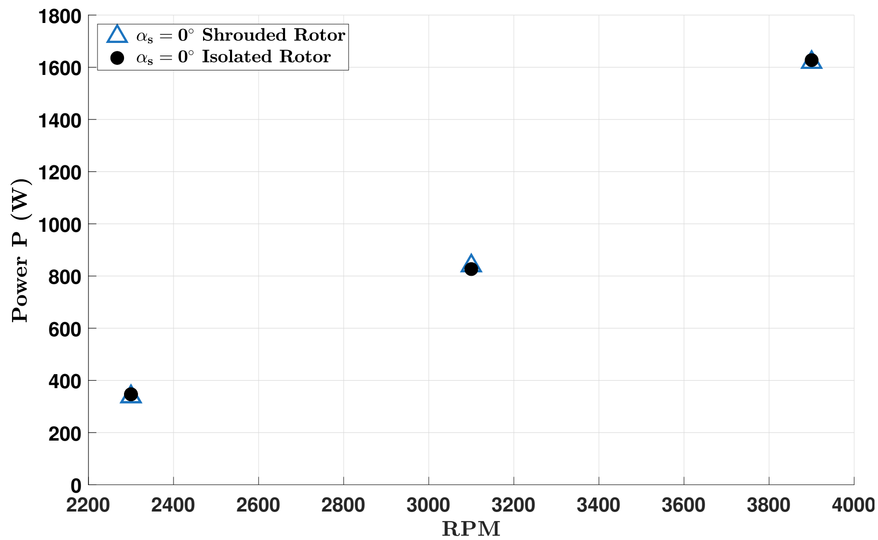

Figure 4.15: Power P versus RPM for shrouded and isolated T-motor rotor for edgewise $\alpha_s = 0°$ $V = 5$ m/s flight condition.

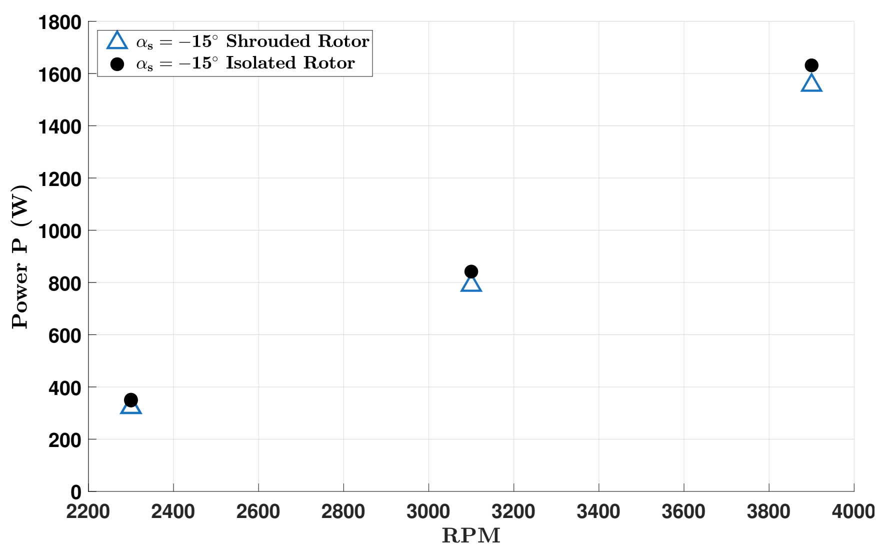

Figure 4.16: Power P versus RPM for shrouded and isolated T-motor rotor for climb $\alpha_s = -15°$ $V = 5$ m/s flight condition.

Advance ratio is a metric used to measure the ratio of forward velocity to rotor tip speed. Advance ratio is defined as follows:

$$\mu = \frac{V cos \alpha_s}{\Omega R} \tag{4.4}$$

Figures 4.17 and 4.18 show C_T/σ versus μ for the shrouded rotor system and isolated rotor. A hover case for 2300 RPM is shown as $\mu = 0$ for comparison. For increasing advance ratio, the value for C_T/σ reduces. Comparing the isolated and shrouded rotor, the shrouded rotor provides additional thrust for $\alpha_s = 0°$ that is approximately 10% greater than the isolated rotor case. For $\alpha_s = -15°$, this advantage is reduced and the shrouded rotor performs similarly to the isolated rotor. It is assumed that because the wind speed is low, the value for C_T/σ does not decrease noticeably in climb.

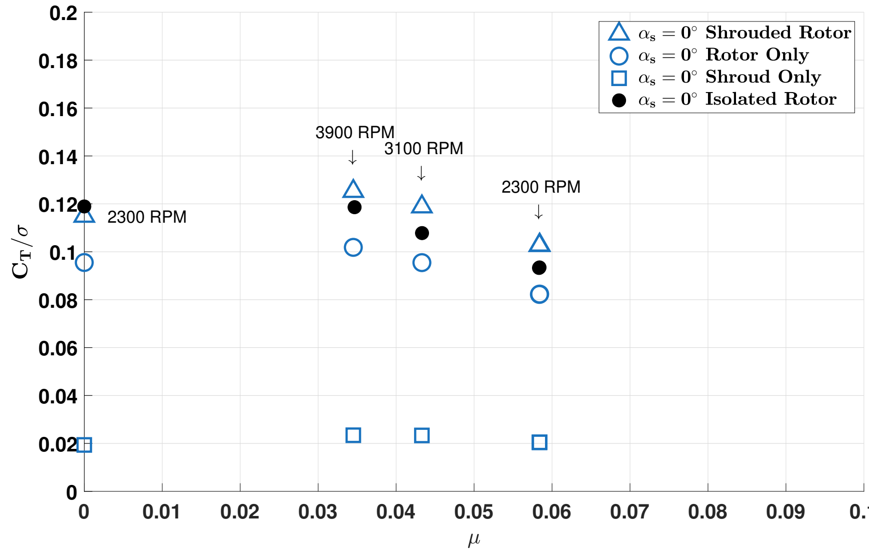

Figure 4.17: Coefficient of thrust C_T versus advance ratio μ for shrouded and isolated rotor at $\alpha_s = 0°$ edgewise condition.

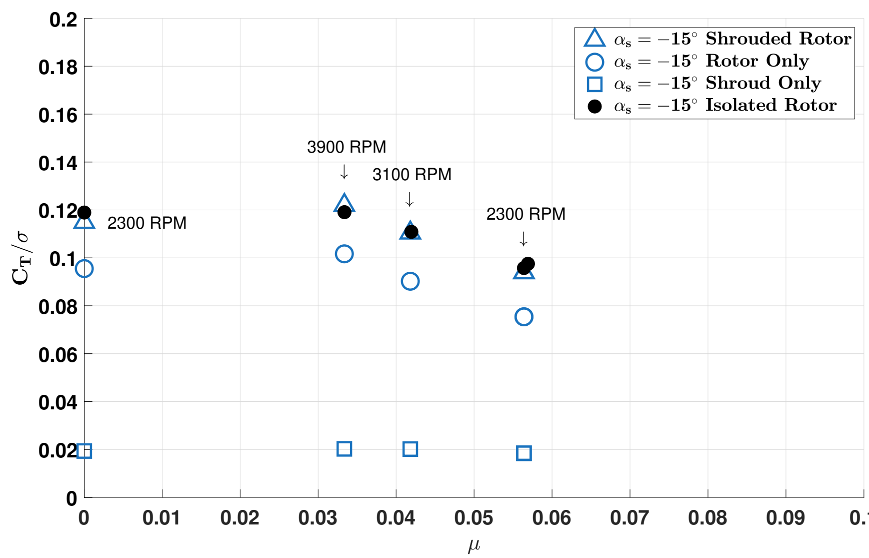

Figure 4.18: Coefficient of thrust C_T versus advance ratio μ for shrouded and isolated rotor at $\alpha_s = -15°$ climb condition.

Figures 4.19 and 4.20 show C_P/σ versus μ for the shrouded rotor system and isolated rotor. Again, a hover case for 2300 RPM is shown as $\mu = 0$ for comparison. The value for C_P/σ remains nearly constant for edgewise flight. For $\alpha_s = -15°$, the power required by the shrouded rotor is reduced by approximately 10% compared to the isolated rotor. Compared to the 2300 RPM hover case, the value for C_P/σ is greater for all cases.

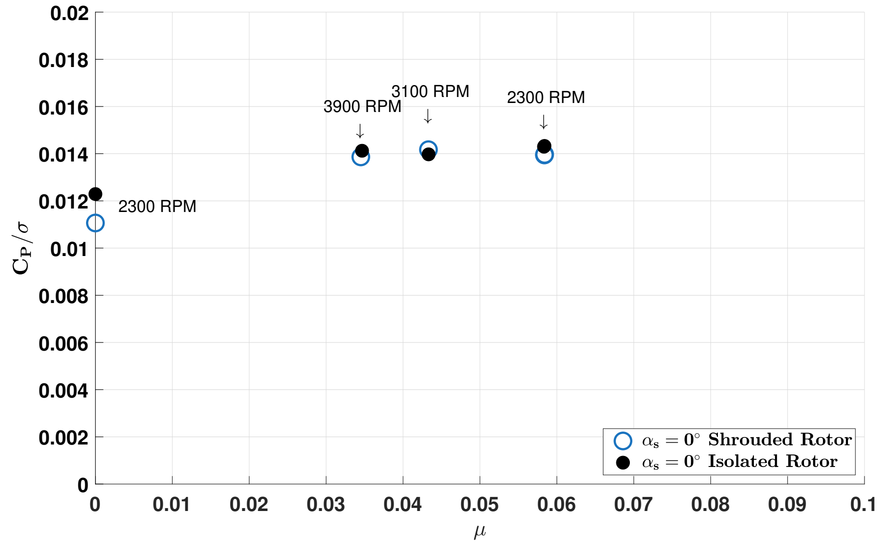

Figure 4.19: Coefficient of power C_P versus advance ratio μ for shrouded and isolated rotor at $\alpha_s = 0°$ edgewise condition.

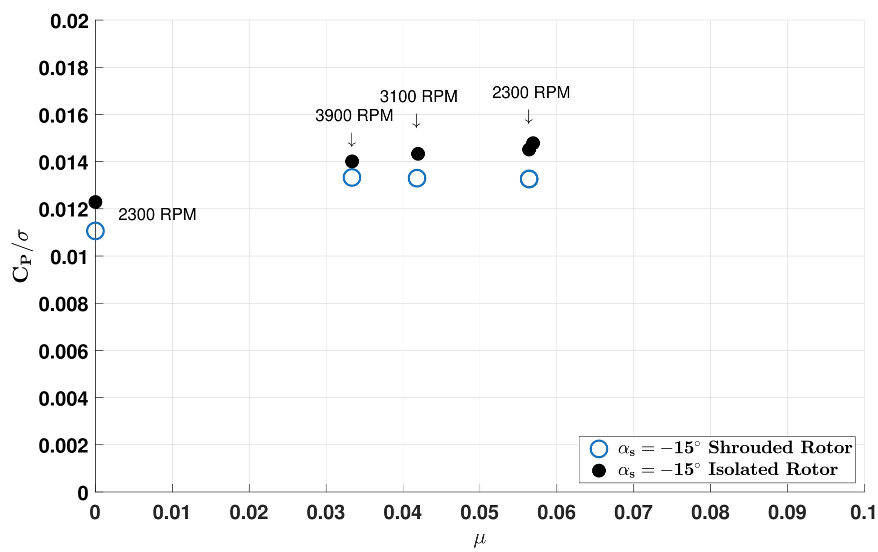

Figure 4.20: Coefficient of power C_P versus advance ratio μ for shrouded and isolated rotor at $\alpha_s = -15°$ climb condition.

Figures 4.21 and 4.22 show roll moment versus advance ratio. Comparing $\alpha_s = 0°$ edgewise and $\alpha_s = -15°$ climb, the roll moment for the isolated rotor decreases with increasing shaft tilt. For the shrouded rotor, the roll moment increases with increasing shaft tilt. Thus, the shrouded rotor is likely greater affected by flow asymmetry.

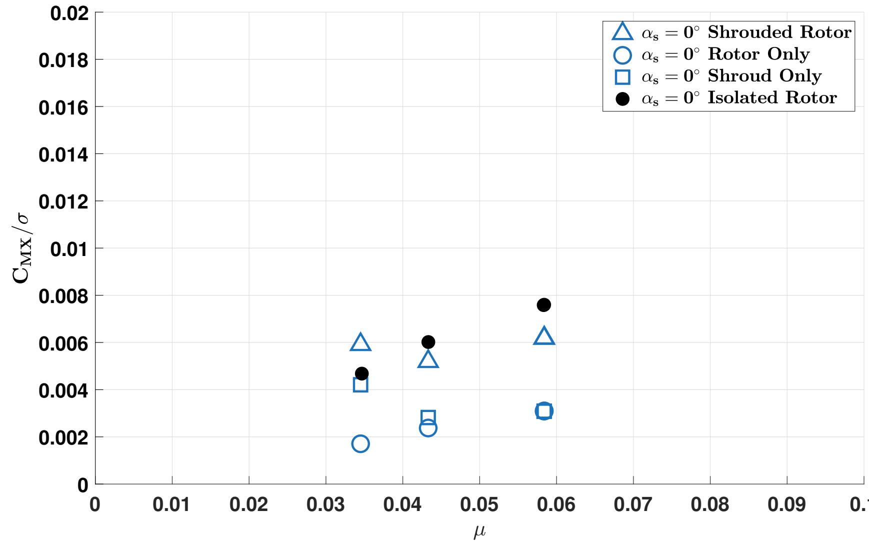

Figure 4.21: Roll moment coefficient C_{MX} at the hub versus advance ratio μ for shrouded and isolated rotor at $\alpha_s = 0^\circ$ edgewise condition.

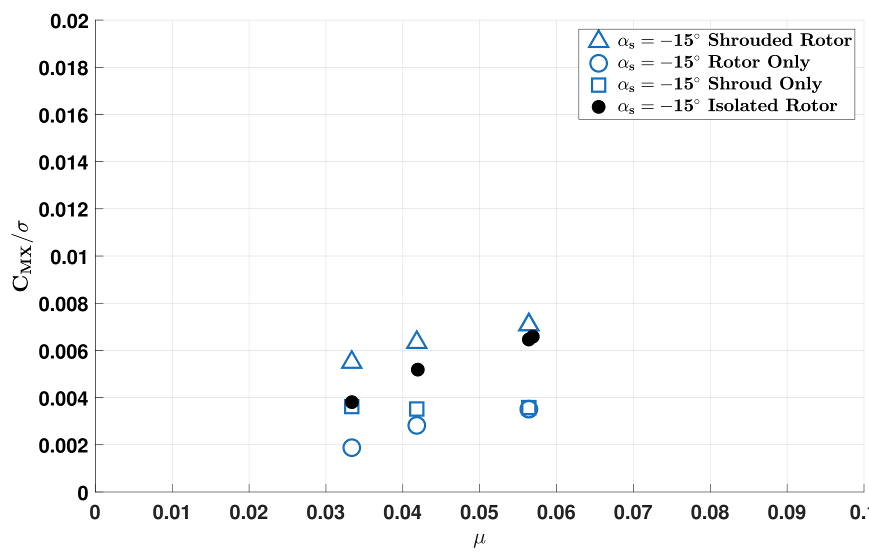

Figure 4.22: Roll moment coefficient C_{MX} at the hub versus advance ratio μ for shrouded and isolated rotor at $\alpha_s = -15^\circ$ climb condition.

Figures 4.23 and 4.24 show pitching moment versus advance ratio. Pitching moment for both $\alpha_s = 0°$ edgewise and $\alpha_s = -15°$ climb is found to increase with increasing advance ratio and is 150% greater for the shrouded rotor system compared to the isolated rotor. For both shaft tilts, the shroud produces approximately 65 to 70% of the total pitching moment of the shrouded rotor system while the rotor component pitching moment is approximately equal to the isolated rotor. For $\alpha_s = -15°$, the pitching moment for all components is reduced compared to pure edgewise flight.

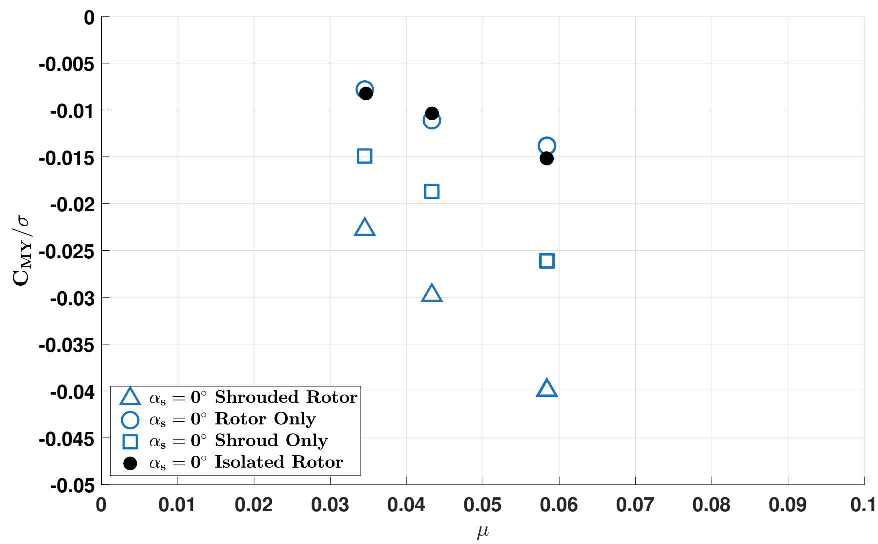

Figure 4.23: Pitch moment coefficient C_{MY} at the hub versus advance ratio μ for shrouded and isolated rotor at $\alpha_s = 0°$ edgewise condition.

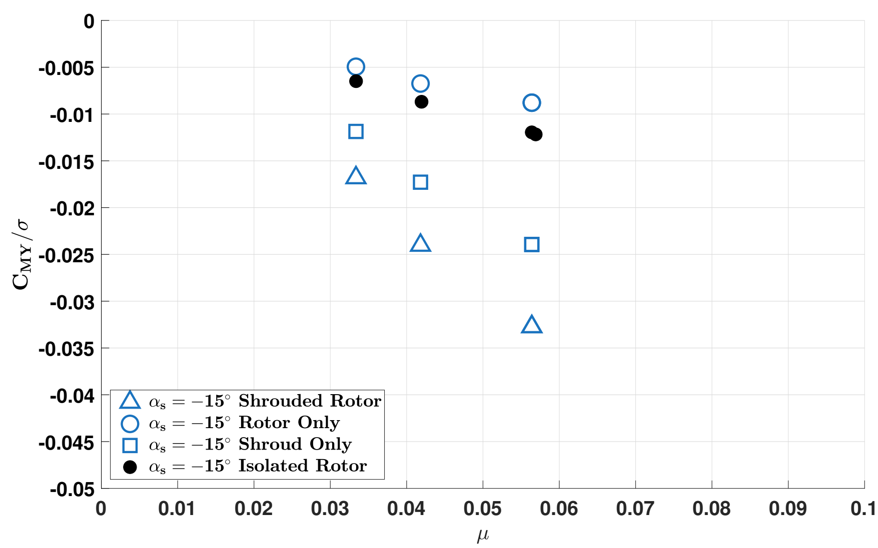

Figure 4.24: Pitch moment coefficient C_{MY} at the hub versus advance ratio μ for shrouded and isolated rotor at $\alpha_s = -15°$ climb condition.

The isolated rotor and shrouded rotor effective lift-to-drag ratio is a key parameter to characterize the performance in forward flight. The isolated rotor lift-to-drag ratio L/D_e is defined by:

$$\frac{L}{D_e} = \frac{L}{D + \frac{P}{V}} \tag{4.5}$$

With shaft tilt angle α_s, the equation becomes:

$$\frac{L}{D_e} = \frac{T cos\alpha_s - H sin\alpha_s}{T sin\alpha_s + H cos\alpha_s + \frac{P}{V}} \tag{4.6}$$

In this case, it is important to note the lift and drag terms are only from the rotor for the shrouded rotor. The shrouded rotor lift-to-drag ratio L/D_e is defined by:

$$\frac{L}{D}_{e\,Shrouded\ Rotor:\ Rotor\ Only} = \frac{L_{rotor}}{D_{rotor} + \frac{P_{rotor}}{V}} \tag{4.7}$$

With shaft tilt angle α_s, the equation becomes:

$$\frac{L}{D}_{e\,Shrouded\ Rotor:\ Rotor\ Only} = \frac{T_{rotor} cos\alpha_s - H_{rotor} sin\alpha_s}{T_{rotor} sin\alpha_s + H_{rotor} cos\alpha_s + \frac{P_{rotor}}{V}} \tag{4.8}$$

The effective lift-to-drag ratio versus advance ratio is shown in Figure 4.25 and 4.26. Both figures show increasing L/D_e with increasing advance ratio. The isolated rotor produces 13% greater L/D_e compared to the shrouded rotor in these cases. With the inclusion of the shroud, the shrouded rotor system performs similarly to the isolated rotor in edgewise flight but results in an 8 to 10% increase in L/D with a shaft tilt of $\alpha_s = -15°$. Thus, the inclusion of the shroud results in a marginally more efficient system compared to the isolated rotor in low speed forward flight.

Only the rotor lift and drag components are considered in Equations 4.7 and 4.8 while the shroud lift and drag components are excluded. This is similar in methodology to a wing and rotor compound rotorcraft as described by Bauknecht et al. [32]. As a total system, the shrouded rotor shroud component should also be considered. Thus, the effective lift-to-drag ratio of the shrouded rotor system is defined by:

$$\frac{L}{D_e}_{Shrouded\ Rotor} = \frac{L_{shroud} + L_{rotor}}{D_{shroud} + D_{rotor} + \frac{P_{rotor}}{V}} \tag{4.9}$$

With shaft tilt angle α_s, the equation becomes:

$$\frac{L}{D_e}_{Shrouded\ Rotor} = \frac{T_{shroud} cos\alpha_s - H_{shroud} sin\alpha_s + T_{rotor} cos\alpha_s - H_{rotor} sin\alpha_s}{T_{shroud} sin\alpha_s + H_{shroud} cos\alpha_s + T_{rotor} sin\alpha_s + H_{rotor} cos\alpha_s + \frac{P_{rotor}}{V}} \tag{4.10}$$

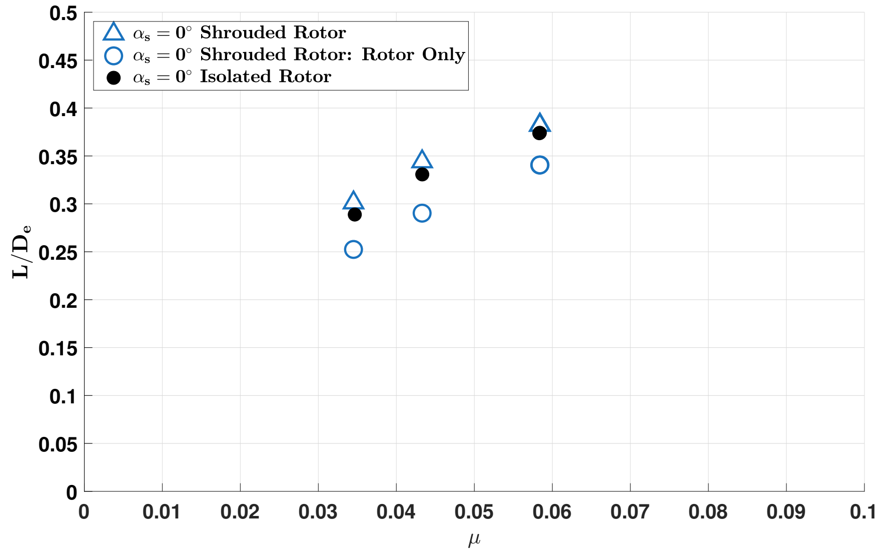

Figure 4.25: Effective lift-to-drag ratio L/D_e versus advance ratio μ for shrouded and isolated rotor at $\alpha_s = 0^\circ$ edgewise condition.

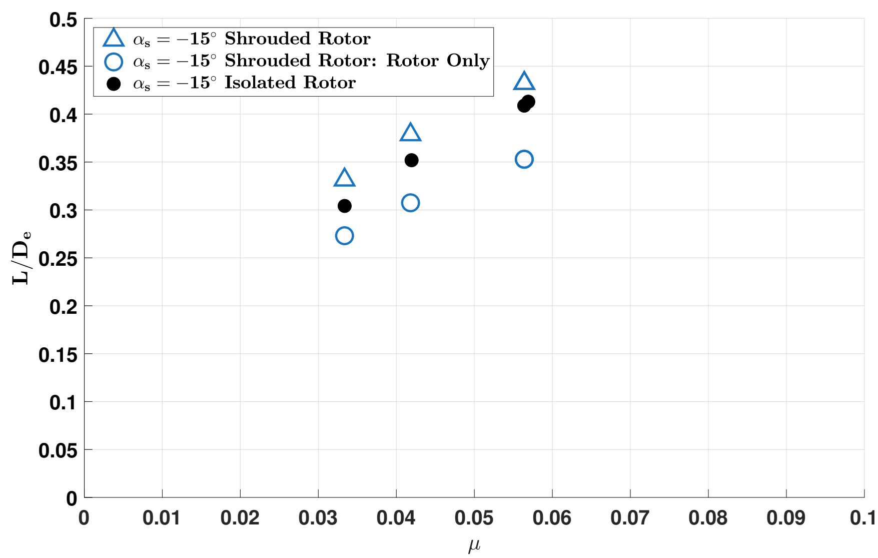

Figure 4.26: Effective lift-to-drag ratio L/D_e versus advance ratio μ for shrouded and isolated rotor at $\alpha_s = -15^\circ$ climb condition.

4.2.2 Axial Climb

Pure axial climb ($\alpha = -90^\circ$) tests were completed to investigate the climb performance of the isolated rotor and shrouded rotor. The metric used for climb inflow is defined by:

$$\lambda_c = \frac{V_\infty}{\Omega R} \tag{4.11}$$

Figure 4.27 shows coefficient of thrust C_T/σ for the total shrouded rotor, shrouded rotor components, and isolated rotor. In climb, the isolated rotor performs similarly to the shrouded rotor. Compared to the 2300 RPM hover case, thrust decreases with climb velocity. The shroud in the shrouded rotor system begins with positive C_T/σ and decreases with increasing climb inflow until it becomes negative due to drag. However, the shrouded rotor system begins with lower C_T/σ than the isolated rotor and increases relative to the isolated rotor with increasing λ_c until it becomes equivalent to the isolated rotor.

Figure 4.28 shows power coefficient C_P/σ versus climb inflow λ_c. C_P/σ for the shrouded rotor follows a similar trend to the isolated rotor and is consistently marginally lower than the isolated rotor. This is a similar finding to the hover results.

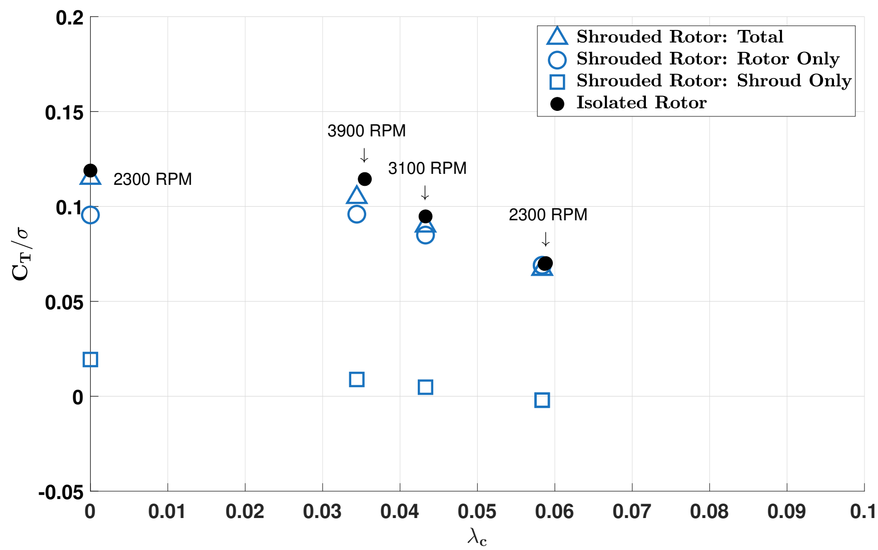

Figure 4.27: Coefficient of thrust (propulsive force) C_T versus climb inflow λ_c for shrouded and isolated rotor at $\alpha_s = -90°$ axial climb condition.

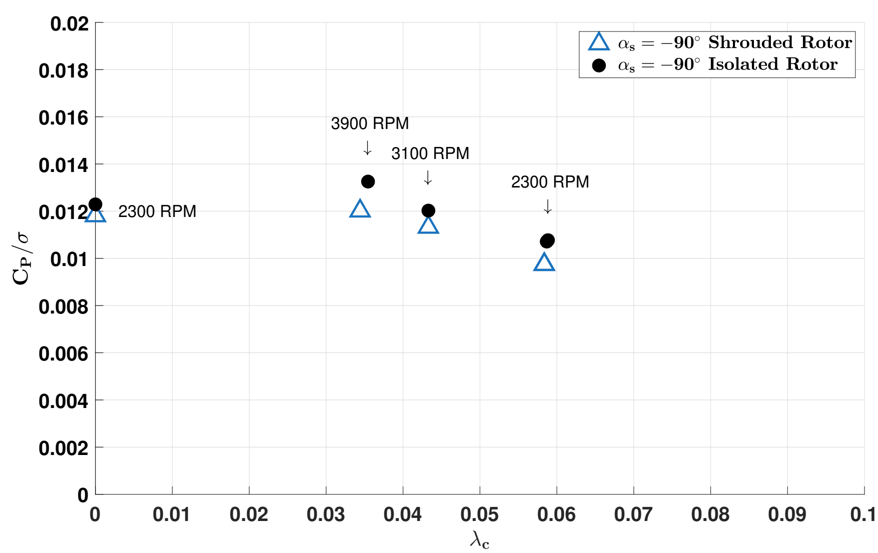

Figure 4.28: Coefficient of power C_P versus climb inflow λ_c for shrouded and isolated rotor at $\alpha_s = -90°$ axial climb condition.

To quantify pure axial climb efficiency, propeller efficiency η is used. The propulsive force X which is used to find η is defined by:

$$X_{Isolated\ Rotor} = T_{Isolated\ Rotor} \tag{4.12}$$

$$X_{Shrouded\ Rotor} = T_{Shrouded\ Rotor} \tag{4.13}$$

Propulsive efficiency is then defined by:

$$\eta_{Isolated\ Rotor} = \frac{X_{Isolated\ Rotor}V}{P_{Isolated\ Rotor}} \tag{4.14}$$

$$\eta_{Shrouded\ Rotor} = \frac{X_{Shrouded\ Rotor}V}{P_{Shrouded\ Rotor}} \tag{4.15}$$

Figure 4.29 shows propulsive efficiency versus climb inflow. With increasing climb inflow, the shrouded rotor and isolated rotor increase in propulsive efficiency and are nearly equivalent.

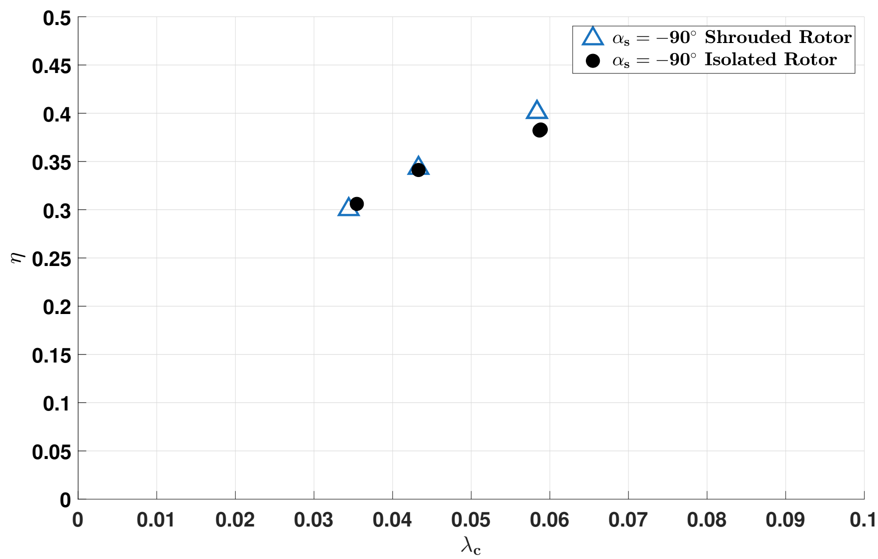

Figure 4.29: Efficiency η versus climb inflow λ_c for shrouded and isolated rotor at $\alpha_s = -90°$ axial climb condition.

4.3 Chapter Summary

The isolated rotor and shrouded rotor performance for hover and low speed wind tunnel conditions was characterized. With the T-motor rotor in hover, it was found that the shrouded rotor performed similarly to the isolated rotor with matching thrust and power. The shroud attributed 20% and the rotor 80% of the total thrust generated by the shrouded rotor system. However, shrouded and isolated hover performance was similar for the T-motor rotor with minimal efficiency gains. In contrast, performance benefits were observed with the NACA0012 rotor: Power reduced by 10% to 16% and thrust increased up to 7% for the collectives tested with the shrouded system over the isolated rotor. Power loading for all NACA0012 rotor cases increased with the shrouded rotor system. The best overall configuration tested was the NACA0012 $\theta_{75} = 14^\circ$ shrouded rotor. These results prove it is important to design both the rotor and shroud as a coupled system in order to maximize overall performance.

For low speed wind tunnel tests, the T-motor rotor and shroud system was characterized. For $\alpha_s = 0^\circ$ edgewise flight, approximately 10% greater thrust and equivalent power was observed with the shrouded rotor system compared to the isolated rotor. For $\alpha_s = -15^\circ$ forward flight climb, the thrust for both configurations was equivalent while the power was approximately 10% less for the shrouded rotor compared to the isolated rotor. Pitch moment was observed to be approximately 150% greater for the shrouded rotor system compared to the isolated rotor. Lift-to-drag ratio L/D_e was found to increase by 8 to 10% for the shrouded rotor system for $\alpha_s = -15^\circ$ over the isolated rotor. In axial climb, the shrouded rotor yielded similar propulsive efficiency to the isolated rotor.

Chapter 5: Conclusions

5.0.1 Summary of Research

This thesis focused on the hover and wind tunnel performance of an electric medium-sized variable-RPM rotor and shrouded rotor.

First, an experimental test rig is designed, fabricated and validated for testing with a range of test articles. Many of these test articles were custom designed and fabricated for testing in both hover and wind tunnel conditions.

Second, Blade element momentum theory (BEMT) with two Reynolds number correction approaches is explained and compared with experimental hover results. Transient step and chirp input results are presented with Comprehensive Identifica- tion from Frequency Response (CIFER) analysis which can be used to validate and inform physics based multi-rotor modeling.

Lastly, experimental comparison of a shrouded and isolated rotor in hover and low speed wind tunnel conditions is provided and discussed. Helios CFD results are compared for static and climb conditions.

5.0.2 Conclusions

1. The universal test stand as constructed is proven for hover and wind tunnel tests in the Glenn L. Martin Wind Tunnel with a variety of test articles.

2. Load cell measurement reading drift is shown to be due to the BLDC electric motor heat and is minimized with G-10 insulation.

3. The 28 inch diameter NACA0012 rotor constructed with a single root insert and no spar was demonstrated successfully for rotational speeds up to 3000 RPM.

4. The 3D printed shroud resulted in minimal deflection and is proven for hover and low speed wind tunnel testing with uncoupled shroud and rotor load measurement.

5. The TRV-80 bare airframe test rig is proven for low-speed wind tunnel tests.

6. Correlation of experimental and predicted thrust and power results show dependence on Reynolds number variation along the span and with RPM for the 28 inch diameter rotors tested. The empirical method showed good agreement with experimental results for high RPM and less satisfactory agreement for low RPM. The interpolation method which uses multiple airfoil tables generated at different Reynolds number showed better agreement, indicating strong dependence on accuracy of C_l and C_d data.

7. System identification results indicate a constant relationship between thrust with RPM and RPM^2. Therefore, when modeling this rotor, steady inflow appears ad-

equate in the frequency range of interest. Linear frequency responses of RPM and RPM^2 to torque were also found.

8. Similar results for C_T and C_Q were calculated from both hover and transient data.

9. Torque's frequency responses were used to derive the moment of inertia from the transient data which was within 15% to the moment of inertia found from SolidWorks.

10. Electrical efficiency of the ESC and motor system peaks at 90% above 2000 RPM and has significantly reduced efficiency below 2000 RPM.

11. For all rotors tested, the shroud contributed approximately 20% to 30% of the total thrust of the shrouded rotor system.

12. With the T-motor rotor in hover, the shrouded rotor performance was similar to the isolated rotor with no net gain or loss in efficiency.

13. With the NACA0012 rotor in hover, the shrouded rotor performance was improved compared to the isolated rotor, with up to 11% greater power loading for the same disk loading. For the same RPM, thrust was found to increase by up to 7% and power reduced by 9% to 16%.

14. Increasing collective with the NACA0012 rotor in hover yielded greater efficiency gains compared to lower collectives for the shrouded rotor system.

15. In low speed edgewise flight $\alpha_s = 0^\circ$, the T-motor shrouded rotor produced approximately 10% greater thrust with equivalent power draw compared to the isolated rotor.

16. In low speed climb flight $\alpha_s = -15^\circ$, the T-motor shrouded rotor produced approximately equivalent thrust with approximately 10% power draw reduction compared to the isolated rotor.

17. In low speed flight, the shroud produced an approximately 150% greater pitching moment than the isolated rotor with the majority of the pitching moment produced by the shroud.

18. For low speed flight at $\alpha_s = -15^\circ$, the lift-to-drag ratio L/D_e for the T-motor shrouded rotor was found to increase by 8 to 10% for the shrouded rotor system.

19. In low speed axial climb, the T-motor shrouded rotor yielded similar propulsive efficiency to the isolated rotor.

5.0.3 Future Work

There are many areas where this work can be expanded to improve the design and analysis of UAVs, some of these opportunities are listed below:

1. **Shrouded Rotor:** Greater collectives should be tested with the NACA0012 and T-motor rotor as greater efficiency gains are likely to be found. High speed wind tunnel tests should be performed to investigate advance ratios up to at least 0.25 in order to fully characterize the operating range of the system. Due to the current inoperability

of the Glenn L. Martin Wind Tunnel, these tests could not be conducted but are scheduled for the near future.

2. **Aerodynamic Interactions:** Interactions of the variable-RPM rotor with other rotors or stationary objects such as vehicle frame structural components should be collected to fully characterize the TRV-80 vehicle performance. With bare airframe drag and isolated rotor loads, the next step is to test co-axial counter-rotating rotors and the full vehicle with all 4 counter-rotating rotors. Component addition of loads will then reveal interaction effects.

3. **Transient Rotor System Identification:** Further tests should be completed to characterize the difference between variable RPM and variable collective as the vehicle scales. Increased rotor size will affect RPM response due to increased inertia and required vehicle maneuverability will change with scale. In addition, system identification with input PWM commands should be modeled for control purposes with a physics based model. Lastly, transient tests should be conducted in the wind tunnel to determine whether forward flight conditions will have an effect on dynamic RPM response.

Appendix A: TRV-80 Bare Airframe Low Speed Wind Tunnel Results

Low speed wind tunnel tests were performed with the TRV-80 bare airframe. The purpose of these tests was to determine the dimensional drag and drag factor of the airframe without rotors. As described in Section 2.2.3, the airframe has the ability to be tested with varying body pitch angles and yaw angles. With an airspeed of 6.5 m/s, the bare airframe was tested at yaw angles of 0°, 45°, and 90° with results shown in Figure A.1. The equation for drag factor is defined by:

$$f = \frac{D}{\frac{1}{2}\rho V_\infty^2} \tag{A.1}$$

The drag factor is lowest for edgewise flight at a body angle $\alpha = 0^\circ$ and greatest in climb and descent at $\alpha = -90^\circ$ and 90°.

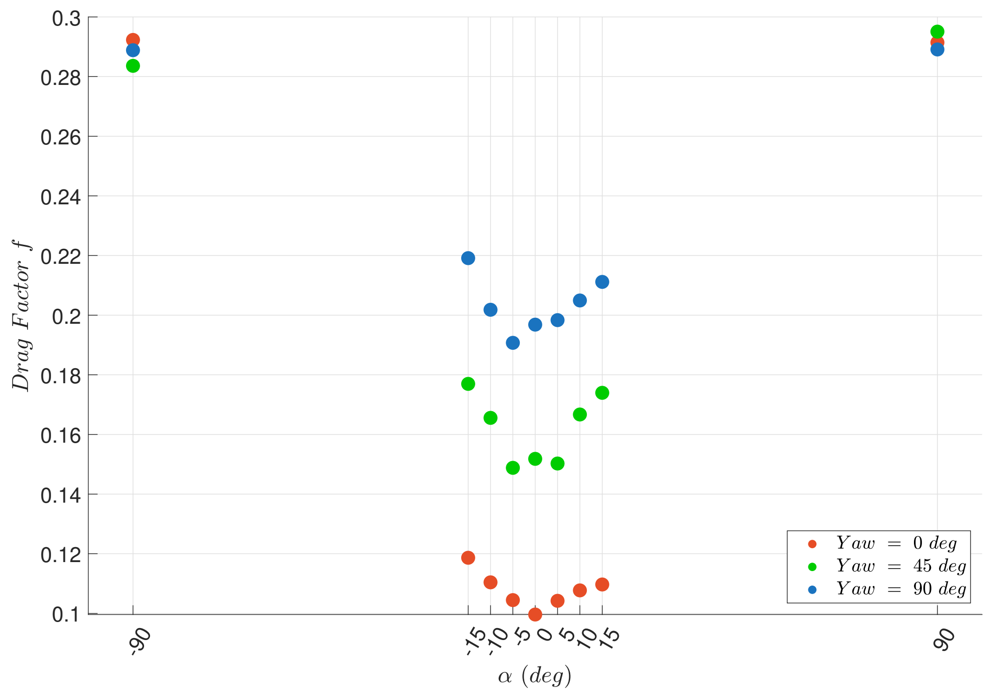

Figure A.1: Drag factor f vs. body pitch angle α_s for TRV-80 bare airframe (no rotors).

Bibliography

[1] R. Kumar. Tactical reconnaissance: Uavs versus manned aircraft. Technical report, Air Command and Staff Coll Maxwell AFB AL, 1997.

[2] S. G. Penny, R. L. White, D. M. Scott, L. MacTavish, and A. P. Pernetta. Using drones and sirens to elicit avoidance behaviour in white rhinoceros as an anti-poaching tactic. *Proceedings of the Royal Society B*, 286(1907):20191135, 2019.

[3] S. P. Yeong, L. M. King, and S. S. Dol. A review on marine search and rescue operations using unmanned aerial vehicles. *International Journal of Marine and Environmental Sciences*, 9(2):396–399, 2015.

[4] V. Sherstjuk, M. Zharikova, and I. Sokol. Forest fire-fighting monitoring system based on uav team and remote sensing. In *2018 IEEE 38th International Conference on Electronics and Nanotechnology (ELNANO)*, pages 663–668, 2018.

[5] Tactical Resupply Vehicle (TRV). SURVICE Engineering,www.survice.com/who-we-are/focus-areas/tactical-resupply-vehicle-trv.

[6] B. Phillips, V. Hrishikeshavan, D. Yeo, and I. Chopra. Experimental evaluation of a quadrotor biplane with variable pitch rotors. In *73rd Annual Forum of the American Helicopter Society*, 2017.

[7] M. E. McKay, R. Niemiec, and F. Gandhi. Performance comparison of quadcopters with variable-rpm and variable-pitch rotors. *Journal of the American Helicopter Society*, 64(4):1–14, 2019.

[8] A. Walter, M. McKay, R. Niemiec, F. Gandhi, and C. Jaran. An assessment of heave response dynamics for electrically driven rotors of increasing diameter. In *8th Biennial Autonomous VTOL Technical Meeting and 6th Annual Electric VTOL Symposium, Mesa, AZ, USA*, 2019.

[9] Sky. Royal marines seek 'battlefield advantage' as they train with drone swarms in uk first, Jul 2021.

[10] B. Theys, G. Dimitriadis, T. Andrianne, P. Hendrick, and J. De Schutter. Wind tunnel testing of a vtol mav propeller in tilted operating mode. In *2014 International conference on unmanned aircraft systems (ICUAS)*, pages 1064–1072. IEEE, 2014.

[11] A. Kolaei, D. Barcelos, and G. Bramesfeld. Experimental analysis of a small-scale rotor at various inflow angles. *International Journal of Aerospace Engineering*, 2018, 2018.

[12] C. R. Russell, J. Jung, G. Willink, and B. Glasner. Wind tunnel and hover performance test results for multicopter uas vehicles. In *American Helicopter Society (AHS) International Annual Forum and Technology Display*, 2016.

[13] R. W. Deters, A. Krishnan, G. Kumar, and M. S. Selig. Reynolds number effects on the performance of small-scale propellers. In *32nd AIAA applied aerodynamics conference*, page 2151, 2014.

[14] J. Winslow, . Benedict, V. Hrishikeshavan, and I. Chopra. Design, development, and flight testing of a high endurance micro quadrotor helicopter. *International Journal of Micro Air Vehicles*, 8(3):155–169, 2016.

[15] BELL NEXUS, https://www.bellflight.com/products/bell-nexus.

[16] J. L. Pereira. *Hover and wind-tunnel testing of shrouded rotors for improved micro air vehicle design*. University of Maryland, College Park, 2008.

[17] CREATE Air Vehicles (AV). DEPARTMENT OF DEFENSE HIGH PERFORMANCE COMPUTING MODERNIZATION PROGRAM, www.hpc.mil/program-areas/computational-research-and-engineering-acquisition-tools-and-environments/create-air-vehicles-av.

[18] F. Chew, S. Gan, and H. Hesse. Rapid design process of shrouded rotors for efficient uav propulsion. In *AIAA Scitech 2021 Forum*, page 0212, 2021.

[19] V. Hrishikeshavan and I. Chopra. Performance, flight testing of a shrouded rotor micro air vehicle in edgewise gusts. *Journal of Aircraft*, 49(1):193–205, 2012.

[20] Glenn L. Martin Wind Tunnel. Facilities, University of Maryland, windtunnel.umd.edu/facilities.

[21] J. B. Barlow, W. H. Rae, and A. Pope. *Low-speed wind tunnel testing*. John wiley & sons, 1999.

[22] F/T Sensor: Mini45. ATI Industrial Automation, https://www.ati-ia.com/products/ft/ft_models.aspx?id=mini45.

[23] 48 Volt 210 Amp 10,080 Watt AC-to-DC Enclosed Single Output Switching Power Supply. Jameco Electronics, https://www.jameco.com/z/RST-10000-48-MEAN-WELL-48-Volt-210-Amp-10-080-Watt-AC-to-DC-Enclosed-Single-Output-Switching-Power-Supply_2220568.html.

[24] T. W. Haag. Thrust stand for high-power electric propulsion devices. *Review of Scientific Instruments*, 62(5):1186–1191, 1991.

[25] T. Narbuntas, S. Conley, K. Kallstrom, and A. Abrego. Wind tunnel performance test of a ducted fan system. Technical report, NASA/TM-2020-220484, March 2020.

[26] Tactical Resupply Vehicle (TRV). SURVICE Engineering, www.survice.com/who-we-are/focus-areas/tactical-resupply-vehicle-trv.

[27] A. Costenoble, Yong S. Jung, B. Govindarajan, and J. Baeder. Automated mesh generation and solution analysis of arbitrary airfoil geometries. In *Aeromechanics Design for Transformative Vertical Flight*, San Francisco, January 2018. AHS International.

[28] G. K. Yamauchi and W. Johnson. Trends of reynolds number effects on two-dimensional airfoil characteristics for helicopter rotor analyses. Technical report, 1983.

[29] C. Stutz, D. G. Bohl, and J. T. Hrynuk. Investigation of lift forces during long gust interactions at low reynolds number. In *AIAA SCITECH 2022 Forum*, page 42, 2022.

[30] J. Winslow, H. Otsuka, B. Govindarajan, and I. Chopra. Basic understanding of airfoil characteristics at low reynolds numbers (10 4–10 5). *Journal of Aircraft*, 55(3):1050–1061, 2018.

[31] M. B. Tischler and R. K. Remple. *Aircraft and rotorcraft system identification*. American Institute of Aeronautics and Astronautics Reston, VA, 2012.

[32] A. Bauknecht, X. Wang, J. Faust, and I. Chopra. Wind tunnel test of a rotorcraft with lift compounding. *Journal of the American Helicopter Society*, 66(1):1–16, 2021.